

PROBING THE REVERSIBLE AND IRREVERSIBLE VOLUME EXPANSION
OBSERVED IN LI-ION POUCH CELLS

by

Alexander J. Louli

Submitted in partial fulfilment of the requirements
for the degree of Master of Science

at

Dalhousie University
Halifax, Nova Scotia
October 2017

© Copyright by Alexander J. Louli, 2017

Table of Contents

List of Tables	vi
List of Figures	vii
Abstract	xiii
List of Abbreviations and Symbols Used	xiv
Acknowledgments.....	xvi
Chapter 1: Introduction	1
1.1 Motivation	1
1.2 Scope of this Work	2
Chapter 2: Lithium Ion Batteries	4
2.1 Lithium Ion Cells	4
2.2 Electrode Materials	8
2.2.1 Positive Electrode Materials	8
2.2.2 Negative Electrode Materials	11
2.3 Electrolyte	18
2.4 Li-ion Cell Degradation	19
2.4.1 The Solid Electrolyte Interphase (SEI).....	20
2.4.2 Loss of Active Material	22

2.4.3 Degradation Effects on the Voltage vs. Capacity of Cells	23
Chapter 3: Experimental Methods	30
3.1 Cell Preparation.....	30
3.1.1 Pouch Cells.....	30
3.1.2 Coin Cells	32
3.2 Electrochemical Testing.....	33
3.2.1 Pouch Cell Cycling.....	33
3.2.2 Coin Cell Cycling	33
3.2.3 dV/dQ Analysis	34
3.3 In-situ Electrode Expansion Measurements	38
3.3.1 Volume Measurements	39
3.3.2 Pressure Measurements	41
3.3.3 Thickness Measurements.....	42
Chapter 4: The Effect of Electrode Volume Expansion on Full Li-ion Pouch Cells.....	44
4.1 In-situ Volume, Pressure and Thickness Measurements.....	45
4.2 Volume Expansion of Cells with Graphite Negative Electrodes	47
4.2.1 Negative Electrode Expansion.....	48
4.2.2 Positive Electrode Expansion	49

4.2.3 Predicted Full Cell Expansion	50
4.3 Volume Expansion of Cells with Silicon-Composite Negative Electrodes	52
4.3.1 Type C Positive Electrode Expansion	53
4.3.2 Type C Negative Electrode Expansion.....	54
4.3.3 Predicted Type C Full Cell Expansion	61
4.3.4 Understanding the Expansion of Other Silicon-Containing Cells.....	63
Chapter 5: Pressure Evolution & Degradation Analysis.....	66
5.1 Analysis of Cells with Graphite Negative Electrodes	67
5.1.1 Electrode Comparison: AG vs. NG	68
5.1.2 Electrolyte Comparison: 0.25PES211 vs. 1.0PES211	75
5.1.3 Differential Voltage Analysis.....	81
5.2 Analysis of Cells with Silicon Negative Electrodes.....	86
5.2.1 Electrode Comparison	86
5.2.2 Differential Voltage Analysis.....	93
Chapter 6: Conclusions & Future Work	98
6.1 Conclusions	98
6.2 Future Work	101
Appendix.....	106

A.1 Additional Data & Information	106
A.1.1 Solvent and Additive Chemical Structures	106
A.1.2 Pressure Apparatus Compliancy	107
A.1.3 dV/dQ Analysis Fits	109
A.2 Permissions	114
References	116

List of Tables

Table 2.1: Positive electrode materials used in this work.....	9
Table 2.2: Negative electrode materials used in this work.	15
Table 2.3: Solvents and additives used in the electrolyte in this work.	19
Table 3.1: List of pouch cells used in this work.	31
Table A.1: Solvents and additives used in the electrolyte in this work.	106

List of Figures

Figure 2.1: Schematic of a Li-ion cell during charge (red arrows) and discharge (blue arrows).	5
Figure 2.2: Electrochemical characteristics of the positive electrode materials used in this work. The voltage vs. capacity, differential voltage vs. capacity (bottom panels), and differential capacity vs. voltage profiles during charge and discharge for a) LCO, b) NMC, and c) NCA. Lines are drawn at 4.28 V to the corresponding specific capacity for each electrode material.	10
Figure 2.3: a) Diagram of graphite and lithiated graphite (LiC_6), reproduced with permission from Jeff Dahn. b) Diagram of silicon, lithiated silicon ($\text{Li}_{15}\text{Si}_4$), and de-lithiated amorphous silicon, reproduced with permission from Mark Obrovac.	12
Figure 2.4: Electrochemical characteristics of the graphite materials used in this work. Voltage vs. capacity, differential voltage vs. capacity (bottom panels) and differential capacity vs. voltage profiles during charge and discharge for a) natural graphite and b) artificial graphite.	16
Figure 2.5: Voltage vs. capacity, differential voltage vs. capacity (bottom panels) and differential capacity vs. voltage profiles during charge and discharge for a) Si alloy, b) Si alloy-graphite, c) SiO, d) SiO-graphite, and e) n-Si-C.	17
Figure 2.6: Illustration of Li-ion cell degradation mechanisms that affect lithium inventory. a) Schematic of an electrode composed of active particles (blue) on a current collector, with electrical connections shown with light blue lines, and an SEI layer (brown) that coats the surface of the particles. b) Electrode after lithiation—the particles have expanded, disrupting the SEI causing growth/repair. One particle has cracked due to the stress of volume expansion. c) Electrode after de-lithiation—a particle and fracture has become electrically disconnected, and the newly formed SEI has accumulated on the particles. .	22
Figure 2.7: Schematic of the lithium inventory of a Li-cell.	24
Figure 2.8: a) Lithium inventory schematic during charge. b) The resulting full cell voltage vs. state of charge (SOC) curve during charge (black). The difference between the positive (red) and negative (blue) electrode voltage curves yields the full cell curve.	25
Figure 2.9: a) Lithium inventory schematic during discharge following Figure 2.8a. b) Corresponding voltage vs. capacity curves.	27
Figure 2.10: a) Lithium inventory schematic during discharge following Figure 2.8a, considering the effects of both slippage and mass loss. b) Corresponding voltage vs. capacity curves.	28
Figure 3.1: Image of a Li-ion pouch cell.	30

Figure 3.2: a) Components of a coin-type half cell. b) Electrodes removed from a pouch cell used to obtain the working electrode for the half cells.	32
Figure 3.3: An example of the differential voltage vs. specific capacity curve for a) a positive electrode and b) a negative electrode. c) A measured differential voltage vs. capacity curve of a full cell.	35
Figure 3.4: An example of the dV/dQ fitting process. In each panel, the fitting parameters (P_M , P_S , N_M , N_S) are changed to obtain a better fit. The fit quality improves from panel a) to panel e).....	36
Figure 3.5: In-situ volume measurement apparatus; a) pictured in left panel, b) shown schematically the right panel.	40
Figure 3.6: In-situ pressure and thickness measurement apparatus. a) Pressure measurement apparatus; b) schematic of pressure measurement apparatus; c) thickness measurement setup.....	42
Figure 4.1: In-situ volume and pressure measurements for Type A-i (NMC/AG) (a-b), Type A-ii (NMC/NG) (c-d) and Type B (LCO/Si-graphite) (e-f) cells.	46
Figure 4.2: In-situ volume, pressure and thickness measurements for Type C (NCA/SiO-graphite) (a-c), Type D-i (NCA/Si-C) (d-e) and Type D-ii (NCA/Si-C) (f-g) cells. The thickness data shown in panel c) was measured by Christopher Fell (Tesla Motors).	46
Figure 4.3: Fractional volume expansion of graphite during charge, adapted from data in Ref. ⁶ by Dahn. The highlighted region corresponds to the cycling range of graphite within the full cell: 0 to 71% SOC.....	49
Figure 4.4: Fractional volume expansion of NMC during charge measured by Weber et al. ⁴⁵ The highlighted region corresponds to the cycling range of graphite within the full cell: 0 to 71% SOC.	50
Figure 4.5: Predicted change in volume of a full NMC/graphite cell shown in magenta during charge (bottom left) and discharge (bottom right), with the corresponding voltage vs. capacity curve shown in the top panel in green. The change in volume of the graphite negative electrode is shown in blue, the NMC positive electrode in red, and their sum—the predicted net volume change of a full cell—in magenta.	51
Figure 4.6: Fractional volume expansion of NCA during charge (orange) and discharge (blue). The highlighted region corresponds to the cycling range of NCA within the full cell: 20 to 97% SOC. This data was collected by Jing Li (Dalhousie University).	54
Figure 4.7: a) Fractional volume expansion of graphite during charge adapted from Ref. ⁶ . b) Fractional volume expansion of amorphous silicon during charge and discharged adapted from Ref. ¹³ . The highlighted regions correspond to the cycling range of the negative electrode within the full cell: 3 to 84% SOC.....	55

Figure 4.8: The dV/dQ fits during charge a) and discharge b) of the SiO-graphite composite negative electrode. The graphite component (red) is added to the SiO component (blue) to make the calculated composite in solid magenta, which is a fit of the experimental data shown in dotted purple..... 58

Figure 4.9: dQ/dV vs. V (a,b), component state of charge (c,d) and fractional volume expansion (e,f) vs. composite electrode capacity of graphite (red) and SiO (blue) during the full cell charge (left column) and discharge (right column). 60

Figure 4.10: a) The calculated change of volume for each electrode component during charge and discharge. b) The measured volume, pressure and thickness data for Type C cells to compare to the calculated volume expansion profile. A plateau during charge, an asymmetric plateau near the top of charge, and a rapid fall seen in both a) and b) are highlighted as features i), ii) and iii) respectively..... 62

Figure 4.11: Fractional volume expansion of LCO adapted from Reimers and Dahn.⁴⁴.. 65

Figure 5.1: a) The pressure vs. time profiles of 1.0PES211 AG (blue) and NG cells (red). The corresponding voltage vs. time graph of the NG cell is shown in the top panel. The cells were cycled between 3.0 V and 4.2 V at 40°C. b) Proposed metrics for measuring pressure evolution: the pressure at the top of charge (TOC), the pressure at the bottom of charge (BOC), the pressure swing, and the average pressure. 70

Figure 5.2: The normalized capacity of 1.0PES211 AG (blue triangles) and NG (red circles) cells plotted vs. cycle no. (a) and time (b). All cells were cycled between 3.0 V and 4.2 V at 40°C. 71

Figure 5.3: Metrics of pressure evolution for 1.0PES211 AG (blue triangles) and NG cells (red circles). Each row shows the metric (left) and the change in the metric (right): a,b) the pressure at the bottom of charge; c,d) the pressure at the top of charge; e,f) the pressure swing; g,h) the average pressure. The capacity vs. time data for these cells is given in Figure 5.2. 72

Figure 5.4: The normalized capacity of 0.25PES211 AG (blue triangles) and NG cells (red circles) plotted vs. cycle no. (a) and time (b). All cells were cycled at C/6, unless labeled otherwise, between 3.0 V and 4.2 V at 40°C..... 73

Figure 5.5: Metrics of pressure evolution for 0.25PES211 AG (blue triangles) and NG cells (red circles). Each row shows the metric (left) and the change in the metric (right): a,b) the pressure at the bottom of charge; c,d) the pressure at the top of charge; e,f) the pressure swing; g,h) the average pressure. The capacity vs. time data for these cells is given in Figure 5.4. 74

Figure 5.6: The normalized capacity of AG 0.25PES211 (blue triangles) and 1.0PES211 cells (red circles) plotted vs. cycle no. (a) and time (b). All cells were between 3.0 V and 4.2 V at 40°C. The C-rate of cell x=1.00 AG v3 was changed mid-experiment resulting in a capacity drop around cycle 70..... 75

Figure 5.7: Metrics of pressure evolution for AG 1.0PES211 (blue triangles) and 0.25PES211 cells (red circles). Each row shows the metric (left) and the change in the metric (right): a,b) the pressure at the bottom of charge; c,d) the pressure at the top of charge; e,f) the pressure swing; g,h) the average pressure. The capacity vs. time data for these cells is given in Figure 5.6. 76

Figure 5.8: The normalized capacity of NG 1.0PES211 (blue triangles) and 0.25PES211 cells (red circles) plotted vs. cycle no. (a) and time (b). All cells were cycled between 3.0 V and 4.2 V at 40°C. 77

Figure 5.9: Metrics of pressure evolution for NG 1.0PES211 (blue triangles) and 0.25PES211 cells (red circles). Each row shows the metric (left) and the change in the metric (right): a,b) the pressure at the bottom of charge; c,d) the pressure at the top of charge; e,f) the pressure swing; g,h) the average pressure. The capacity vs. time data for these cells is given in Figure 5.8. 78

Figure 5.10: Summary of capacity loss vs. pressure growth data for AG and NG cells. a) Percent capacity loss vs. change in average pressure at the end of testing. b) Rate of capacity loss vs. rate of change in average pressure measured during the last 100 hours of testing. AG data are shown in shades of blue, NG data are shown in shades of red; 1.0PES211 electrolyte data are shown with circles, 0.25PES211 electrolyte data are shown with triangles. Cells were cycled at C/6 unless labeled otherwise, and were cycled between 3.0 V and 4.2 V at 40°C. 80

Figure 5.11: dV/dQ analysis of 0.25PES211 NG v3. The dV/dQ and corresponding dQ/dV fits are shown at the beginning of cycling (a,b) and at the end of cycling (c,d). Panels e-g show the fit parameters for the beginning (light blue) and end of cycling (dark blue). This cell was cycled at C/6 between 3.0 V and 4.2 V at 40°C. 82

Figure 5.12: dV/dQ analysis of 0.25PES211 NG v5 C/3. The dV/dQ and corresponding dQ/dV fits are shown at the beginning of cycling (a,b) and at the end of cycling (c,d). Panels e-g show the fit parameters for the beginning (light green) and end of cycling (dark green). This cell was cycled at C/3 between 3.0 V and 4.2 V at 40°C. 84

Figure 5.13: Summary of dV/dQ fit parameters for NG 0.25PES211 (shown in green) and 1.0PES211 cells (shown in blue). C/3 cycling rates are shown in lighter colours than cells than ran at C/6. 85

Figure 5.14: The normalized capacity of Type B (yellow crosses), Type C (green triangles), Type D-i (blue diamonds) and Type D-ii cells (red squares) plotted vs. cycle no. (a) and time (b). Cells were cycled at C/6 unless labeled otherwise, and cycled between 3.0 V and 4.2 V at 40°C. 87

Figure 5.15: Long-term cycling data comparing the performance of Type C and Type D-ii cells. All cells were cycled at C/3 except for Type C v2 which was cycled at C/6. Cells were cycled between 3.0 V and 4.2 V at 40°C. The long-term cycling data was collected by Xiaowei Ma and William Stone (Dalhousie University). 89

Figure 5.16: The pressure vs. time measurements for a) Type D-i, b) Type D-ii, c) Type C and d) Type B cells. Colour shades distinguish different trials for each cell type. Cells were cycled at C/6 unless labeled otherwise, and cycled between 3.0 V and 4.2 V at 40°C. 90

Figure 5.17: Metrics of pressure evolution for Type B (yellow crosses), Type C (green triangles), Type D-i (blue diamonds) and Type D-ii cells (red squares). Each row shows the metric (left) and the change in the metric (right): a,b) the pressure at the bottom of charge; c,d) the pressure at the top of charge; e,f) the pressure swing; g,h) the average pressure. The capacity vs. time data for these cells is given in Figure 5.14. 91

Figure 5.18: Summary of capacity loss vs. pressure growth data for silicon containing cells. a) Percent capacity loss vs. change in average pressure at the end of testing. b) Rate of capacity loss vs. rate of change in average pressure at the end of testing. 92

Figure 5.19: dV/dQ analysis of cell Type D-i v2. The dV/dQ and corresponding dQ/dV fits are shown at the beginning of cycling (a,b) and at the end of cycling (c,d). Panels e-g show the fit parameters for the beginning (light green) and end of cycling (dark green). This cell was cycled at C/6 between 3.0 V and 4.2 V at 40°C. 94

Figure 5.20: dV/dQ analysis of cell Type D-i v3 C/3. The dV/dQ and corresponding dQ/dV fits are shown at the beginning of cycling (a,b) and at the end of cycling (c,d). Panels e-g show the fit parameters for the beginning (light green) and end of cycling (dark green). This cell was cycled at C/3 between 3.0 V and 4.2 V at 40°C. 95

Figure 5.21: Summary of dV/dQ fit parameters for Type D-i (shown in green) and D-ii cells (shown in blue). C/3 cycling rates are shown in lighter colours than cells than ran at C/6. 96

Figure A.1: a) Apparatus used to measure compliancy. b) Compliancy data for different pouch cell systems. 108

Figure A.2: Differential voltage analysis for cell x=0.25 NG v2. This cell was cycled at C/6 between 3.0 V and 4.2 V at 40°C. 110

Figure A.3: Differential voltage analysis for cell x=0.25 NG v4. This cell was cycled at C/6 between 3.0 V and 4.2 V at 40°C. 110

Figure A.4: Differential voltage analysis for cell x=1.00 NG v3. This cell was cycled at C/6 between 3.0 V and 4.2 V at 40°C. 111

Figure A.5: Differential voltage analysis for cell x=1.00 NG v4 C/3. This cell was cycled at C/3 between 3.0 V and 4.2 V at 40°C. 111

Figure A.6: Differential voltage analysis for cell Type D-i v1. This cell was cycled at C/6 between 3.0 V and 4.2 V at 40°C. 112

Figure A.7: Differential voltage analysis for cell Type D-ii v2. This cell was cycled at C/6 between 3.0 V and 4.2 V at 40°C. 113

Figure A.8: Differential voltage analysis for cell Type D-ii v3 C/3. This cell was cycled at C/3 between 3.0 V and 4.2 V at 40°C..... 113

Abstract

The electrodes used in Li-ion cells experience a change in volume during lithiation and delithiation. This electrode volume expansion will affect a Li-ion cell, causing an overall volume change in compliant cell formats such as pouch cells, or an increase in pressure in non-compliant cell formats such as hard can cylindrical cells. In this work, the effects of electrode volume expansion on Li-ion pouch cells are measured. *In-situ* volume and thickness measurements were performed on pouch cells to probe the reversible volume expansion and contraction of cells during charge and discharge. *In-situ* pressure measurements were performed on volumetrically constrained pouch cells to probe the reversible pressure change caused by electrode expansion and contraction. In addition to the reversible volume expansion and contraction observed with these techniques, an irreversible volume expansion was observed with *in-situ* pressure measurements. It was found that cells that experienced larger irreversible pressure growth consistently exhibited worse capacity retention. Therefore, it is proposed that monitoring irreversible volume expansion with *in-situ* pressure measurements may be a useful technique to rank the performance of Li-ion cell chemistries.

List of Abbreviations and Symbols and Used

V_{OC}	Open circuit voltage
V_{pos}	Positive electrode voltage vs. Li/Li ⁺
V_{neg}	Negative electrode voltage vs. Li/Li ⁺
V_{avg}	Average voltage
μ_{neg}	Negative electrode chemical potential
μ_{pos}	Positive electrode chemical potential
LCO	LiCoO ₂
NMC	Li(Ni _{1-x-y} Mn _x Co _y)O ₂
NCA	Li(Ni _{1-x-y} Co _x Al _y)O ₂
AG	Artificial graphite
NG	Natural graphite
EC	Ethylene carbonate
EMC	Ethylmethyl carbonate
DMC	Dimethyl carbonate
DEC	Diethyl carbonate
FEC	Fluoroethylene carbonate
VC	Vinylene carbonate
PES	Prop-1-ene-1,3-sultone
DTD	1,3,2-Dioxathiolane-2,2-dioxide
TTSPi	Tris(trimethylsilyl)phosphite

TOC	Top of charge
BOC	Bottom of charge
SOC	State of charge
XRD	X-ray diffraction
a-	Amorphous
n-	Nano
SEI	Solid electrolyte interphase
P	Probability of turbostratic misalignment
e	Elementary charge
e^-	Electron

Acknowledgments

I am very grateful to all those who have lent their support and guidance to me over these last two years. First and foremost, I would like to thank my supervisor Jeff Dahn for all he has taught me, and all of the patience it took to do so, because sometimes I am a slow learner. His excitement and passion for research is contagious and continues to inspire me as a scientist, as well as to promote sleepless nights (in a good way). I would like to thank Simon Trussler for designing and ultimately constructing several key pieces of equipment that were essential for my work, including bringing “superboats” into reality. I am thankful to all the administrative support I received from the physics department staff who always tried to go out of their way to make my life easier. And of course, many thanks to all of the wonderful mentors, colleagues, and dear friends I have made in the Dahn lab.

Chapter 1: Introduction

1.1 Motivation

Lithium ion (Li-ion) batteries are the primary power source for portable electronics—power tools, laptops, cell phones; devices that have now become indispensable in everyday life. The electrification of cars is underway using Li-ion batteries to replace fossil fuel-consuming vehicles. These all-electric vehicles can achieve driving ranges of >350 km before recharging.¹ Grid energy storage is necessary to move away from non-renewable energy sources due to the inherent intermittency of renewable sources such as wind and solar. The storage of renewable energy with batteries can address these intermittency issues. Li-ion batteries have and will continue to play an important role in grid energy storage.

Li-ion has become the chemistry of choice in the rechargeable battery market due to its many excellent electrochemical properties, such as low self-discharge, good rate capability, high energy density, and good cycle life.² Although remarkable advances in Li-ion batteries have been made since their introduction in 1990,¹ the improvement of energy density and lifetime remains of paramount importance to industry, and therefore, to Li-ion battery researchers. Improving the energy density of Li-ion batteries is important for applications where battery size is a concern, such as portable electronics and electric vehicles. Additionally, increasing the energy density of batteries will decrease their cost by virtue of providing more energy with less battery material. Efforts to increase energy density focus on enhancing the energy density of the constituent electrode materials used

in Li-ion batteries. Improving the cycle life of Li-ion batteries is important for applications which require many hundreds to thousands of charge/discharge cycles over tens of years, such as electric vehicles and grid energy storage. This also necessitates the ability to predict the long-term lifetime (over many years) of batteries using relatively short-term tests (over several weeks). Verifying that a new Li-ion chemistry will last a decade by testing that battery for a decade is impractical. Therefore, methods to rank the lifetime of Li-ion batteries are important.

1.2 Scope of this Work

This thesis focuses on addressing the two challenges detailed above: increasing the energy density of Li-ion batteries, and developing short-term testing methods to rank Li-ion battery lifetime. The former is done by studying Li-ion batteries which employ high energy density negative electrode materials, namely silicon-containing electrodes. The main obstacles for the adoption of silicon electrode materials are problems associated with the large volume expansion these materials experience during lithiation. Therefore, the volume expansion of electrode materials is studied in this work. *In-situ* techniques are used to measure the result of electrode expansion within Li-ion cells. These measurements are used to understand the volume expansion of a variety of Li-ion cell chemistries, with an emphasis on chemistries with different negative electrodes. One of the *in-situ* techniques devised for this work, *in-situ* pressure measurements of volumetrically constrained pouch cells, is then applied to rank the long-term efficacy of different Li-ion cell chemistries.

Chapter 2 presents an introduction to Li-ion cells. The main components of Li-ion cells—the active materials (the positive and negative electrodes) and the electrolyte are described. Chapter 2 concludes with a discussion of the causes of Li-ion cell degradation. Chapter 3 describes the experimental methodology used in this thesis. Namely, the preparation of Li-ion cells, the electrochemical testing, and the *in-situ* measurement techniques used in this work. The main results of this thesis are presented in Chapters 4 and 5. Chapter 4 is a consideration of electrode volume expansion within Li-ion cells. The volume and thickness expansion, as well as the pressure evolution of constrained pouch cells caused by electrode volume expansion is measured for a variety of cell chemistries. Calculations are presented to elucidate the expansion behaviour observed. Chapter 5 employs the *in-situ* pressure measurement technique developed in this work as a tool for ranking the long-term performance of Li-ion cell chemistries by monitoring the pressure evolution of volumetrically constrained pouch cells. Chapter 6 presents the conclusions of this thesis.

The results presented in Chapter 4 of this thesis were previously published in a peer-reviewed journal article: A. J. Louli, Jing Li, S. Trussler, Christopher R. Fell, and J. R. Dahn, Volume, Pressure and Thickness Evolution of Li-Ion Pouch Cells with Silicon-Composite Negative Electrodes, *J. Electrochem. Soc.*, **164** (12) A2689-A2696 (2017). doi: 10.1149/2.1691712jes. The license agreement to reproduce this previously published work is shown in Appendix A.2.

Chapter 2: Lithium Ion Batteries

Lithium ion (Li-ion) batteries are a class of secondary (rechargeable) batteries which convert stored chemical energy into electrical energy during discharge and vice versa during charge. This is accomplished by reduction and oxidation (redox) reactions that occur in the active materials of Li-ion batteries. Li-ion batteries are comprised of several Li-ion cells—the electrochemical units in which the redox reactions occur. These cells are connected in series and in parallel to deliver the desired voltage and capacity characteristics for the battery. This thesis will discuss the characteristics and performance of Li-ion cells.

2.1 Lithium Ion Cells

Li-ion cells are composed of three main components: the positive electrode, the negative electrode, and the electrolyte, schematically shown in Figure 2.1. The electrodes are the active materials where chemical energy is stored. These materials are usually intercalation compounds—materials with layered structures allowing for the reversible insertion and de-insertion of lithium between layers. Graphite is the most prevalent negative electrode material, which is coated on a copper current collector. Positive electrode materials are mainly lithium transition metal oxides, which are coated on an aluminum current collector. This is depicted in Figure 2.1. The electrode materials of Li-ion cells will be discussed further in Section 2.2. The electrolyte is the medium of transport of lithium ions between electrodes facilitating the storage and delivery of electrical energy. Li-ion cell electrolyte consists of a lithium salt (most commonly LiPF_6) typically dissolved in a mixture of organic carbonate solvents. The electrolyte of Li-ion cells will be discussed further in

Section 2.3. A microporous film known as a separator physically divides the positive and negative electrodes to prevent internal shorts, forcing electrical energy to flow through an external circuit to do useable work. As such, separator materials must be electronic insulators while also allowing the flow of lithium ions between electrodes. Separators used in Li-ion cells are usually microporous polyethylene or polypropylene films.²

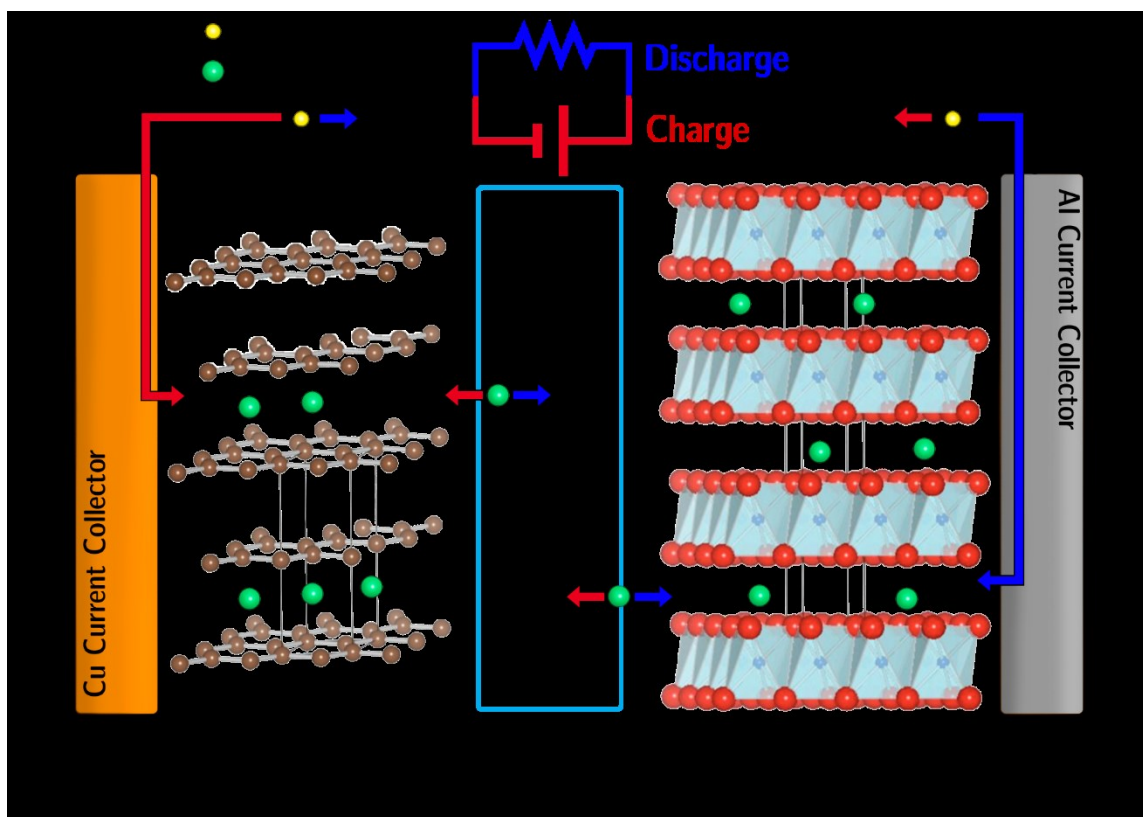
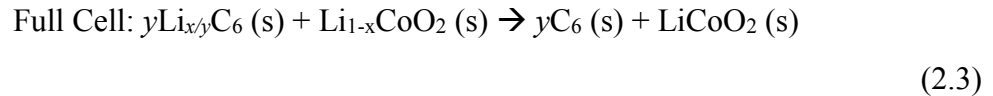
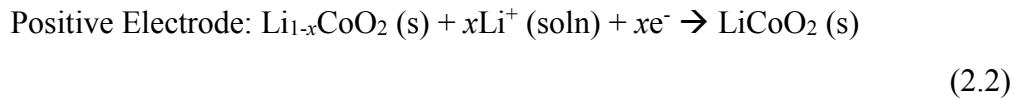
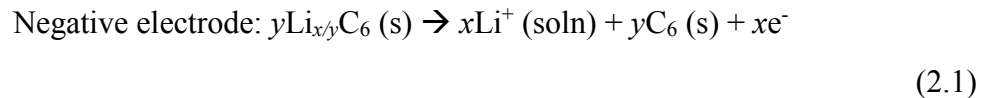


Figure 2.1: Schematic of a Li-ion cell during charge (red arrows) and discharge (blue arrows).

During cell operation, redox reactions occur at the positive and negative electrodes, resulting in an exchange of electrons and lithium ions. Figure 2.1 is a schematic of a Li-ion cell during charge (red arrows) and discharge (blue arrows). In the charged state, the negative electrode of a Li-ion cell is lithiated (filled with lithium), and the positive

electrode is partially de-lithiated. When an external load is connected across the cell, the negative electrode will spontaneously oxidize, releasing a lithium ion and an electron from the negative electrode. This reaction, using graphite as the negative electrode, is given by Equation 2.1. The Li-ion then travels to the positive electrode facilitated by the electrolyte while the electron travels through the external circuit performing work on the load. The electron and lithium ion reunite at the positive electrode which is reduced. This reaction, using LiCoO₂ as the transition metal oxide for the positive electrode, is given by Equation 2.2. The net, full cell reaction is given by Equation 2.3. This describes the discharge of a Li-ion cell.



The value of x depends on the upper cutoff voltage of the positive electrode. For an upper cutoff voltage of 4.28 V, x is about 0.6. The value of y is chosen so that the value of x/y is about 0.9 when the cell is fully charged to avoid lithium plating.

To charge a Li-ion cell, the external load shown in Figure 2.1 must be replaced with a charging source. This reverses the reactions given in Equations 2.1-2.3. During charge, lithium atoms travel from the positive electrode which is oxidized to the negative electrode which is reduced.

The open circuit voltage (V_{OC}) of a Li-ion cell, measured in V, is determined by the difference in chemical potential of the negative (μ_{neg}) and positive electrodes (μ_{pos}), given by:

$$V_{OC} = (\mu_{neg} - \mu_{pos})/e \quad (2.4)$$

where e is the elementary charge. Since voltage is a potential difference, there is no such thing as the voltage of a single electrode; therefore, when a voltage of a single Li-ion cell electrode is referred to, this is always given relative to Li/Li⁺ (i.e. relative to lithium in lithium metal). Using this convention, the voltage of a Li-ion cell can also be given as a difference between the positive and negative electrode voltage vs. Li/Li⁺ (V_{pos} and V_{neg} , respectively):

$$V_{pos} - V_{neg} = (\mu_{Li} - \mu_{pos})/e - (\mu_{Li} - \mu_{neg})/e \quad (2.5)$$

$$V_{pos} - V_{neg} = (-\mu_{pos} + \mu_{neg})/e \quad (2.6)$$

$$V_{pos} - V_{neg} = V_{OC} \quad (2.7)$$

The capacity of a Li-ion cell, measured in mAh, is determined by the number of electrons exchanged during charge and discharge. This depends on the capacity of the positive and negative electrodes. These capacities are often more useful to be given by weightusing specific capacity measured in mAh/g or by volume using volumetric capacity measured in Ah/L. The capacity of Li-ion cells decreases over time and cycle number due to degradation mechanisms which will be discussed in Section 2.4. The energy a Li-ion cell

can deliver, measured in Wh, is the product of the average voltage of the cell (V_{avg}) and the capacity of the cell. Again, it is often more useful to measure the energy per unit weight or volume in Wh/kg or Wh/L. Volumetric energy density, and therefore volumetric capacity, tends to be the most important consideration for Li-ion battery applications such as portable electronics and electric vehicles where size is a principal concern.³ The cost and cycle life are also very important considerations for Li-ion cells. An important metric that industry uses to assess the viability of a Li-ion cell is the cost of the cell to deliver energy over its entire cycle life, i.e. $\$/(\text{Wh} * \text{cycle life})$ —minimizing this cost, by increasing the Wh and cycle life of Li-ion cells is the goal of many researchers.

2.2 Electrode Materials

This section discusses the active materials used in Li-ion cell electrodes. Commercial electrodes,⁴ as well as electrodes used in cells studied in this work, are generally composed of >95% active material, ~2% binder and ~2% conducting additive. In this thesis, when electrodes and electrode materials are discussed, it is the active component that is being referred to.

2.2.1 Positive Electrode Materials

The positive electrode materials used in Li-ion cells are mainly layered lithium transition metal oxides⁵—three of which are used in this thesis, detailed in Table 2.1. Lithium cobalt oxide (LiCoO_2 , abbrv. LCO) was the first positive electrode material used in Li-ion cells and is still in common use today as a result of the good cycle life and energy it provides.¹ More recently, $\text{Li}(\text{Ni}_{1-x-y}\text{Mn}_x\text{Co}_y)\text{O}_2$ (NMC) and $\text{Li}(\text{Ni}_{1-x-y}\text{Co}_x\text{Al}_y)\text{O}_2$ (NCA) have emerged

as positive electrode materials for Li-ion cells due to their superior energy density (NCA), superior safety (NMC), and lower cost than LCO due to the reduced used of expensive cobalt.² The values of x and y in the NMC material used in this thesis were x = 0.3 and y = 0.2 (this grade of NMC is referred to as NMC532 due to the respective ratios of nickel, manganese and cobalt). The values of x and y in the NCA material used in this thesis were x = 0.15 and y = 0.05.

Table 2.1: Positive electrode materials used in this work.

Abbrev.	Name	Chemical Formula	Specific Capacity (mAh/g)	Average Voltage (V)
LCO	Lithium Cobalt Oxide	LiCoO ₂	155	3.9
NMC	Nickle Manganese Cobalt Oxide	Li(Ni _{1-x-y} Mn _x Co _y)O ₂	160 [†]	3.8
NCA	Nickle Cobalt Aluminum Oxide	Li(Ni _{1-x-y} Co _x Al _y)O ₂	180 [‡]	3.7

*Capacities given to an upper cutoff voltage of 4.28 V

†For x = 0.3, y = 0.2

‡For x = 0.15, y = 0.05

Electrochemistry

The electrochemical characteristics of the LCO, NMC and NCA materials used in this work are shown in Figures 2.2a, b and c respectively. These figures show the charge and discharge voltage vs. capacity, differential voltage vs. capacity (bottom panels), and differential capacity vs. voltage profiles (top panels) of each material. These data were collected by charge/discharge cycling each positive electrode material vs. lithium metal in half cells as detailed in the Experimental Methods chapter in Section 3.1.2. When a full

Li-ion cell is charged to 4.2 V, the corresponding voltage of the positive electrode relative to Li/Li^+ is about 4.28 V. Therefore, lines are drawn at 4.28 V and to the corresponding capacity for each electrode material in Figure 2.2 for a comparison of the useful relative specific capacities. It is clear that the specific capacity of $\text{NCA} > \text{NMC} > \text{LCO}$.

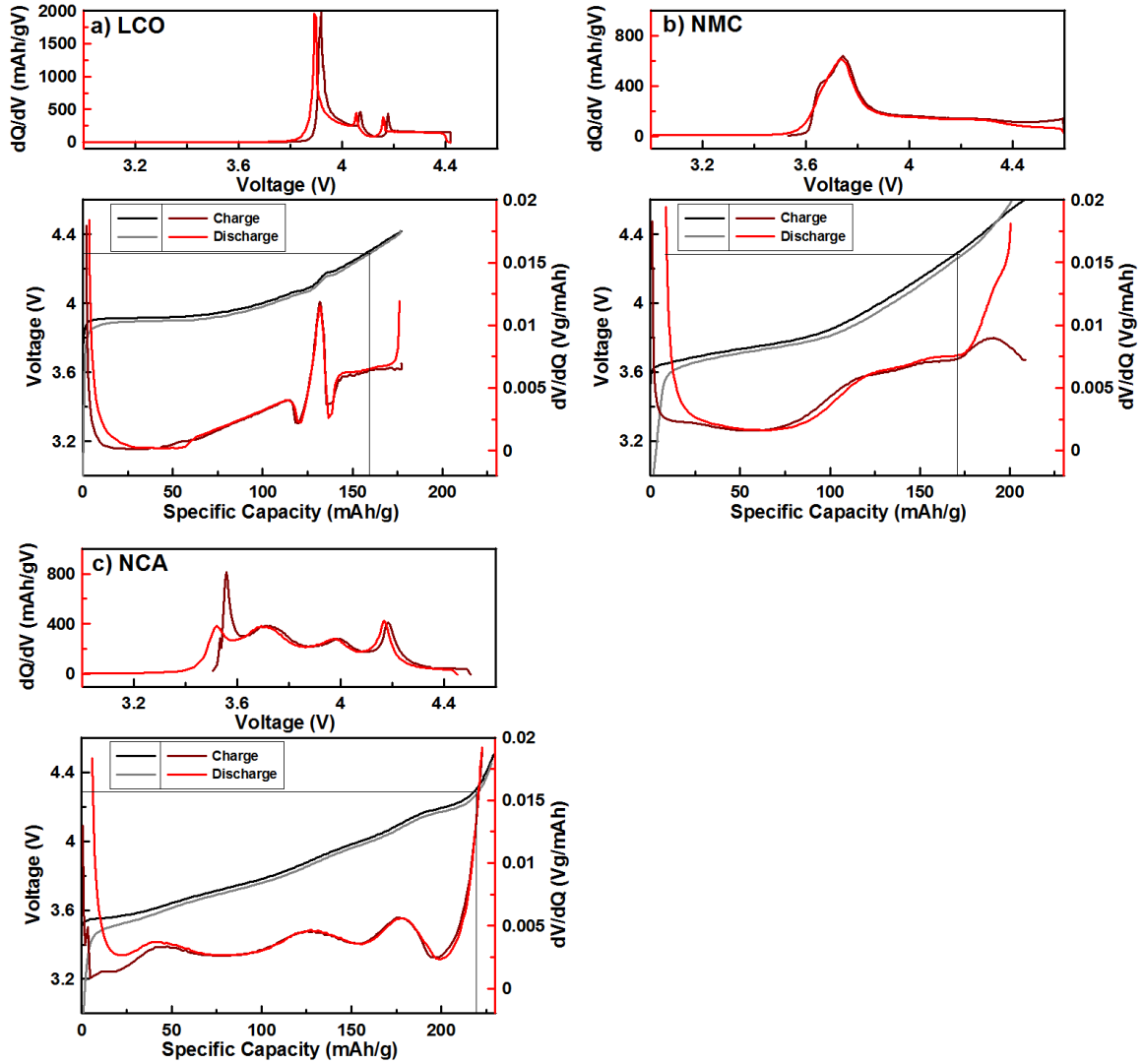


Figure 2.2: Electrochemical characteristics of the positive electrode materials used in this work. The voltage vs. capacity, differential voltage vs. capacity (bottom panels), and differential capacity vs. voltage profiles during charge and discharge for a) LCO, b) NMC, and c) NCA. Lines are drawn at 4.28 V to the corresponding specific capacity for each electrode material.

2.2.2 Negative Electrode Materials

The most common negative electrode material for Li-ion cells is graphite—an intercalation host that stores lithium between graphene sheets, as shown in Figure 2.3a. The insertion of lithium into graphite is a relatively benign process, only expanding the volume of graphite by 10% during charge.^{6,7} Lithium ion insertion into graphite undergoes a staging process in which the ions preferentially fill interstitial layers a repeated number of layers apart before filling adjacent layers. Ions are first inserted into every fourth interstitial layer (referred to as stage 4), and then every third (stage 3) and second layer (stage 2), until every interstitial layer is filled (stage 1). The voltage vs. capacity curve of graphite has plateaus corresponding to the staging of graphite, which can be seen in the black curves shown in Figure 2.4. The staging of graphite along with the correspondence to electrochemical data was shown by Zheng et al.⁸ The insertion of lithium ions within the interstitial layers of graphite increases the interlayer spacing of graphite causing volume expansion during charge and contraction during discharge.⁶

There are different types of graphite that are used in Li-ion cells. Two grades of graphite—natural (NG) and synthetic “artificial” graphite (AG) are used in this thesis. Natural graphite is just that—naturally occurring graphite that is mined from the ground. Artificial graphite is synthesized by pyrolyzing (extreme heating under inert atmosphere) a liquid phase carbon precursor such as petroleum pitch.^{2,9} Important parameters to consider for the performance of different types of graphite is degree of crystallinity and the surface area of the material. The former is characterized by P , the probability of turbostratic misalignment—this describes the fraction of graphene layers that are rotated or translated from positions that would form a perfect graphitic crystal structure. Zheng et al. showed

that these misalignments block layers in which lithium could otherwise occupy, thereby decreasing the capacity of graphite with a larger value of P .⁸ Natural graphite tends to have a higher degree of crystallinity, and thus a lower P resulting in a larger initial capacity than artificial graphite.⁹ Therefore, natural graphite is the obvious choice to obtain a larger energy density. During lithium de/insertion, electrolyte reacts at the surface of lithiated graphite, irreversibly consuming lithium thereby decreasing the capacity of Li-ion cells. Larger graphite surfaces will induce more reactions, therefore, to minimize these unwanted reactions, one would want to minimize the surface area of graphite. Previous studies have shown that graphite exfoliation occurs more readily in highly crystallized graphite,^{10,11} causing an enlarged surface area. Therefore, artificial graphite electrodes may exhibit less exfoliation and capacity-consuming reactions resulting in superior long-term capacity retention compared to highly crystallized natural graphite electrodes with larger initial capacities. These are important considerations for deciding which type of graphite to use in a Li-ion cell.

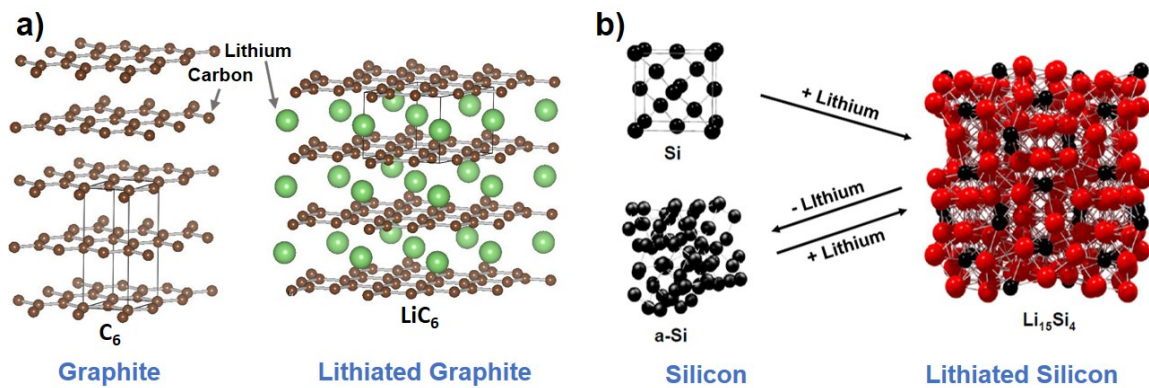


Figure 2.3: a) Diagram of graphite and lithiated graphite (LiC_6), reproduced with permission from Jeff Dahn. b) Diagram of silicon, lithiated silicon ($Li_{15}Si_4$), and de-lithiated amorphous silicon, reproduced with permission from Mark Obrovac.

Graphite was adopted as the negative electrode material for Li-ion cells early in their history and has remained the most prevalent negative electrode material due to the excellent electrochemical properties it provides.¹ In their review article *Alloy Negative Electrodes for Li-ion Batteries*,⁷ Obrovac et al. state:

Graphite is an excellent negative electrode (anode) material for Li-ion batteries. It has ... [a] low average voltage (but not too low, so that Li plating can be avoided), low voltage hysteresis, good rate capability, low irreversible capacity, good thermal stability when low surface area is maintained, low volume expansion during lithiation, good cycle life, high Coulombic efficiency (CE), good electronic conductivity, excellent densification properties in electrode coatings, and is based on an inexpensive and plentiful raw material.⁷

However, graphite has a relatively low theoretical capacity (372 mAh/g for graphite and 719 Ah/L for LiC_6) relative to other possible negative electrode materials. This has motivated the search for other suitable negative electrode materials for Li-ion cells. Silicon negative electrode materials have generated much interest due the massive theoretical capacities they could provide—3579 mAh/g for silicon and 2194 Ah/L for $\text{Li}_{15}\text{Si}_4$, the most lithiated silicon phase.¹² Unfortunately, silicon negative electrodes do not share many of the properties that make graphite electrodes so excellent as listed by Obrovac et al. On the contrary, silicon electrodes have a large voltage hysteresis, large volume expansion during lithiation and relatively poor cycle life compared to graphite.^{7,13}

Silicon electrodes do not work via lithium intercalation like graphite. Upon lithium insertion, lithium alloys with silicon, dramatically changing its structure as shown in Figure 2.3b, causing a volume expansion of 280%.¹³ Previous studies have shown how this volume expansion can be detrimental to electrodes by causing constituent particles to electrically disconnect from their current collectors, particles to fracture, and damage to

the SEI—all of which result in large capacity loss.^{7,13,14} During first lithiation, crystalline silicon goes through an amorphous Li_xSi (a- Li_xSi) phase before crystallizing to the highest room temperature-accessible lithiated silicon phase $\text{Li}_{15}\text{Si}_4$. This crystalline phase can be avoided during future lithiations by limiting the discharge potential to >70 mV vs. Li/Li^+ , causing Li_xSi to stay in an amorphous phase.^{7,12,15} This is ideal since the crystallization results in a two-phase region of a- Li_xSi and $\text{Li}_{15}\text{Si}_4$ which is known to cause high internal stresses resulting in particle cracking and electrical disconnection. Additionally, confining silicon to nano-sized domains can prevent the formation of two-phase regions, reducing the internal stress on particles to avoid fracture.^{16–18} Alloying active silicon material with an inactive material also serves this purpose, as well as to suppress the overall volume change of the material.¹⁶ Efforts to reduce electrical disconnection of particles often involve making composites of Si-containing electrode materials with more volumetrically benign materials such as carbon.^{18–21} This effort aims to take advantage of the high capacity of silicon, while diminishing the overall volume expansion of the composite electrode.

Si alloy, SiO and nano-Si-C are the silicon materials used in this thesis. The Si alloy is a material provided by 3M. It is an active-inactive alloy in which the active silicon microstructure remains amorphous during cycling.²² SiO consists of a nano-structure of a-Si and a- SiO_2 in a 1:1 mole ratio.²¹ During first charge/discharge, lithium first irreversibly reacts with SiO_2 to form Li_4SiO_4 and Si. The Li_4SiO_4 remains inactive throughout subsequent cycling while the amorphous n-Si is reversibly lithiated and de-lithiated.^{21,23,24} When used in Li-ion cells in this thesis, the Si alloy and SiO are composited with graphite. Nano-Si-C is composed of nano-grains of silicon coated with carbon. Each of these Si-

containing materials employ the strategy of limiting the active grain size to impede two-phase regions, as well as using an inactive phase (inactive portion of Si alloy, SiO₂) and/or a volumetrically benign active phase (carbon coating, graphite) to suppress volume expansion. Table 2.2 details all of the electrode materials used in this work.

Table 2.2: Negative electrode materials used in this work.

Abbrev.	Name	Chemical Formula	Specific Capacity (mAh/g)	Volumetric Capacity (Ah/L)	Average Voltage (V)
AG	Artificial graphite	C ₆	350	700	0.125
NG	Natural graphite	C ₆	365	719	0.125
SiO	Silicon Oxide	SiO	1600	1547	0.4
n-Si-C	nano Silicon coated with Carbon	Si-C	650	N/A	0.26
Si Alloy	Silicon Alloy	-	1000	1550	0.37
Si Alloy-AG	Si Alloy-graphite composite	-	420	785	0.20
SiO-AG	Silicon Oxide-graphite composite	-	410	750	0.18

Electrochemistry

The electrochemical characteristics of the graphite grades (NG, AG), the silicon materials (Si alloy, SiO), and the composite silicon electrode materials (Si alloy-graphite, SiO-graphite and n-Si-C) used in this work are shown in Figures 2.4 and 2.5. These figures show the charge and discharge voltage vs. capacity, differential voltage vs. capacity (bottom panels), and difference capacity vs. voltage profiles (top panels) of each material.

These data were collected by cycling each negative electrode material vs. lithium metal in half cells as detailed in the Experimental Methods chapter in Section 3.1.2.

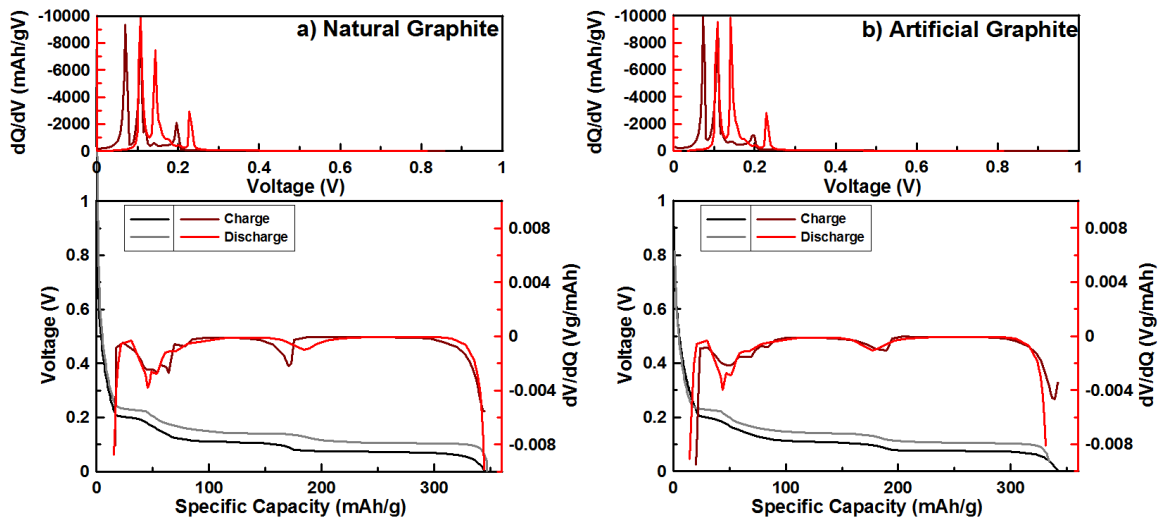


Figure 2.4: Electrochemical characteristics of the graphite materials used in this work. Voltage vs. capacity, differential voltage vs. capacity (bottom panels) and differential capacity vs. voltage profiles during charge and discharge for a) natural graphite and b) artificial graphite.

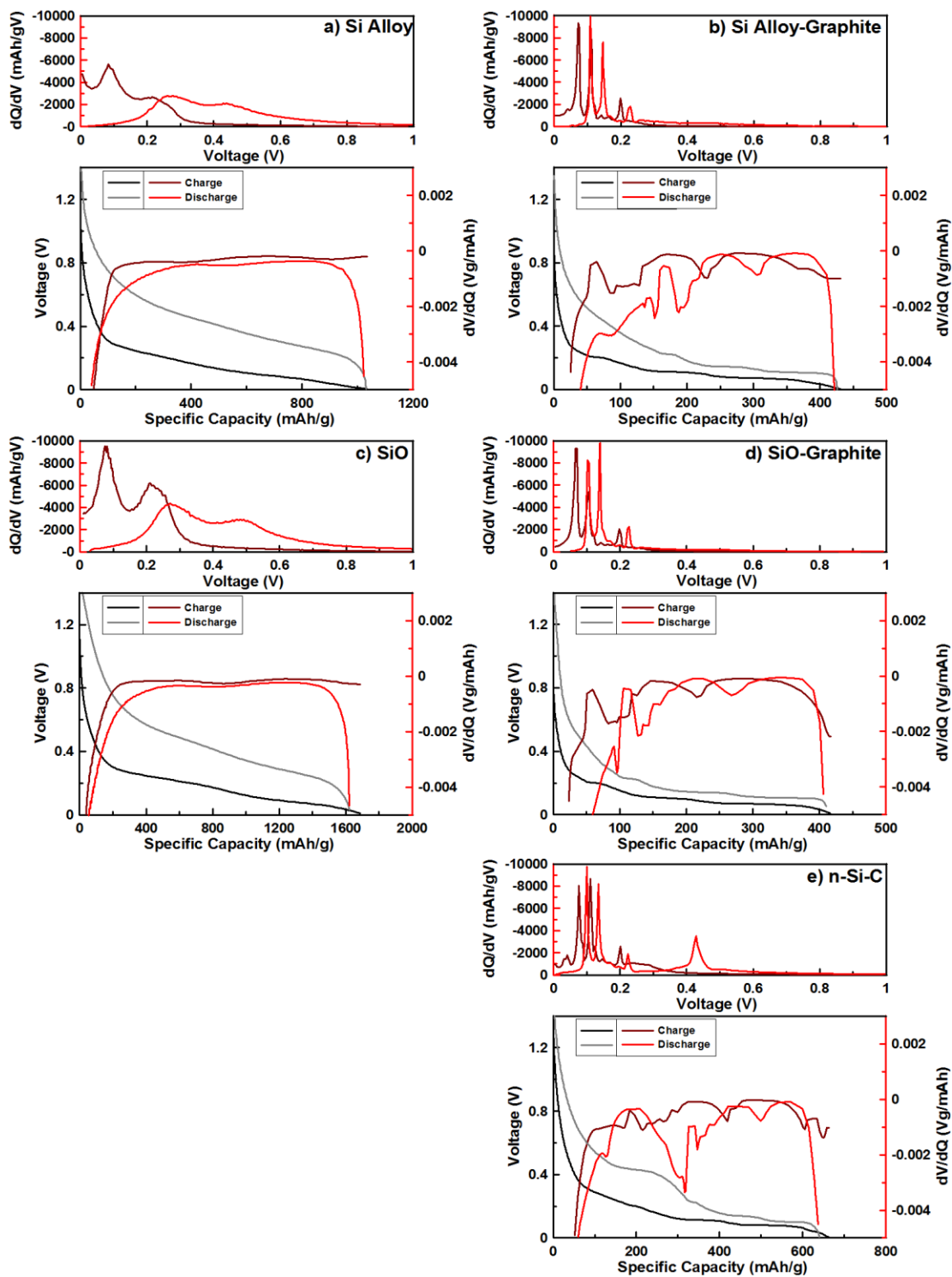


Figure 2.5: Voltage vs. capacity, differential voltage vs. capacity (bottom panels) and differential capacity vs. voltage profiles during charge and discharge for a) Si alloy, b) Si alloy-graphite, c) SiO, d) SiO-graphite, and e) n-Si-C.

2.3 Electrolyte

Electrolyte is an ionic conductor used to facilitate the transport of lithium ions between electrodes. The electrolyte used in Li-ion cells is composed of a lithium salt (most commonly lithium phosphorous hexafluoride, LiPF_6), typically dissolved in a mixture of organic carbonate solvents. Lithium phosphorous hexafluoride is used for the high ionic conductivity LiPF_6 solutions provide. Favorable solvent qualities are high dielectric constants (to allow lithium salt solvation to high molarities), low viscosity, a broad temperature range of operation (i.e. low freezing and high melting points), and good stability over the range of potentials Li-ion cell electrodes cycle at, about 0 to 4.5 V.² However, practical solvents are not stable over this entire range—particularly at the extremes (<1 V and >4.4 V), corresponding to voltages accessed by the negative and positive electrodes, respectively. As such, electrolyte reacts at the surface of the electrodes. The product of such reactions is a film that deposits on the electrode surfaces known as the solid electrolyte interphase (SEI).^{2,25} The SEI will be discussed further in Section 2.4. Electrolyte is often formulated with additives, chemicals typically added at < 10% by weight, to improve the performance Li-ion cells.^{2,26}

All electrolyte in this work was made with LiPF_6 salt. The solvents and additives used in this work are listed in Table 2.3. Ethylene carbonate (EC), ethylmethyl carbonate (EMC), dimethyl carbonate (DMC), diethyl carbonate (DEC) and fluoroethylene carbonate (FEC) were used as solvents. Vinylene carbonate (VC), prop-1-ene-1,3-sultone (PES), 1,3,2-Dioxathiolane-2,2-dioxide (DTD) and tris(trimethylsilyl)phosphite (TTSPi) were used as additives. The chemical structures of these solvents and additives are shown in the appendix in Table A.1. PES, DTD and TTSPi were used in combination to make the

ternary additive blend known as xPES211: x*2% PES, x*1% DTD, x*1% TTSPi (all by weight). In this work, 1.0PES211 and 0.25PES211 was used, i.e, (2%, 1%, 1%) and (0.5%, 0.25%, 0.25%) of (PES, DTD, TTSPi), respectively.

Table 2.3: Solvents and additives used in the electrolyte in this work.

Abbreviation	Name
EC	ethylene carbonate
EMC	ethylmethyl carbonate
DMC	dimethyl carbonate
DEC	diethyl carbonate
FEC	fluoroethylene carbonate
VC	vinylene carbonate
PES	prop-1-ene-1,3-sultone
DTD	1,3,2-Dioxathiolane-2,2-dioxide
TTSPi	tris(trimethylsilyl)phosphite

Electrolyte development and optimization was not the focus of this thesis work, therefore the motivation behind the use of the different electrolytes and blends will not be discussed here. The electrolyte formulations used in this work are blends known to work well with the electrode chemistries they are paired with.^{7,20,27-31}

2.4 Li-ion Cell Degradation

Li-ion cells do not last forever due to components which slowly degrade. The positive and negative electrodes can deteriorate and the electrolyte reacts with the charged electrodes. These degradation mechanisms consume and trap active lithium used to store and provide energy. As this lithium becomes unavailable, the capacity of a Li-ion cell decreases. Therefore, an accounting of the lithium inventory is necessary to understand the

degradation of Li-ion cells. This section discusses the degradation mechanisms which affect the lithium inventory and decrease the capacity of Li-ion cells.

2.4.1 The Solid Electrolyte Interphase (SEI)

The electrolytes used in Li-ion cells are not stable at *ca.* <1 V and >4.4 V. These potentials, achieved at the negative and positive electrodes respectively, cause the electrolyte to react at the electrode surfaces. Despite this, Li-ion cells are able to function because the reduction and oxidation products of these reactions form a passivating layer on the electrode surfaces known as the solid electrolyte interphase (SEI) that impedes further reactions.^{2,25} The SEI is ideally a good ionic conductor to allow the transport of lithium ions between electrode and the electrolyte and a good ionic insulator to prevent further electrode-electrolyte reactions by blocking the exchange of electrons. The SEI forms during the first charge of a Li-ion cell, when most of the electrode-electrolyte reactions occur. This first charge (and sometimes accompanying first discharge) is called a formation step, which is designed to optimize the properties of the SEI that is formed, namely forming a suitable passivation layer.²⁵

The electrode-electrolyte reactions that form the SEI are often called unwanted side reactions or parasitic reactions. These reactions irreversibly consume lithium from the lithium inventory of the cell (active lithium from electrodes, lithium ions from the electrolyte); preventing the consumed lithium from performing useful work by trapping it within the SEI. This consumption of the lithium inventory decreases the capacity of Li-ion cells.^{32,33} Previous studies have shown that SEI growth and the resulting consumption of Li inventory is often proportional to $time^{1/2}$, and is therefore slowed over time.³⁴

Regardless, the gradual growth of the SEI will continue to degrade Li-ion cells. Additionally, possible disruptions to the SEI layer can exacerbate electrode-electrolyte reactions until the SEI is sufficiently repaired. SEI growth and repair is a degradation mechanism of Li-ion cells.^{32,33} This is schematically illustrated in Figure 2.6. Figure 2.6a depicts a de-lithiated electrode represented by a collection of active material particles shown in blue deposited on a current collector, with electrical connections between particles and the current collector shown with light blue lines. An SEI layer is shown in brown coating the surface of each electrode particle. If the electrode material is one that exhibits a large volume expansion, such as silicon, the constituent electrode particles will dramatically expand upon lithiation. This is shown in Figure 2.6b. The SEI is unable to accommodate the particle expansion, and is thus stretched and torn, leaving portions of the lithiated particles exposed. The damage to the SEI is repaired by new film-forming electrode-electrolyte reactions, passivating the disruptions with newly formed SEI shown in light red. This process further consumes lithium from the inventory. Figure 2.6c shows the subsequent de-lithiated state of the electrode. Compared to the initial de-lithiated state, each particle is coated with a thicker layer of SEI due to the extra SEI formed to passivate the previous disruptions. One could imagine that many cycles of this repair and growth could cause the overall volume of the SEI to increase sufficiently to cause the entire electrode to expand in volume.

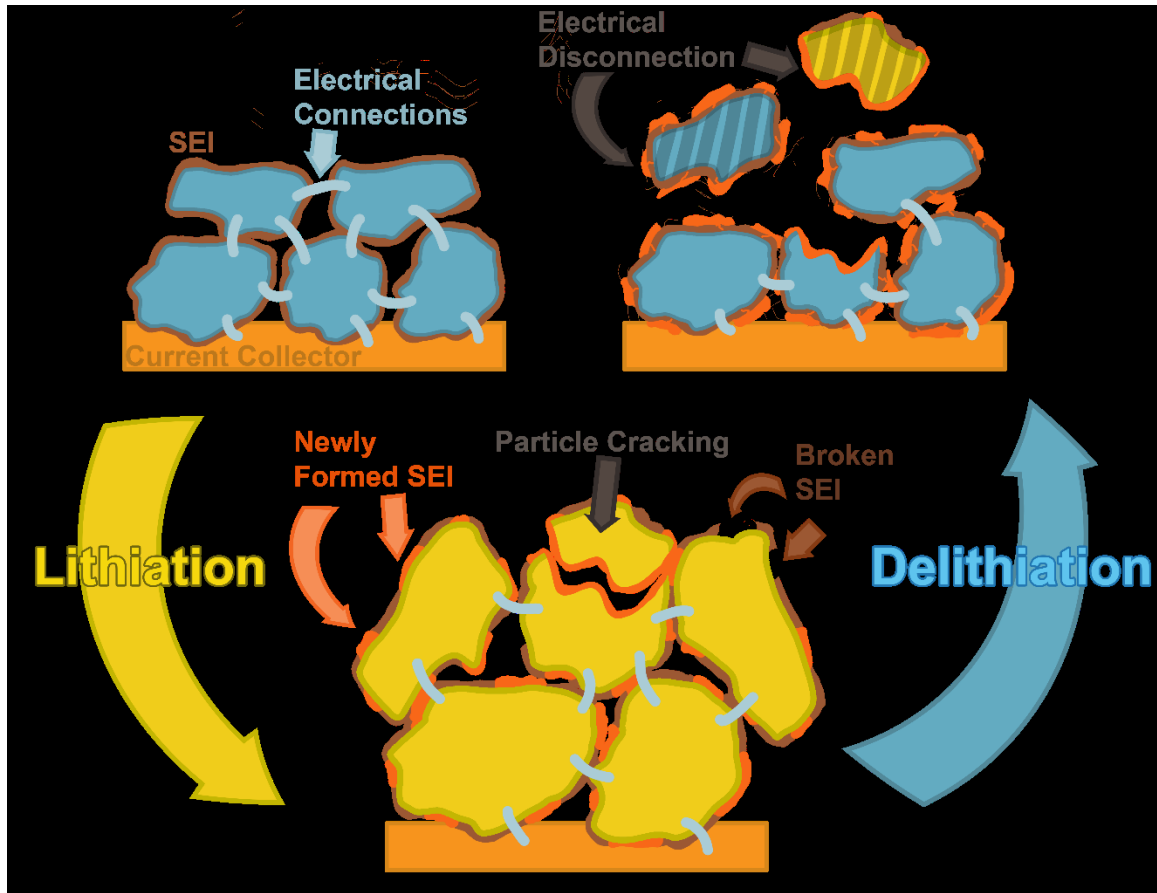


Figure 2.6: Illustration of Li-ion cell degradation mechanisms that affect lithium inventory. a) Schematic of an electrode composed of active particles (blue) on a current collector, with electrical connections shown with light blue lines, and an SEI layer (brown) that coats the surface of the particles. b) Electrode after lithiation—the particles have expanded, disrupting the SEI causing growth/repair. One particle has cracked due to the stress of volume expansion. c) Electrode after de-lithiation—a particle and fracture has become electrically disconnected, and the newly formed SEI has accumulated on the particles.

2.4.2 Loss of Active Material

Lithium ions are stored within the active materials of the positive and negative electrodes. If portions of these active materials become electrically disconnected from the cell, the stored lithium within these disconnected regions will be no longer accessible. This trapped lithium reduces the lithium inventory of the cell, decreasing cell capacity. Disconnection

can be caused by electrode particles delaminating from current collectors, loss of electrical contact between particles, and particle fracture/cracking. All of these mechanisms are exacerbated by large repeated volume expansion and contraction, and are known mechanisms of capacity loss for silicon electrodes.^{7,13,14} Loss of active material, of both the positive and negative electrode, is a degradation mechanism of Li-ion cells.^{32,33} This is schematically shown in Figure 2.6. In Figure 2.6b, an electrode which has experienced a large volume expansion is shown. Beaulieu et al. showed that electrodes which exhibit large volume expansions experience minimal lateral expansion parallel to the current collector.¹⁴ Therefore, the expansion occurs perpendicular to the current collector, resulting in a “shuffling” of electrode particles. This shuffling and subsequent un-shuffling upon de-lithiation, shown in Figure 2.6c, can result in loss of electrical contact between particles. Additionally, the stress of volume expansion can cause particles to fracture, as shown in Figure 2.6b. During de-lithiation, the fractured portions may no longer be electrically connected, as shown in Figure 2.6c. These processes result in loss of active material, decreasing the lithium inventory.

2.4.3 Degradation Effects on the Voltage vs. Capacity of Cells

To determine the effect of SEI growth/repair and mass loss on the measured voltage vs. capacity profiles of Li-ion cells, consider the example given by the lithium inventory schematic presented in Figure 2.7. This figure depicts a Li-ion cell in the discharged state; all 16 active lithium atoms in the inventory are stored within the positive electrode ($Q(P) = 16$). Additionally, there are 4 lithium ions within the electrolyte ($Q(E) = 4$) to facilitate ion transfer (solvated by solvent molecules), as well as one inactive lithium atom trapped in the SEI ($Q(S) = 1$).

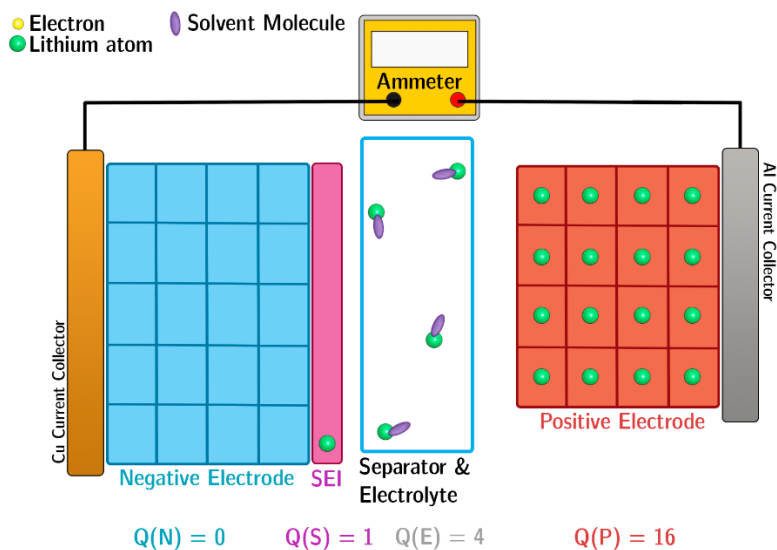


Figure 2.7: Schematic of the lithium inventory of a Li-cell.

During charge, lithium ions travel to the negative electrode, as shown in Figure 2.8a. In practice, the positive electrode is never fully de-lithiated to prevent it from reaching too high a voltage. Therefore, here the cell is shown to charge until 15/16 lithium ions leave the positive electrode, providing $15 e^-$ of capacity. As such, $15 e^-$ will be considered 100% capacity. The resulting voltage vs. capacity (plotted as state of charge (SOC), normalized full cell capacity * 100%) curve is shown in black in Figure 2.8b; the full cell has been charged to 100% capacity. It was demonstrated in Equation 2.7 of Section 2.1 that the voltage of a full Li-ion cell is the difference between the positive and negative electrode voltage. Therefore, the difference between positive and negative electrode voltage vs. capacity profiles shown in red and blue, respectively, produce the full cell voltage curve shown in black. If there are capacities where both a positive and negative electrode voltage do not simultaneously exist (i.e. no overlap), then no full cell voltage is possible and capacity cannot be delivered over that range. In Figure 2.8a, when the lithium ions reached

the negative electrode, 3 were involved in parasitic reactions and trapped in the SEI. This did not affect the full cell charge curve in Figure 2.8b since all 15 e⁻, even the 3 that recombined with Li inside the SEI, travelled through the external circuit, resulting in a 100% charge.

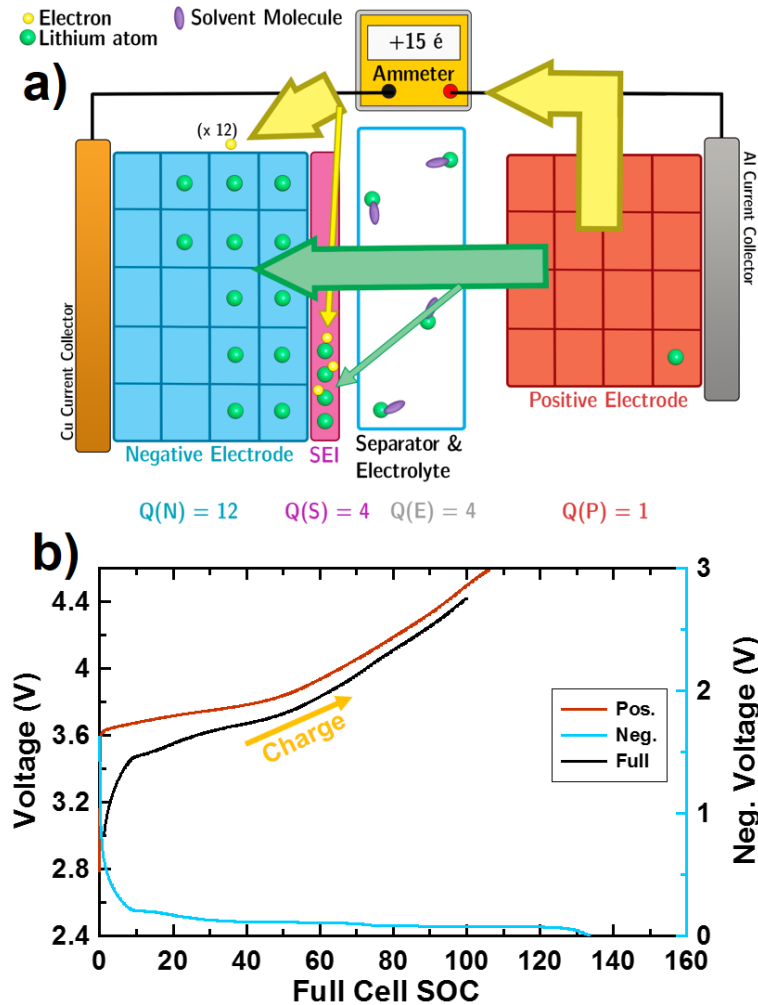


Figure 2.8: a) Lithium inventory schematic during charge. b) The resulting full cell voltage vs. state of charge (SOC) curve during charge (black). The difference between the positive (red) and negative (blue) electrode voltage curves yields the full cell curve.

Figure 2.9a shows the lithium inventory schematic during discharge following the cell state presented in Figure 2.8a. Since 3 lithium ions were trapped in the SEI, they are unavailable

to contribute to the discharge. Therefore, only 12/15 ions were available for discharge, resulting in a 20% (3/15) loss of capacity. Since the positive and negative electrode voltage curves add to produce the full cell curve, something must change such that the full cell curve only has 80% capacity. Neither electrode lost capacity; the positive electrode still has 16 available inventory slots, and the negative electrode still has 20 available inventory slots. Therefore, the electrode voltage curves cannot shrink. The inventory-consuming electrode-electrolyte reactions cause the electrode voltage curves to “slip” relative to each other, as shown in Figure 2.9b. Here, the negative electrode voltage curve (thick, light blue line) has shifted 20% from its original position (thin, navy line). This causes the full cell curve to slip accordingly since there is no more positive/negative overlap in this region; the full cell cannot discharge to 0% SOC since 20% capacity is no longer available, so the end of discharge slips by 20%. Accordingly, the capacity loss associated with lithium inventory consuming reactions and SEI growth is known as shift loss or loss due to slippage.

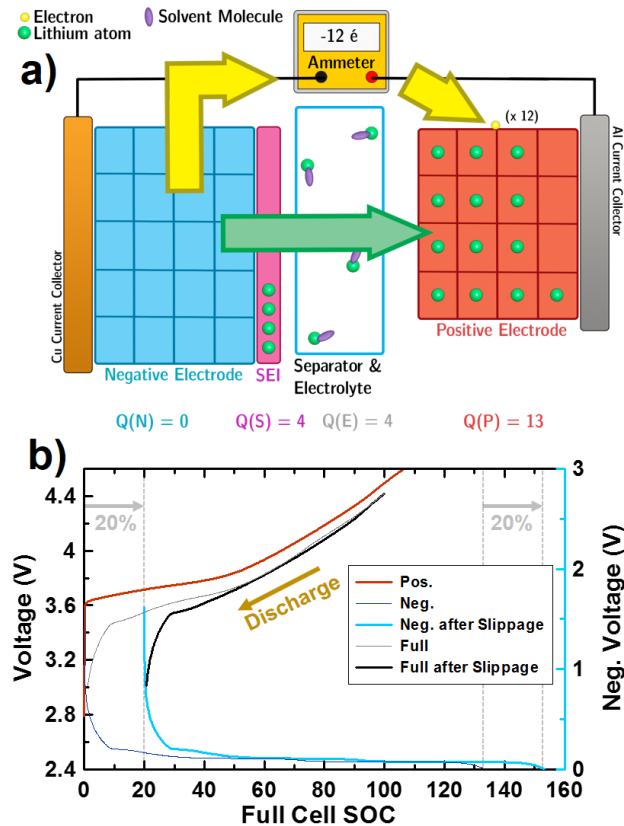


Figure 2.9: a) Lithium inventory schematic during discharge following Figure 2.8a. b) Corresponding voltage vs. capacity curves.

In addition to slippage, mass loss can occur which will also decrease the capacity of the full cell. This situation is demonstrated in Figure 2.10a. Here, the cell is discharging following the cell state depicted in Figure 2.8a. The effect of slippage has already been considered in the voltage vs. capacity curve shown in Figure 2.10b; the “initial” full cell and negative electrode curves shown in thin gray and thin navy, respectively, are the state of the voltage curves after the shift loss was considered shown in Figure 2.9b. Figure 2.10a depicts mass loss caused by portions of the negative electrode becoming electrically disconnecting, trapping two formally active Li. Therefore, a further 2/15 ions are unavailable, resulting in an additional ~13% loss. 3 Li have been trapped in the SEI due

to the previous shift loss, and now 2 have become trapped due to mass loss, resulting in a discharge capacity of $11/15 e^- = 67\%$. The negative electrode capacity has decreased as there are two less Li inventory slots available. This causes the negative electrode curve to shrink from 20/15 (133% of the full cell capacity) to 18/15 (120% of the full cell capacity), shown in Figure 2.10b, resulting in the further 13% loss in the full cell. The distinction between mass loss which causes electrode curves to shrink as shown in Figure 2.10b, and slippage or shift loss which causes electrode curves to shift as shown in Figure 2.9b is important to realize.

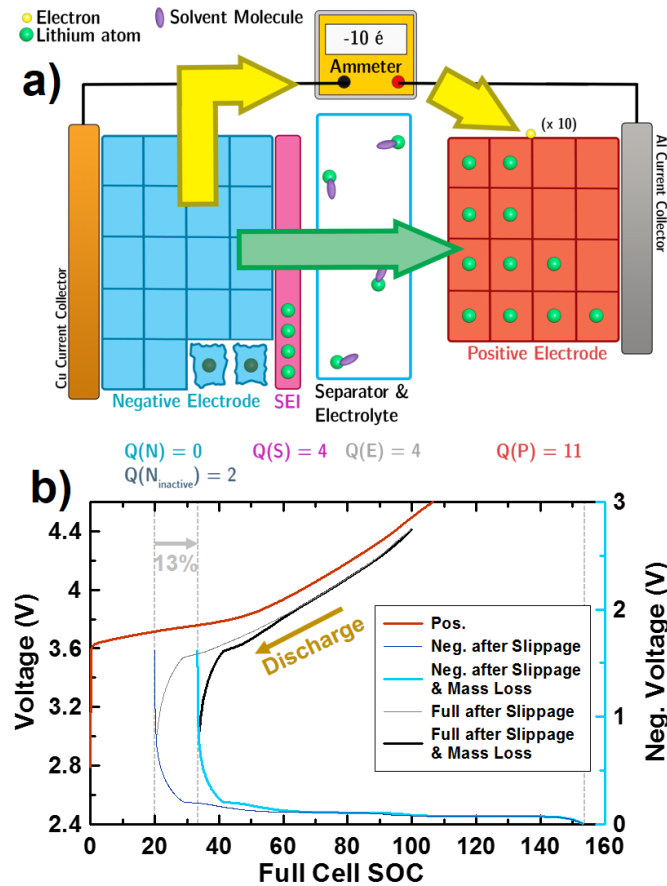


Figure 2.10: a) Lithium inventory schematic during discharge following Figure 2.8a, considering the effects of both slippage and mass loss. b) Corresponding voltage vs. capacity curves.

Mechanisms that do not decrease the active lithium inventory such as shuttle reactions and mass loss of de-lithiated particles have been omitted here.³² Further mechanisms of lithium inventory loss analogous to those presented in Figures 2.8-2.10 include positive mass loss, SEI growth during discharge and electrolyte oxidation.³² These have been omitted for simplicity and conciseness. Such mechanisms cause slippage and mass loss analogous to what has presented here, and are illustrated more completely in the excellent works by Smith^{32*} and Birkl.³³

Determining whether capacity loss is caused by electrolyte-electrode SEI forming reactions or mass loss is important to understand the degradation of Li-ion cells. Differential voltage analysis is a technique that can distinguish these loss mechanisms. This technique will be described in Section 3.2.

* To the keen reader who is interested in understanding *Interpreting High Precision Coulometry Results on Li-ion Cells*³² by Smith et al., please note there is an error in Table I of this work: in the “First discharge (Qd)” column, the capacity inventory for the Pos. electrode should read “ $Q_0 - 2q_{Li} + 2q_{ox}^a$ ” instead of “ $Q_0 - 2q_{Li} - 2q_{ox}^a$ ”.

Chapter 3: Experimental Methods

In this work, experiments were performed on rolled prismatic pouch cells and coin cells. This chapter details the preparation and experiments performed on such cells.

3.1 Cell Preparation

3.1.1 Pouch Cells

Machine-made rolled 402035 size (40 mm long, 20 mm wide x 3.5 mm thick) pouch cells were used in this work. These are the dimensions of the jelly roll of the cell, labelled in Figure 3.1. The jelly roll contains the components of a Li-ion cell described in Chapter 2, which are stacked together and wound to the desired dimension. Pouch cells were received sealed without electrolyte. Access to wet the jelly roll with electrolyte is made through the pouch bag, which is cut open and resealed for this purpose. The pouch bag also serves to collect any gas generated by the cell during operation, removing it from the jelly roll. Several different pouch cell chemistries were studied in this work, listed in Table 3.1.



Figure 3.1: Image of a Li-ion pouch cell.

Table 3.1: List of pouch cells used in this work.

Designation	Supplier Designation	Positive Electrode	Negative Electrode	Capacity (mAh)
Type A-i	Supplier A	NMC	AG	210
Type A-ii	Supplier A	NMC	NG	215
Type B	Supplier B	LCO	Si alloy-graphite	230
Type C	Supplier C	NCA	SiO-graphite	260
Type D-i	Supplier D	NCA	nano Si-C	165
Type D-ii	Supplier D	NCA	nano Si-C	205

Pouch cells were opened and placed in a vacuum oven at 100°C for 14 hours to remove any water contamination and then transferred into an argon-filled glovebox for electrolyte filling and sealing. Electrolyte was prepared in an argon-filled glovebox to minimize possible contaminations. Type A-i and A-ii cells were filled with 1.2 M LiPF₆ EC:EMC (3:7 by volume) with xPES211 (x = 1.0, 0.25). Type C cells were filled with EC:EMC:DMC (25:5:70 by volume) with 2% VC. Type B, D-i and D-ii cells were filled with 1.2 M LiPF₆ EC: EMC: FEC (27:63:10 by volume).

As discussed in Section 2.4.1, Li-ion cells undergo a formation process—a specialized charging protocol at the beginning of life to form a suitable SEI. In this work, formation began by wetting cells for 24 hours at 1.5 V. Cells were clamped with rubber blocks during formation to force any evolved gas outside the jelly roll and then were transferred to a Maccor series 4000 charger. Type A cells underwent formation according to the supplier’s recommended protocol which involved a single charge to 4.2 V and discharge to 3.8 V as

well as a storage step. Type B and C cells were charged to 4.2 V and back down to 3.8 V at C/20 (charged at a current corresponding to a charge time of 20 hours) without the storage step. Cells then were transferred into an argon-filled glove box and opened to remove any gas generated during the formation process and then resealed.

3.1.2 Coin Cells

2325-type (23.0 mm diameter, 2.5 mm thick) coin cells were prepared as half cells to measure the voltage profiles of each electrode materials (the working electrodes) vs. lithium metal, as shown in Section 2.2. The assembly of such coin cells is shown in Figure 3.2a. The electrode materials used as the working electrodes were punched directly from disassembled pouch cell electrodes, shown in Figure 3.2b. For the cell chemistries that employed composite negative electrodes, electrode material of each component was obtained and punched to make half cells.

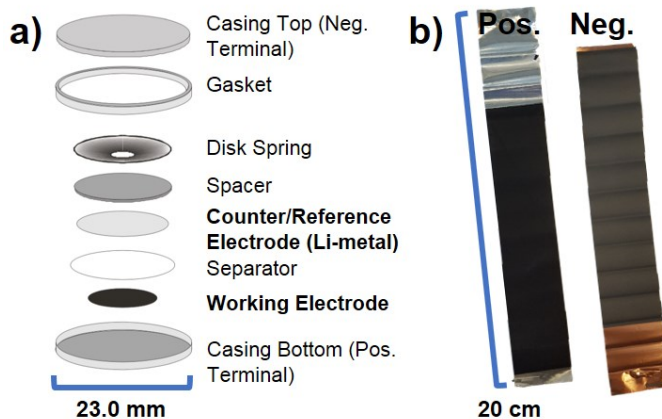


Figure 3.2: a) Components of a coin-type half cell. b) Electrodes removed from a pouch cell used to obtain the working electrode for the half cells.

The working electrodes were precision punched into 1.28 cm diameter disks. Two Celgard 2320 thin film polypropylene microporous films were used as separators. A 150 μm thick lithium metal foil (Chemetall, >99.99%) was punched into a 1.4 cm diameter disc to be used as reference electrodes. These components are shown in Figure 3.2a. 1M LiPF_6 EC:DEC (1:2 by volume) was used as electrolyte, fully wetting the electrodes and separators. Coin cells were assembled in an argon-filled glove box.

3.2 Electrochemical Testing

Pouch and coin cells were cycled (repeatedly charged and discharged) to obtain their voltage vs. capacity characteristics as well as capacity vs. cycle number data.

3.2.1 Pouch Cell Cycling

All original pouch cell cycling data presented in this work was performed accompanying an *in-situ* measurement, i.e *in-situ* volume, pressure or thickness measurements. Therefore, these experiments are detailed in Section 3.3 which describes the *in-situ* methods used in this work.

3.2.2 Coin Cell Cycling

To obtain voltage vs. capacity curves for each electrode material used in this work, as shown in Section 2.2, coin cell half cells were cycled on an E-One Moli Energy Canada battery testing system. Cells were cycled slowly as to minimize kinetic effects on cell performance. Charge/discharge rates of C/20 and C/40 (i.e. a charge time of 20 and 40 hours) were used.

3.2.3 dV/dQ Analysis

Section 2.4 discussed the degradation mechanisms that affect the lithium inventory of Li-ion cells. Differential voltage (dV/dQ) analysis is a technique used to quantify these mechanisms as Li-ion cells lose capacity during cycling. This technique was first introduced by Bloom et. al.³⁵ Since the full cell voltage curve of a Li-ion cell is the difference between the positive and negative electrode voltage curves, a measured full cell voltage curve can be fit by using a linear combination plus a relative shift of positive and negative electrode half cell voltage curves. The change in the relative shift needed to achieve a good fit is an indication of degradation due to SEI growth/repair, as shown in Section 2.4.3. The amount that the half cell voltage curves must shrink to achieve a good fit indicates the quantity of mass loss degradation, as shown in Section 2.4.3. Since the voltage vs. capacity curves of Li-ion cells and half cells are relatively smooth without distinct features (as shown in Figure 3.3c), fitting V vs. Q curves can be a difficult task. To amplify the features of these curves such that good fits can be easily determined, the derivatives, dV/dQ vs. Q, are used to perform these fits.

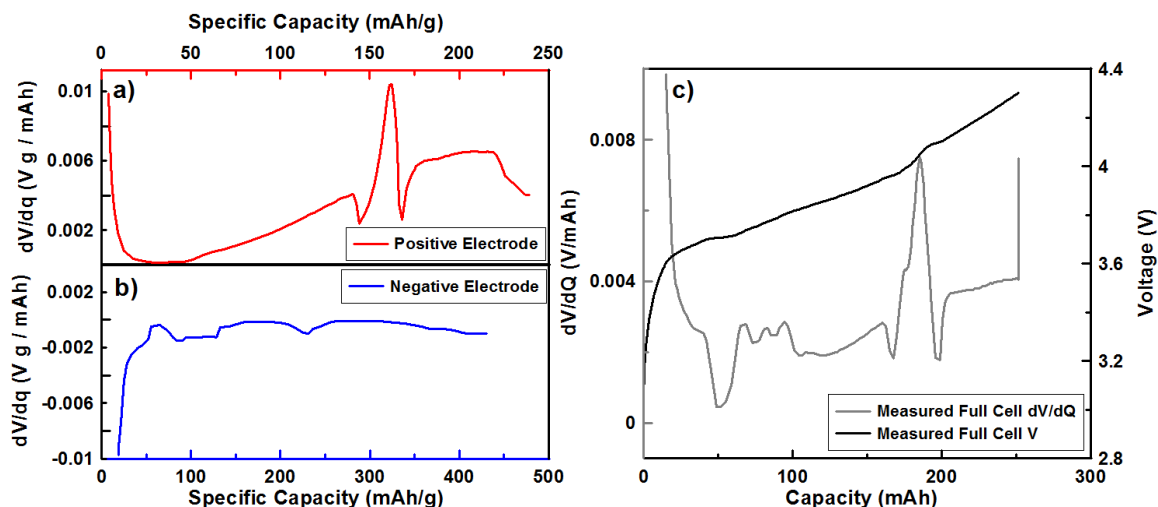


Figure 3.3: An example of the differential voltage vs. specific capacity curve for a) a positive electrode and b) a negative electrode. c) A measured differential voltage vs. capacity curve of a full cell.

The fitting process goes as follows: First, the differential voltage vs. specific capacity curves of each electrode must be obtained, as well as the differential voltage vs. capacity curve of the charge or discharge cycle to be analyzed. Examples of these curves are shown in Figure 3.3. Before the half cell curves in Figure 3.3a and b can be added to begin to attempt fitting the full cell curve shown in Figure 3.3c, the curves must be converted from specific capacity (units of mAh/g) to capacity (units of mAh) by multiplying by the electrode masses. Multiplying the specific capacity curves with a mass effectively stretches or shrinks the curves until they are the right size to make a good fit. The electrode masses within the pouch cells used in this work are on the order of 1 g, so this is a good starting guess. In Figure 3.4a, the half cell curves presented in Figure 3.3 are both multiplied by 1 g and are plotted in red and blue dashed lines. The difference between these curves is the calculated full cell dV/dQ vs. Q curve plotted in green.

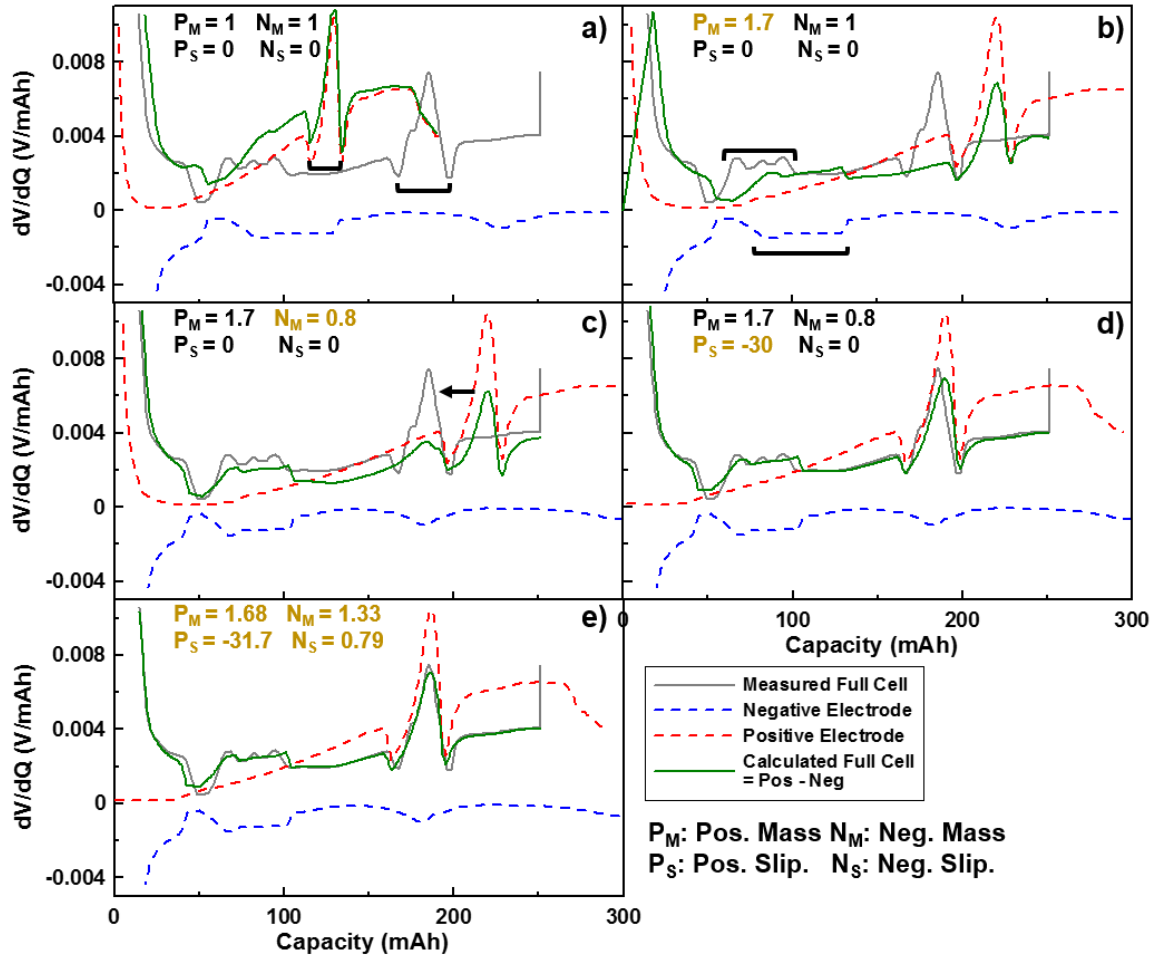


Figure 3.4: An example of the dV/dQ fitting process. In each panel, the fitting parameters (P_M , P_S , N_M , N_S) are changed to obtain a better fit. The fit quality improves from panel a) to panel e).

The goal of this fit is to match the calculated dV/dQ curve (green) to the measured curve (gray). From this first attempt in Figure 3.4a, it can be seen that the fitting parameters—the positive, negative mass and slippages, must be changed to obtain a good fit. First, the positive mass must be increased—this is obvious since the positive half cell curve (red) does not span the entire full cell curve. Additionally, there is a positive peak in the half cell curve which can also be seen in the full cell curve, both of which are indicated with

black lines. This peak is wider in the full cell curve, further indication that the positive curve must be stretched by increasing the mass.

The positive mass is increased to 1.7 g in Figure 3.4b. This results in better agreement between the widths of the positive peaks. There is a negative feature seen in both the negative half cell and full cell curves, indicated with black lines, that needs to be adjusted. This feature is too wide in the negative half cell curve, therefore the negative mass must be decreased.

The negative mass is decreased to 0.8 g in Figure 3.4c. The prominent positive and negative features seem to be the appropriate size, indicating that the chosen mass parameters are decent. Now, slippage must be considered. It is clear that the positive peak is too far to the right; it must be shifted, which is done by changing the positive slippage.

Figure 3.4d shows the result of slipping the positive half cell curve by -30 mAh. Now that a decent fit has been obtained, the slippage and mass values can be optimized by a computer algorithm. A user-friendly software to perform the transformations on dV/dQ curves as discussed above as well to optimize the fitting parameters was published by Dahn et al.³⁶ An updated version of this software has been developed by Asher Wright. The work done in this thesis uses the software by Wright. Using this software, the fitting parameters used in Figure 3.4d are optimized to obtain a better fit shown in Figure 3.4e.

The fitting shown in Figure 3.4 yields the mass of the positive and negative electrodes as well as a positive and negative slippage for a specific charge cycle. Monitoring these parameters from cycle to cycle will elucidate the degradation mechanisms experienced by the cell. If the electrode masses are found to decrease over cycle count, then electrode

degradation such as particle disconnection or cracking has occurred, as illustrated in Figure 2.6. The change in positive and negative electrode slippage over cycle count is the amount that each of the electrode voltage vs. capacity curves has shifted in mAh, as demonstrated in section 2.4.3, quantifying the amount of capacity that has been lost due to SEI growth and repair. Example of this type of analysis can be found in the works by Dahn,³⁶ Fathi,³⁷ and Petibon.²⁰

The dV/dQ analysis software by Wright used in this thesis always defines a fully discharged cell to be at 0% state of charge, in contrast to the examples presented in Section 2.4.3. In the example presented in Figure 2.9, electrode slippage caused a 20% capacity loss. This example illustrated a discharge, therefore the cell went from fully charged at 100% SOC to 20% due to the capacity loss. Since the program by Wright always defines the end of discharge to occur at 0% SOC, this scenario presented in Figure 2.9 would be shown instead as discharging from 80% to 0%.

3.3 *In-situ* Electrode Expansion Measurements

The volume expansion and contraction of alloy negative electrodes has been previously measured using *in-situ* AFM.^{13,14,38} Electrochemical dilatometry is another technique that has been used to measure electrode expansion during cycling. This has been performed on graphite half cells,³⁹ Si composite half and full cells,^{40,41} and SiO half cells.²³ This technique is rarely performed on full cells,¹⁸ thereby only observing the volume expansion of a single electrode. Additionally, these *in-situ* techniques utilize a specially made wet cell for their measurements—a Li-ion cell that would never be used practically outside of

the lab. This tends to limit the ability of these experiments to perform long-term measurements; generally, only short term cycling is possible.

In this work, *in-situ* techniques for measuring the effect of electrode expansion on practical Li-ion full cell pouch cells are presented. In full pouch cells, the contribution of both the positive and negative electrode interplay resulting in a net expansion. This work presents measurements of the volume, pressure and thickness evolution of Li-ion pouch cells in Chapter 4. Additionally, long term cycling experiments are possible with these techniques, as demonstrated with long-term pressure evolution measurements in Chapter 5.

3.3.1 Volume Measurements

In-situ volume measurements were made via Archimedes' principle in the apparatus first described by Aiken et al.,⁴² pictured in Figure 3.5. Pouch cells were suspended in silicon mechanical pump oil from a thin film load cell which measures the tension caused by the suspended cell. The tension measured by the load cell ($F_{tension}$) is equal to the difference between the buoyant force acting on the cell ($F_{buoyant}$) and the weight of the cell (F_{weight}).

$$F_{tension} = F_{buoyant} - F_{weight} \quad (3.1)$$

A change in cell volume will cause the buoyant force to change, but the cell weight will remain constant. Therefore, the load cell will experience a change in tension.

$$\Delta F_{tension} = - \Delta F_{buoyant} \quad (3.2)$$

The change in tension is recorded by the load cell as a change in mass since $\Delta F_{tension} = \Delta m_{load\ cell} g$, where g is the gravitational constant. The change in the buoyant force is a

product of the gravitational constant, the change in cell volume Δv , and the density of the oil ρ .

$$\Delta m_{balance} g = - \rho \Delta v g \quad (3.3)$$

Therefore, the change in cell volume can be calculated:

$$\Delta v = - \Delta m_{balance} / \rho \quad (3.4)$$

The pouch cells measured in these experiments had an initial volume of *ca.* 2.5 mL. For *in-situ* measurements, the pouch cells were connected to a Maccor Series 4000 battery charger. The load cell output was connected to a Keithley 2700 scanning voltmeter. These measurements were made in a temperature box at 40°C. Cells tested here first experienced a formation procedure, as discussed in Section 3.1, before being transferred to this system for charge/discharge cycling from 3-4.2 V.

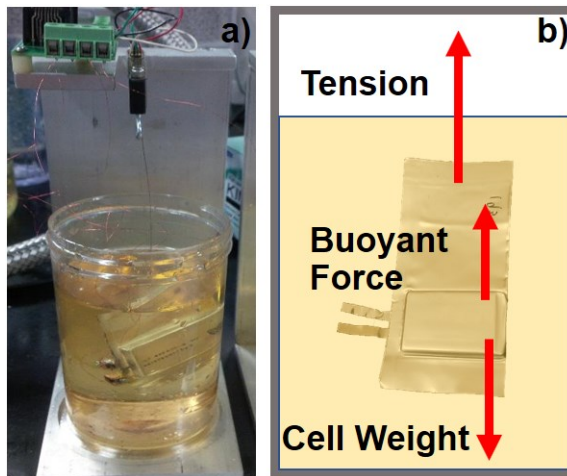


Figure 3.5: *In-situ* volume measurement apparatus; a) pictured in left panel, b) shown schematically the right panel.

3.3.2 Pressure Measurements

For *in-situ* pressure measurements, pouch cells were fastened inside rigid aluminum holders (colloquially referred to as superboats), pictured in Figure 3.6a, such that electrode volume expansion would cause an increase in force exerted on the enclosure. With this holder design, any gas evolved during cycling would be pushed out of the jelly roll into the pouch bag and not cause a change in measured pressure. The force was measured with subminiature load cells (model LCKD - OMEGA Engineering) with capacities of 100, 250, and 500 lbs (445, 1112 and 2224 N), connected to DP25B-S-A (OMEGA Engineering) strain gauge panel meters. The measured force was converted to PSI using the pouch cell area of *ca.* 0.93 in² (6.0 cm²). The load cells were fastened inside the aluminum enclosures, in-between the wall of the enclosure, a force-distributing plate, and the pouch cells, shown in Figure 3.6b. The position of one wall of the superboat enclosure is adjustable with screws. This allows the superboats to accommodate cells of different thicknesses as well as allowing the application of a different initial pressure by tightening the screws to different pressures. The pressures achieved in this work, about 20-200 PSI (~140-1400 kPa), correspond to an elastic response of the system (load cell, pouch cell and force distributing plate) of about 15-100 μm . This was determined by measuring the compliancy of the system, shown in the appendix in Figure A.1. For *in-situ* measurements, the pouch cells were connected to an E-One Moli Energy Canada battery testing system. The analog 0-10 V output of the strain gauge panel meter was connected to a Moli slave channel, allowing for simultaneous voltage and pressure measurements. These measurements were made in a temperature box at 40°C. Cells tested here first experienced a formation

procedure, as discussed in Section 3.1, before being initialized in superboats at 3.8 V and transferred to the Moli system for charge/discharge cycling from 3-4.2 V.

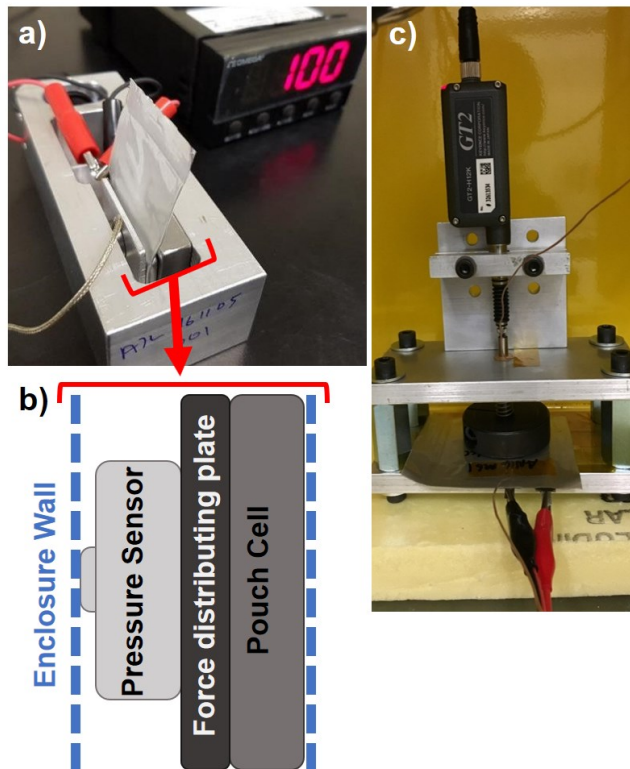


Figure 3.6: *In-situ* pressure and thickness measurement apparatus. a) Pressure measurement apparatus; b) schematic of pressure measurement apparatus; c) thickness measurement setup.

3.3.3 Thickness Measurements

An *in-situ* thickness measurement was made for a single stack (i.e one positive and one negative electrode) pouch cell of the chemistry used in Type C cells in the apparatus shown in Figure 3.6c. The cell was secured to a flat aluminum stage, and a displacement sensor (Keyence GT2) was used to measure the cell thickness changes during charge and discharge cycling. A spring was applied to the displacement pin to minimize noise from

inconsistencies in the pouch. This measurement was performed at room temperature. The first half cycle of this test was a formation step, as no prior formation procedure was performed on this cell. One cycle of discharge charge cycling followed between 3-4.2 V. This measurement was performed by Christopher Fell (Tesla Motors), not by the author.

Chapter 4: The Effect of Electrode Volume Expansion on Full Li-ion Pouch Cells[†]

Upon lithiation and de-lithiation, the electrode materials used in Li-ion cells change in volume. In the extreme case, silicon expands by 280% upon lithiation,¹³ whereas graphite only expands by 10%.⁶ Positive electrode materials tend to experience volume changes of only a few percent.^{43,44} Contrary to the behavior of silicon and graphite, some materials, such as NCA and NMC, contract upon lithiation and expand upon de-lithiation. The expansion and contraction of the constituent electrode materials of a full Li-ion cell within a compliant cell format such as a pouch cell will result in a net volume change during charge and discharge of the cell. Electrode volume expansion within a non-compliant cell design, such as in the hard casing of a cylindrical cell, will result in an increase of pressure within the cell. This is a concern for Li-ion cell manufacturers who need to allocate space for this volume expansion.

In this chapter, the volume change of pouch cells with various electrode chemistries is measured during charge and discharge. The pressure evolution of these cells when they are volumetrically constrained, mimicking the conditions within a cylindrical cell, is also measured. *In-situ* thickness measurements are made on one single stack pouch cell of the chemistry used in Type C cells. An understanding of the resulting volume, pressure and

[†] Some of the results presented in this chapter were published in A. J. Louli, Jing Li, S. Trussler, Christopher R. Fell, and J. R. Dahn, Volume, Pressure and Thickness Evolution of Li-Ion Pouch Cells with Silicon-Composite Negative Electrodes, *J. Electrochem. Soc.*, 164 (12) A2689-A2696 (2017). doi: 10.1149/2.1691712jes, for which the author wrote the first draft of the entire manuscript. The contributions of the co-authors are indicated in figure captions where appropriate. Reproduced by permission of ECS – The Electrochemical Society.

thickness profiles is made by considering the effect of the constituent electrode materials within the full cell.

4.1 *In-situ* Volume, Pressure and Thickness Measurements

Figure 4.1 shows the *in-situ* volume (top row) and pressure (bottom row) measurements for Type A-i, A-ii and B cells in each column. Figure 4.2 shows these measurements for Type C, Type D-i and D-ii cells shown in each column, as well as an *in-situ* thickness measurement made on a Type C chemistry cell shown in the third row. The voltage vs. time curves for each measurement are shown in black using the left axis, and the corresponding *in-situ* measurements are shown in red using the right axis. The *in-situ* data is purposely scaled for a comparison of the shape of each profile and not their relative size, therefore the scaling of the volume/pressure/thickness axes are not consistent between cell types. Two cycles are shown for each measurement (in the cases where such data was available) to demonstrate repeatability. Only 1.5 cycles of the volume measurements for Type A-i and A-ii cells and 1.5 cycles of the thickness measurement for the Type C cell was available. All other data shows the first two cycles after formation. The first charge of the thickness measurement of the Type C cell corresponds to a formation step, and thus is not representative of the thickness evolution post-formation.

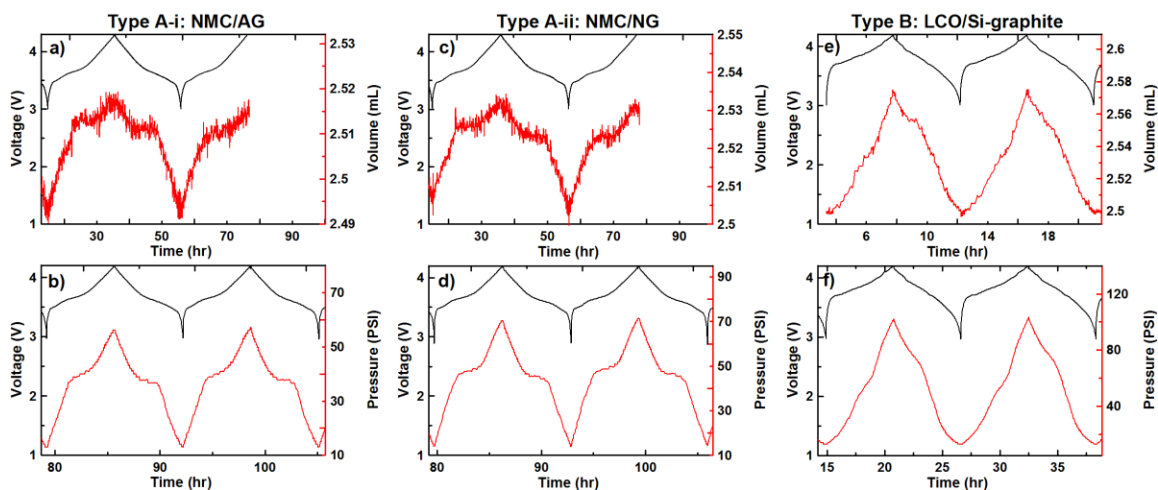


Figure 4.1: *In-situ* volume and pressure measurements for Type A-i (NMC/AG) (a-b), Type A-ii (NMC/NG) (c-d) and Type B (LCO/Si-graphite) (e-f) cells.

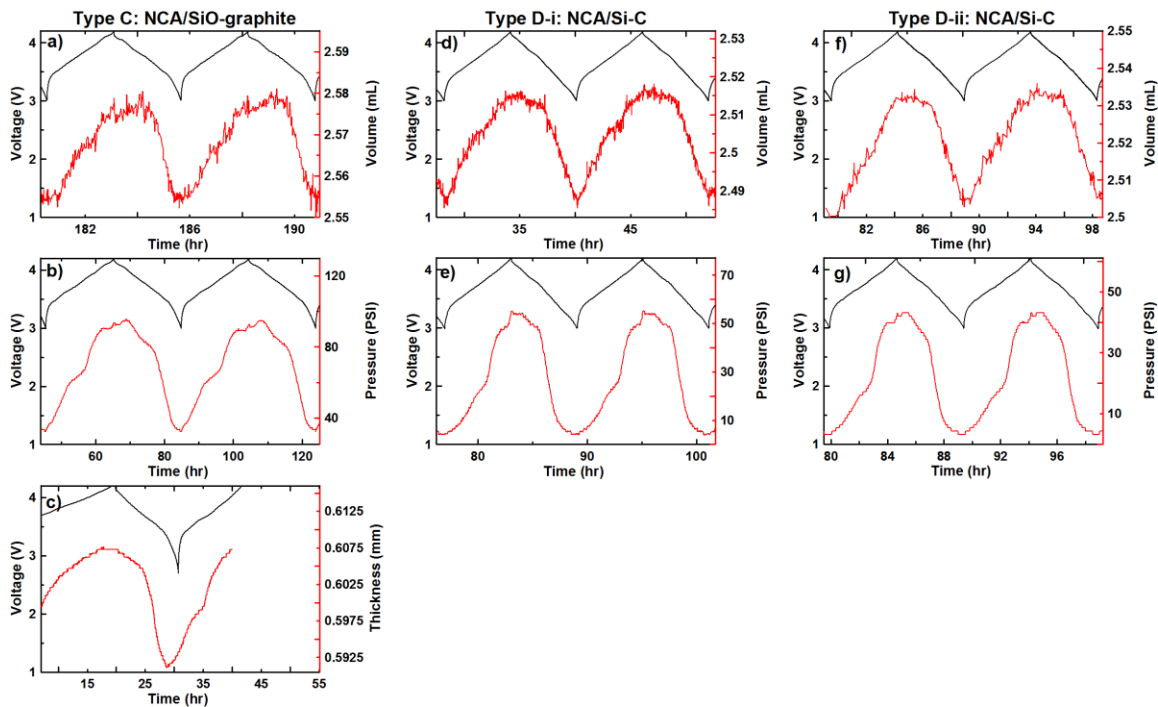


Figure 4.2: *In-situ* volume, pressure and thickness measurements for Type C (NCA/SiO-graphite) (a-c), Type D-i (NCA/Si-C) (d-e) and Type D-ii (NCA/Si-C) (f-g) cells. The thickness data shown in panel c) was measured by Christopher Fell (Tesla Motors).

The *in-situ* measurements for each respective cell type shows good agreement between the trends observed in the volume, pressure and thickness measurements. Therefore, the observed behaviour in each case can be confidently attributed to the same phenomenon—the net constituent electrode volume change during charge and discharge. During charge, the negative electrode is lithiated, causing a volume expansion. For pure graphite negative electrodes, this is a 10% expansion due to lithium intercalation into graphite. For composite negative electrodes, there is a portion of the expansion due to lithium intercalation in graphite, as well as a portion due to lithium alloying with silicon resulting in a 280% expansion of the silicon component. The negative electrode volume expansion causes the jelly roll of the pouch cell to expand in the direction perpendicular to the current collector, i.e. the short axis of the jelly roll. For the respective measurements made in Figures 4.1 and 4.2, this yields a volume expansion, an increase in pressure, and an increase in thickness—and the opposite on discharge. The expansion and contraction profiles are different for different cell chemistries due to the differences of electrode material expansion and contraction during lithiation and de-lithiation. To understand the expansion behavior of each chemistry, the contribution of each electrode component must be considered. This is done in the sections that follow.

4.2 Volume Expansion of Cells with Graphite Negative Electrodes

Figure 4.1 shows the expansion profiles for Type A-i and A-ii cells which use a single component graphite negative electrode (AG for A-i, NG for A-ii) paired with a NMC positive electrode. These cells show a virtually identical expansion profile. Since both cell types use the same chemistry, with only the type of graphite differing, this is not

unexpected. This shows that the type of graphite—artificial or natural—does not affect how the negative electrode changes in volume during cycling. The expansion profiles of Type A-i and A-ii cells are symmetric, exhibiting a plateau midway through charge and discharge as well as a peak at the top of charge. To understand these features, the volume expansion of each electrode is now considered.

4.2.1 Negative Electrode Expansion

The lattice constants of graphite were measured as a function of x in Li_xC_6 by Dahn using *in-situ* x-ray diffraction (XRD),⁶ from which the average spacing of carbon layers was calculated. Graphite has a hexagonal unit cell, therefore, the cell volume per layer, V_u , can be calculated as:

$$V_u = a^2 d_{002} \sqrt{3/2} \quad (4.1)$$

where a is in-plane lattice constant that remains relatively unchanged during lithium intercalation, and d_{002} is the distance between carbon layers, measured in Ref.⁶. Since the volume is linear with d_{002} , normalizing the data from Ref.⁶ gives the fractional volume of Li_xC_6 versus x , where x is equivalent to the state of charge of graphite. This is presented in Figure 4.3. This shows that when graphite is fully charged (SOC = 1), it undergoes a *ca.* 10% volume expansion. The highlighted region corresponds to the cycling range of graphite within the full NMC/graphite cell: 0 to 71% SOC. Therefore, through the range cycled in the full cell presented in this work, graphite undergoes a volume expansion of slightly less than 8%.

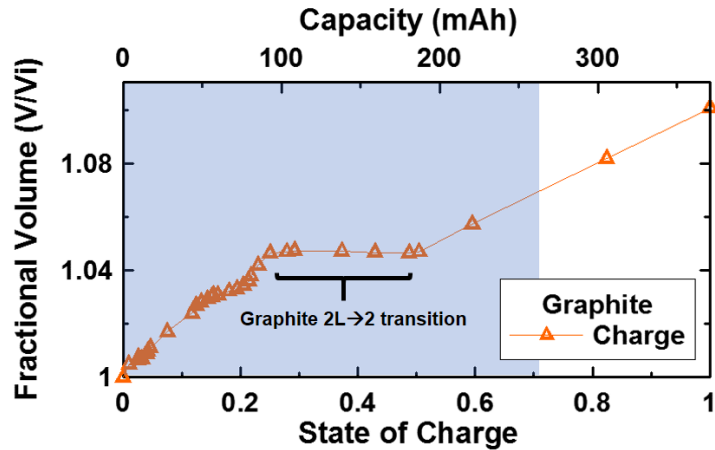


Figure 4.3: Fractional volume expansion of graphite during charge, adapted from data in Ref.⁶ by Dahn. The highlighted region corresponds to the cycling range of graphite within the full cell: 0 to 71% SOC.

The volume expansion of graphite experience a plateau between 25 and 50% SOC. This is a result of how lithium intercalates into graphite. Between $\text{Li}_{0.25}\text{C}_6$ and $\text{Li}_{0.5}\text{C}_6$, graphite undergoes a phase transformation from stage $2\text{L} \rightarrow 2$. Both of these stages have lithium atoms intercalated into every second interstitial layer between carbon layers. Stage 2L is a partially filled phase with disordered Li arrangement that transitions into stage 2 which is a fully filled phase with ordered Li arrangement. Since this transition does not involve lithium intercalating into any empty interstitial layers, there is no volume expansion that occurs throughout this transition.⁶

4.2.2 Positive Electrode Expansion

Weber et al. measured the volume contraction of $\text{Li}(\text{Ni}_{0.5}\text{Mn}_{0.3}\text{Co}_{0.2})\text{O}_2$ (NMC 532, the grade of NMC used in this work) using *in-situ* XRD.⁴⁵ The lattice constants a and d_{002} were measured to calculate the unit cell volume in angstroms using Equation 4.1, which was then normalized to plot Figure 4.4. The orange triangles show the results of this

experiment. *In-situ* data from Weber et al.⁴⁵ was not available for SOC < 10%, so measured lattice parameters for NMC532 in the discharged state (SOC = 0) from Li et al. from Ref.⁴⁶ was used to calculate the volume for the red circle data point at SOC = 0. The cycling range of NMC within the full cell tested in this work is highlighted. Within this region, NMC experiences a volume contraction on charge of *ca.* 3%.

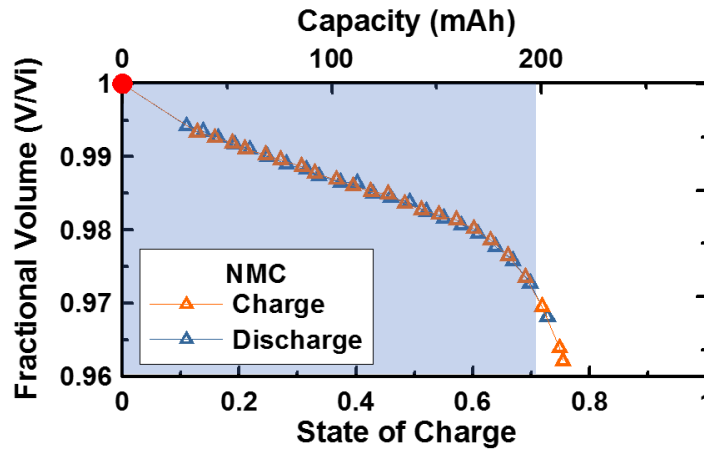


Figure 4.4: Fractional volume expansion of NMC during charge measured by Weber et al.⁴⁵ The highlighted region corresponds to the cycling range of graphite within the full cell: 0 to 71% SOC.

4.2.3 Predicted Full Cell Expansion

Now that all the contributions to electrode volume expansion for the NMC/graphite Type A-i and A-ii cells are known, their sum contribution can be calculated to predict the net volume expansion of a full cell of this chemistry. To calculate the change in volume for graphite and NMC in a full cell, the initial volume of each electrode must be known. This can be calculated using the initial active mass of each electrode derived from dV/dQ fitting—0.877 g for graphite and 1.158 g from NMC—and dividing that by the respective electrode densities—2.266 g/mL for graphite and 4.731 g/mL for NMC. This yields an

initial volume for graphite and NMC of 0.387 mL and 0.245 mL respectively. Multiplying this by the fractional volume expansion of each component presented in Figures 4.3 and 4.4, and subtracting the initial volume of each yields the change in volume, shown in Figure 4.5 in blue for graphite and red for NMC. These two contributions are then added together to calculate the predicted volume expansion of a full cell, shown in magenta. The change of volume is plotted against the capacity of the full cell during charge (0-199 mAh, left panel) and discharge (199-0 mAh, right panel), with the corresponding voltage profile of the cell shown in green in the top panel.

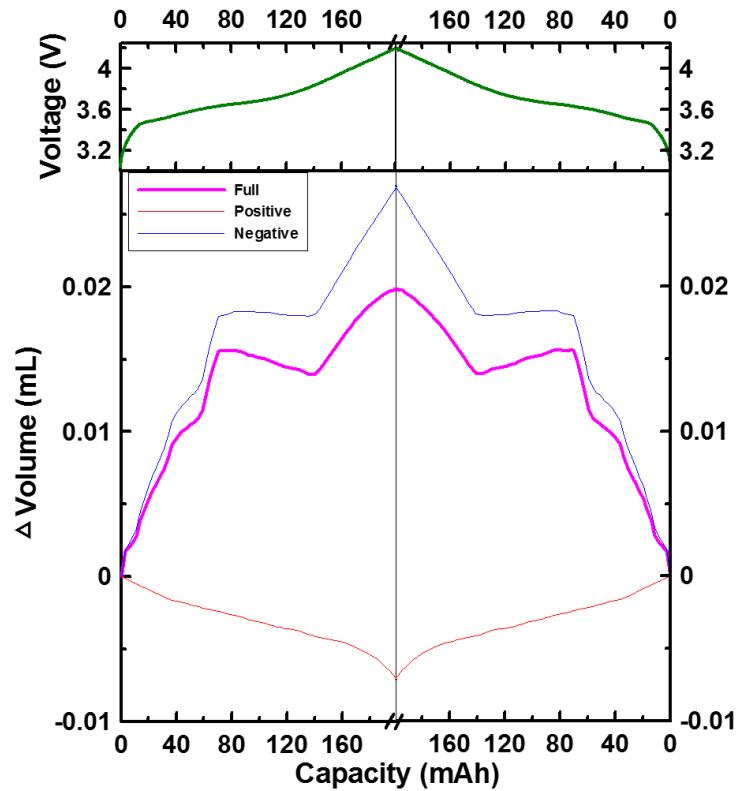


Figure 4.5: Predicted change in volume of a full NMC/graphite cell shown in magenta during charge (bottom left) and discharge (bottom right), with the corresponding voltage vs. capacity curve shown in the top panel in green. The change in volume of the graphite negative electrode is shown in blue, the NMC positive electrode in red, and their sum—the predicted net volume change of a full cell—in magenta.

This shows good qualitative agreement with the measured volume expansion of the NMC/graphite cells shown in Figure 4.1 a-d. These calculations elucidate the expansion behavior of Type A-i and A-ii cells. The major features in the expansion profiles can be attributed to graphite expansion and contraction. The graphite 2L \rightarrow 2 and 2 \rightarrow 2L transitions causes a plateau during charge and discharge in the otherwise relatively linear expansion and contraction profile of the full cell. The magnitude of the predicted volume expansion of the full cell also shows decent agreement—0.02 mL compared to the experimental value of *ca.* 0.03 mL

4.3 Volume Expansion of Cells with Silicon-Composite Negative Electrodes

Type B, C, D-i and D-ii cells use composite negative electrodes containing silicon and a form of carbon. This composite is Si alloy-graphite for Type B cells, SiO-graphite for Type C cells, and carbon coated n-Si for Type D-i and D-ii cells. Type B cells are paired with a LCO positive electrode, while Type C and D cells are paired with NCA positive electrodes. Figure 4.1e and f and Figure 4.2a-g show that these cells have similarities in their expansion profiles. There is a particular similarity between the profiles of Type C and D cells that employ the same positive electrode chemistry. It is no surprise that Type D-i and D-ii cells have identical expansion profiles since they employ the exact same electrode chemistry—these cell types only differ in electrode thickness. In contrast to the NMC/graphite cells reported in Section 4.2, the expansion profiles of all silicon-containing cells are asymmetric. The expansion profiles of these cells experience a plateau during charge and discharge, the latter occurring at a higher volume/pressure/thickness than the

former. NCA-containing Type C and D cells also experience a plateau at the top of charge, whereas the LCO Type B cell does not.

In what follows, a comprehensive analysis on the contributions to volume expansion of each electrode component is performed for the Type C NCA/SiO-graphite chemistry to elucidate the measured expansion profile of silicon-containing cells.

4.3.1 Type C Positive Electrode Expansion

The volume expansion of NCA was measured using *in-situ* XRD with the same methods discussed previously in sections 4.2.1 and 4.2.2. These measurements were performed by Jing Li (Dalhousie University), not the author. The fractional volume expansion of NCA is presented in Figure 4.6. Within the full Type C cell, the NCA positive electrode cycles between about 20-97% SOC, as highlighted in Figure 4.6, corresponding to a *ca.* 4.5% volume contraction and expansion during charge and discharge respectively. The volume change of NCA is relatively benign until the top 15% of SOC where rapid volume contraction occurs.

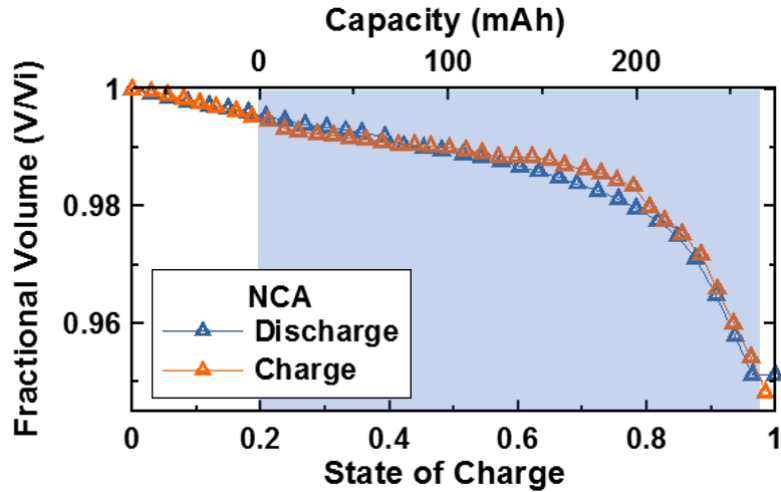


Figure 4.6: Fractional volume expansion of NCA during charge (orange) and discharge (blue). The highlighted region corresponds to the cycling range of NCA within the full cell: 20 to 97% SOC. This data was collected by Jing Li (Dalhousie University).

4.3.2 Type C Negative Electrode Expansion

The negative electrode volume expansion is more complicated for a composite chemistry since the contributions of both components—graphite and SiO for Type C cells—need to be understood separately. Figure 4.7a shows the fractional volume expansion of graphite, which is the same as presented in Figure 4.3, with only the highlighted cycling range changed here to match the cycling range of the negative electrode for the Type C full cell chemistry: 3 to 84% SOC.

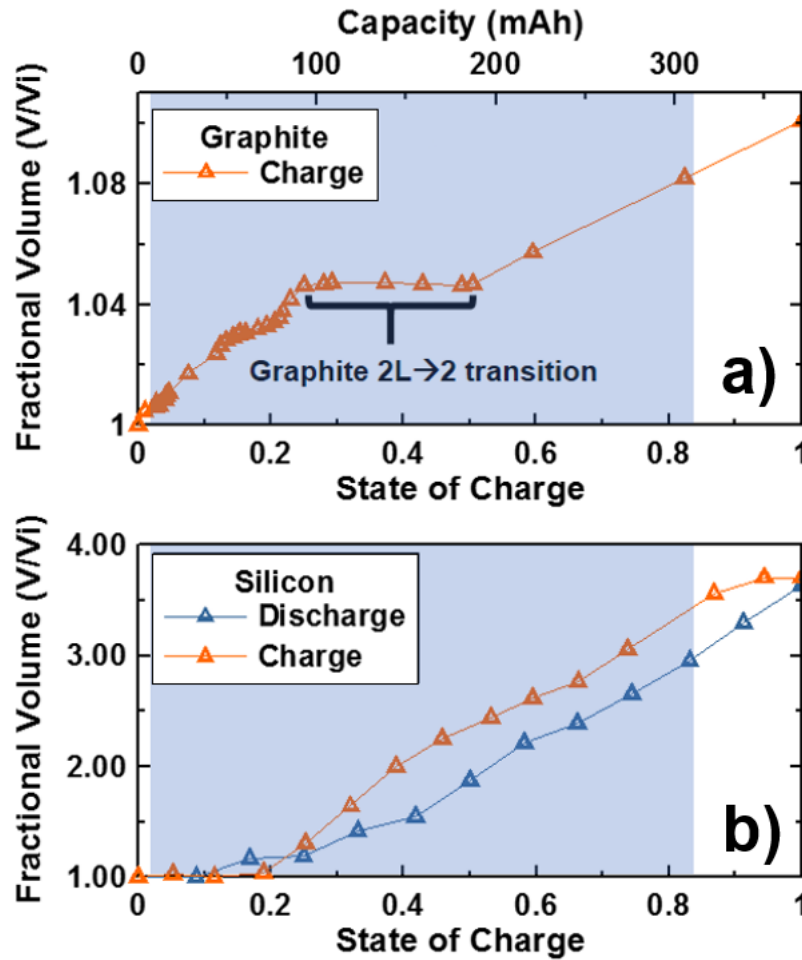


Figure 4.7: a) Fractional volume expansion of graphite during charge adapted from Ref.⁶. b) Fractional volume expansion of amorphous silicon during charge and discharged adapted from Ref.¹³. The highlighted regions correspond to the cycling range of the negative electrode within the full cell: 3 to 84% SOC.

Figure 4.7b shows the fractional volume expansion of amorphous silicon (a-Si), adapted from data taken from Ref.¹³. In Ref.¹³, Beaulieu et al. measure the volume expansion of a sputtered amorphous silicon tower with *in-situ* AFM using a specially made wet cell vs. lithium metal. The following analysis assumes that the fractional volume vs. state of charge of the a-Si tower shown in Figure 4.7b is the same as the volume expansion of the SiO electrode component of Type C cells. Previous studies have shown that SiO consists

of a nanostructure of a-Si and a-SiO₂ in a 1:1 ratio.²¹ During first charge/discharge, lithium irreversibly reacts with SiO₂ to form Li₄SiO₄ and Si. The Li₄SiO₄ remains inactive throughout subsequent cycling while the amorphous n-Si is reversibly lithiated and de-lithiated.^{21,23,24} Therefore, the volume expansion and contraction of SiO during charge/discharge cycling post-formation is caused by a-Si lithiation and de-lithiation.²³ As such, the data from Ref.¹³ is appropriate for this analysis. Figure 4.7b shows that the expansion of silicon is relatively linear. It expands by 280% when fully charged and by about 200% in the cycling range within the full cell of 3-84% SOC. Although Figure 4.7b shows an apparent hysteresis between charge and discharge, it is the opinion of the author that this is not due to a physical difference in the expansion and contraction of a-Si, but rather due to the inherent experimental error in the original AFM experiment.

To determine the expansion of the entire composite negative electrode, the contribution of both the graphite and SiO components must be resolved. Figure 4.7 shows the fractional expansion of these components vs. their SOC, however, the states of charge of each of these components within the composite negative electrode will not be the same during cycling. This is because each component is lithiated differently at different voltages, as can be seen in the dQ/dV vs. V plot during charge in Figure 4.9a and discharge in Figure 4.9b for graphite and SiO shown in red and blue respectively. Integrating the dQ/dV vs. V curves yields the capacity that has been delivered up to a certain voltage for each respective electrode component. This shows that the capacity delivered from each component is not uniform. For the components of a composite electrode, the state of charge (SOC) is the normalized capacity of each respective component that has delivered to the total composite

electrode capacity.[‡] Each component will experience the fractional volume change shown in Figures 4.7a and b at their respective states of charge in the composite negative electrode. Therefore, the states of charge of each component within the composite negative electrode during charge/discharge, as a function of the composite electrode capacity, must be determined. To this end, dV/dQ analysis was used to fit the contribution of each component to the composite electrode capacity using the method outlined in Section 3.2.3, the results of which are shown in Figure 4.8. Half cells of the full composite negative electrode, the graphite component, and the SiO component were cycled vs. lithium metal as reference data for this analysis. The graphite and SiO component reference data ($Q_{neg,i}(V)$ and $Q_{neg,j}(V)$), shown in red and blue respectively, were combined as a function of voltage to fit the measured composite electrode data ($Q_{neg}(V)$) in Figure 4.8.

$$Q_{neg}(V) = Q_{neg,i}(V) + Q_{neg,j}(V) \quad (4.2)$$

The result is good fit, shown in solid magenta, to the measured data, shown in dotted purple. This shows the capacity contribution of each component to the composite negative electrode. From this, the state of charge of each component (SOC_i) can be calculated as the ratio of the capacity of each component ($Q_{neg,i}$), as a function of the composite negative electrode capacity (Q_{neg}), with the maximum capacity that component delivers ($Q_{neg,i}^{max}$):

[‡] For example, if when the composite negative electrode was fully charged, the SiO component could receive 10 mAh of capacity and the graphite component could receive 100 mAh of capacity, then the composite electrode could store 110 mAh of capacity when fully charged. At a certain point during charge of the composite negative electrode, say at 55 mAh—half way through charge, the SiO component had received 7 mAh of capacity and the graphite component had received 48 mAh of capacity, then their respective states of charge would be 70 and 48% when the composite negative electrode was half way through charge at 55 mAh.

$$SOC_i(Q_{neg}) = Q_{neg,i}(Q_{neg}) / Q_{neg,i}^{max} \quad (4.3)$$

One must realize that component capacity \neq composite electrode capacity; component SOC \neq composite electrode SOC; and component SOC \neq composite electrode capacity.

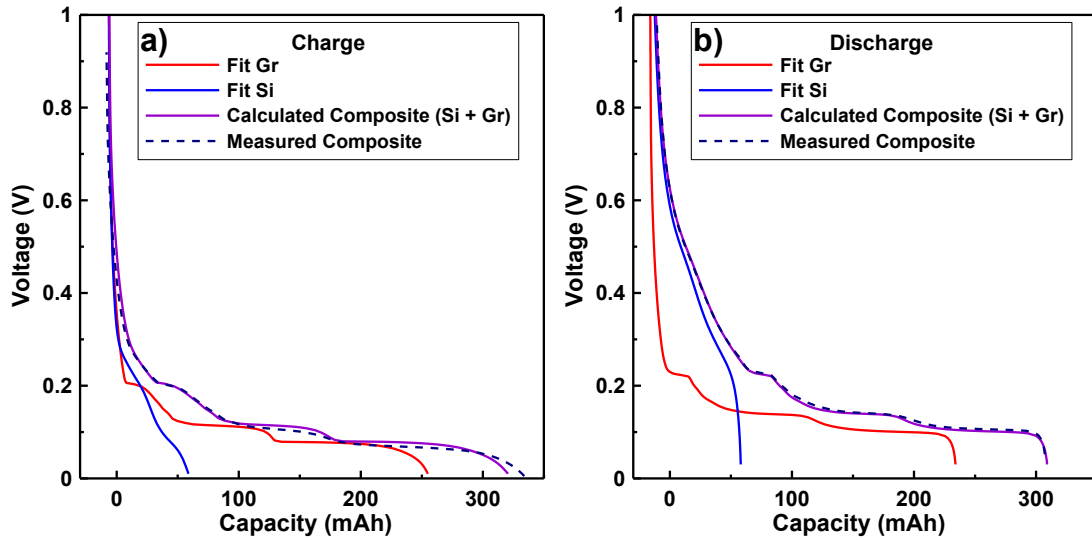


Figure 4.8: The dV/dQ fits during charge a) and discharge b) of the SiO-graphite composite negative electrode. The graphite component (red) is added to the SiO component (blue) to make the calculated composite in solid magenta, which is a fit of the experimental data shown in dotted purple.

This calculation is done for both components during charge and discharge as shown in Figure 4.9c and d respectively. The charge and discharge dQ/dV vs. V for each component is plotted in the panels above (Figures 4.9a and b) to help elucidate the state of charge vs. capacity behaviour. For example, one can see by considering the relative area of the SiO and graphite dQ/dV curves that the SiO component reaches a higher SOC faster than graphite during charge, whereas graphite reaches a lower SOC faster than SiO during discharge. This behaviour is reflected in the SOC vs. composite capacity curves shown in

Figures 4.9c and d. Additionally, the dQ/dV vs. V curve of graphite shows little charge/discharge hysteresis, also reflected in the SOC of the graphite component vs. the composite electrode capacity curves. Silicon shows a large hysteresis in dQ/dV vs. V , and as such the SiO component SOC vs. composite electrode capacity profile is significantly different between charge and discharge. The dQ/dV vs. V curves of graphite and silicon overlap during charge meaning that both components are lithiated simultaneously. Due to the hysteresis of silicon, there is much less overlap of the dQ/dV vs. V curves during discharge; almost all of the capacity of graphite is delivered before silicon begins to de-lithiate. This is reflected in the component SOC vs. composite electrode capacity plot in Figure 4.9d that shows that graphite is de-lithiated to 10% SOC before any significant capacity from silicon has been delivered.

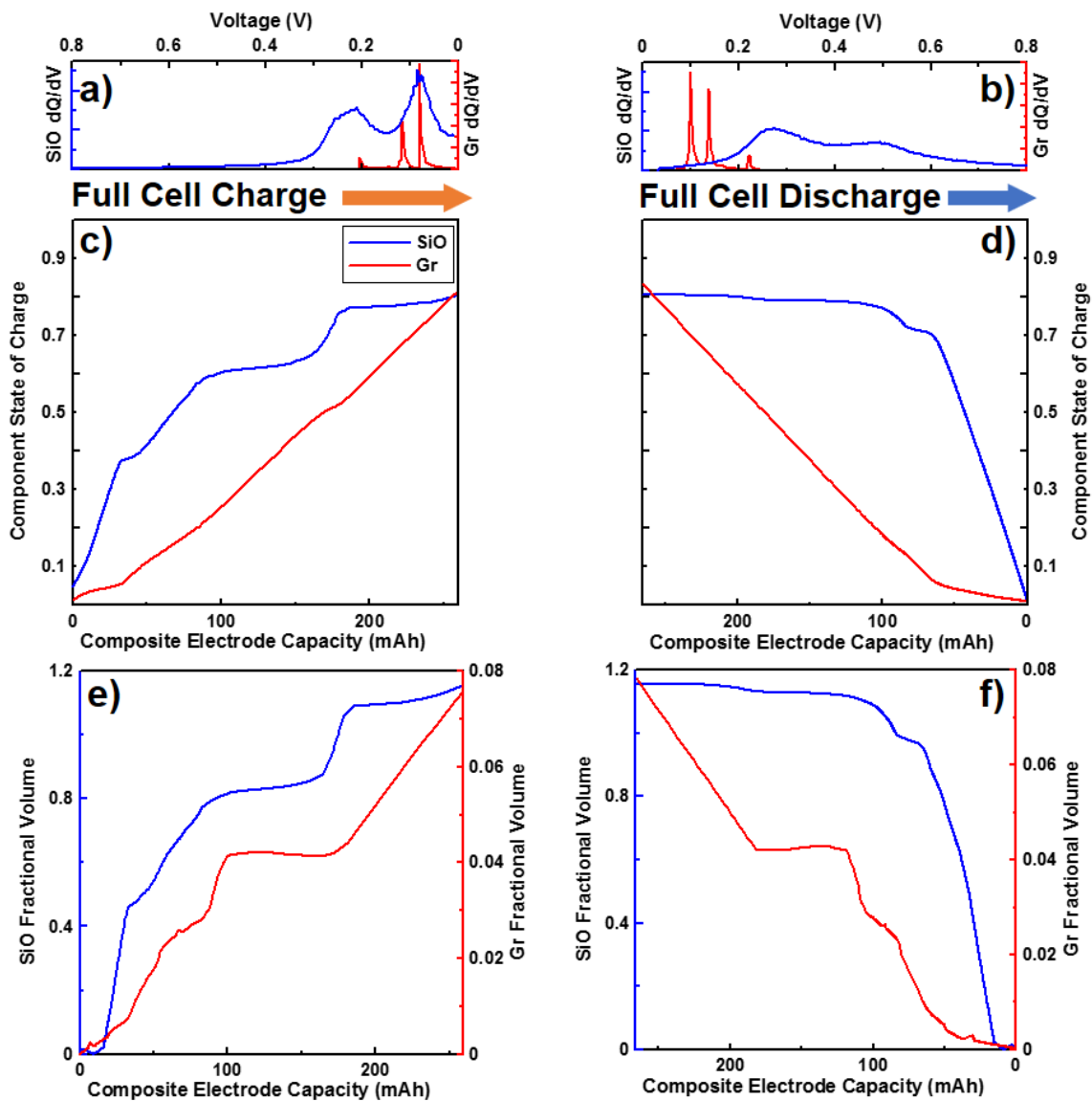


Figure 4.9: dQ/dV vs. V (a,b), component state of charge (c,d) and fractional volume expansion (e,f) vs. composite electrode capacity of graphite (red) and SiO (blue) during the full cell charge (left column) and discharge (right column).

The fractional volume vs. state of charge data for each component previously presented in Figures 4.7a and b can now be combined with the state of charge vs. composite electrode capacity data presented in Figures 4.9c and d to plot the fractional volume vs. composite negative electrode capacity for each component, as done in Figures 4.9e and f.

This shows how the volume of each component varies during charge and discharge within the composite negative electrode. The volume expansion profile of graphite is dominated by the fractional volume vs. SOC behaviour shown in Figure 4.7a since the SOC of graphite vs. composite electrode capacity is fairly linear during charge and discharge, shown in Figure 4.9c and d. Conversely, the volume expansion profile of SiO is dominated by the SOC of SiO vs. composite electrode capacity behavior shown in Figures 4.9c and d, since the fractional volume vs. SOC of SiO is fairly linear shown in Figure 4.7b.

4.3.3 Predicted Type C Full Cell Expansion

In Figures 4.6, 4.9e, and f, the fractional volume expansion of the positive electrode and both components of the negative electrode as a function of capacity is shown. Using the initial masses of each component derived from dV/dQ fitting, the initial volumes of each component can be calculated from their respective densities. In SiO, a-Si is the active component which is being reversibly lithiated and de-lithiated during charge/discharge cycling post-formation. Therefore, it is the a-Si mass and density that is used to determine the initial volume of the silicon component. Multiplying the initial volumes by the fractional volume changes of each component results in the volume of each component during charge and discharge. This is done in Figure 4.10a. The change in volume of the positive electrode is shown in red. Each component of the negative electrode—graphite and SiO, are shown in light and dark teal, respectively. Their sum contribution, resulting in the composite negative electrode volume expansion, is shown in blue. This is added to the change in positive volume to calculate the full cell change in volume shown in lime green. To compare this calculation with experimental results, the measured volume, pressure and thickness data for Type C cells are overlaid in Figure 4.10b.

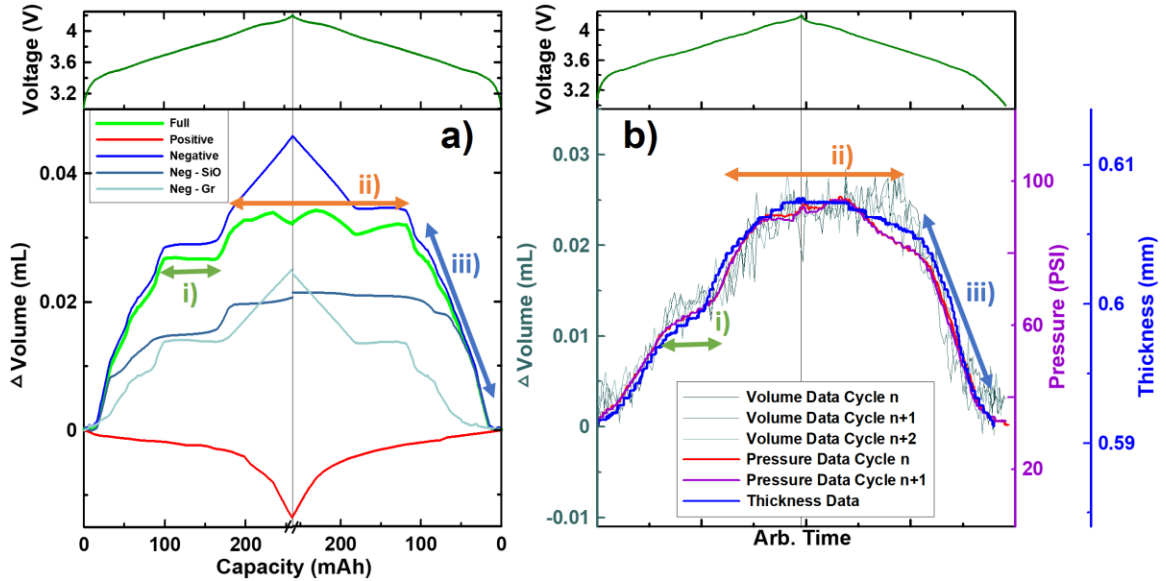


Figure 4.10: a) The calculated change of volume for each electrode component during charge and discharge. b) The measured volume, pressure and thickness data for Type C cells to compare to the calculated volume expansion profile. A plateau during charge, an asymmetric plateau near the top of charge, and a rapid fall seen in both a) and b) are highlighted as features i), ii) and iii) respectively.

The calculations made in Figure 4.10a show good qualitative agreement with the experimental results shown in Figure 4.10b. Specifically, three key features: i) a plateau during charge; ii) an asymmetric plateau near the top of charge; and iii) a rapid volume contraction seen in both calculated and experimental profiles are highlighted in both figures. From the calculations made here, an understanding of these features and the overall asymmetric measured volume expansion profile can be obtained. Feature i) is a plateau in volume expansion due to the stage $2L \rightarrow 2$ phase transition of graphite as previously discussed. Throughout this transition, graphite does not expand in volume, slowing the overall volume expansion of the cell. Feature ii) is a result of two mechanisms: (a) The first two thirds of the plateau is caused by rapid NCA contraction and expansion at the end of charge and then the beginning of discharge, respectively, that effectively cancels

out the opposing expansion and contraction of the negative electrode over this region; (b) The final third of the plateau in feature ii) is caused by the graphite $2 \rightarrow 2L$ transformation, over which graphite does not contract. This contributes to the volume plateau instead of showing up as a distinct feature like i) due to SiO charge/discharge hysteresis. Throughout this transformation during discharge, SiO has yet to begin de-lithiating, therefore it is still at its largest volume, causing this graphite feature to appear higher and distinct from the volume plateau during discharge. Feature iii) is caused by the de-lithiation of the Si in SiO, resulting in a rapid overall volume contraction. In addition to these qualitative agreements, the magnitude of the volume change calculated in Figure 4.10a (~ 0.03 mL) is in decent agreement with the measured expansion in Figure 4.10b of ~ 0.025 mL.

4.3.4 Understanding the Expansion of Other Silicon-Containing Cells

The detailed analysis of Type C cells can be used to elucidate the volume expansion behavior of the other silicon-containing cells presented in this work—Type B LCO/Si alloy-graphite and Type D NCA/nano Si-C cells. The volume and pressure profiles of Type D-i and D-ii cells shown in Figure 4.2d and e and 4.2f and g respectively are similar to that of Type C cells.[§] Each of the 3 features highlighted in the calculated volume profile in Figure 4.10 can be seen in Type D cells. Therefore, the same mechanisms discussed in Section 4.3.3 for Type C cells to apply to Type D cells. Although the Type B cell

[§] The pressure vs. time profiles of Type D cells are more horizontally compressed than pressure profile of the Type C cell shown in Figure 4.2. This may be explained by the larger compliancy Type D cells exhibit compared to Type C cells, as shown in the appendix in Figure A.1. Since Type D cells are more compliant, a larger volume change is required to produce the same pressure signal. However, the compliancy would have no effect on the volume measurements, and indeed the volume profiles of Type C and D cells are very similar.

measurements shown in Figure 4.1e and 3f exhibit features i) and iii) clearly, there is an apparent difference in that feature ii), the plateau near the top of charge, is not observed. This is because LCO is used as the positive electrode instead of NCA as in Type C and D cells. Whereas NCA exhibits a volume contraction during full cell charge in the voltage range tested, LCO expands in this voltage range, seen in the data adapted from Ref.⁴⁴ by Reimers and Dahn shown in Figure 4.11. Although this is a small ~1% expansion, it was the contraction of NCA, specifically the rapid contraction near the TOC, that effectively cancelled out the expansion of the negative electrode components, resulting in an overall volume plateau. Considering the small expansion of LCO to be negligible, the calculations of Figure 4.10a for the composite negative electrode shown in blue would be comparable to cell Type B measurements where, to a first approximation, only the negative electrode components contribute to the net volume expansion of the cell. This shows a good qualitative agreement with the measured volume and pressure profiles for Type B cells shown in Figure 4.1e and f. This analysis is in good agreement with the electrochemical dilatometry profile of a LiCoO₂/nano Si-graphite cell and a Si-graphite half-cell observed in Figure 4 of Ref.¹⁸ and Figure 8 of Ref.⁴¹, respectively. The feature ii) plateau is not observed in Ref.¹⁸ due to the use of LCO as the positive electrode, just as in cell Type B, nor is it seen in Ref.⁴¹ since the cell measured there has no positive electrode. The feature iii) separation between graphite and silicon contraction during discharge is clearly seen in Refs.¹⁸ and ⁴¹, as well as a subtle change in slope during charge characteristic of feature i).

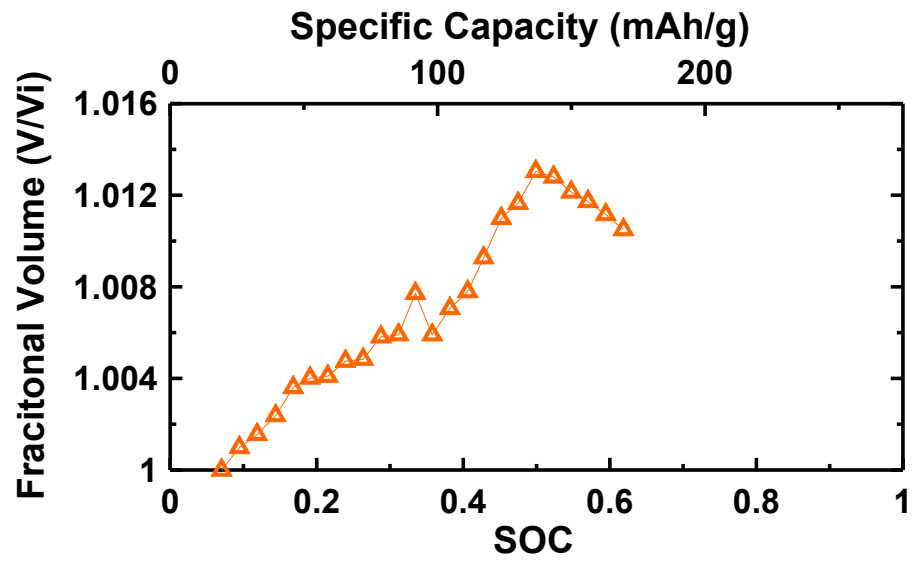


Figure 4.11: Fractional volume expansion of LCO adapted from Reimers and Dahn.⁴⁴

Chapter 5: Pressure Evolution & Degradation Analysis

This work introduced a method for *in-situ* pressure measurements of volumetrically constrained Li-ion pouch cells. It was demonstrated in Chapter 4 that this technique can be used to probe the reversible volume change of Li-ion cells caused by electrode expansion and contraction during cycling over the course of a few cycles. The *in-situ* pressure measurements introduced in this work are also capable of monitoring the volume evolution of cells charged and discharged over many cycles. The volume expansion and contraction of Li-ion cells has been measured by electrochemical dilatometry,^{23,39-41} but that technique is not suited for long term measurements.⁴¹ To the author's knowledge, this work reports the first such measurements of long-term Li-ion cell volume evolution. This chapter demonstrates that when the pressure evolution of a pouch cell is monitored over many cycles, an irreversible pressure growth is measured. Preliminary results using this technique, presented here, indicate that there is a correlation between larger pressure growth and worse capacity retention. Therefore, it is proposed that *in-situ* pressure measurements may be a useful technique for ranking the performance of Li-ion cells.

Cells used in electric vehicles require a lifetime of about a thousand charge/discharge cycles, and the lifetime requirement for grid energy storage applications is many thousands of cycles over tens of years. Therefore, developing better cell chemistries to meet these requirements necessitates the ability to predict the long-term lifetime. Verifying that a new Li-ion chemistry will last a decade by testing that battery for a decade is impractical. Therefore, short-term methods (over the course of weeks) to rank the lifetime of Li-ion batteries are vital to academic and industrial research. Techniques such as ultra high

precision coulometry and electrochemical calorimetry are examples of short-term characterization techniques used to rank the performance of Li-ion cells, but these techniques require costly high precision equipment.^{47,48} By contrast, the equipment required for *in-situ* pressure measurements presented here can be obtained for a fraction of the cost. Additionally, Burns et al. showed that conventional short-term cycling tests, i.e. cycling for a few weeks and using the short-term capacity retention data to rank cells, is not always predictive of long-term performance.⁴⁹ This further motivates the necessity of predictive short-term characterization techniques. Therefore, the addition of *in-situ* pressure measurements to the toolbox of a Li-ion cell researcher may prove to be valuable. This chapter investigates the pressure evolution of all the cell chemistries introduced in this work, starting first with cells containing single-component graphite negative electrodes, and then cells with silicon-composite negative electrodes. A study of the pressure evolution of cells with the same electrode chemistry that use a different electrolyte is also presented for the graphite cells. Then, differential voltage analysis is performed to try to elucidate the mechanisms for capacity loss and correlate them with the measured pressure growth.

5.1 Analysis of Cells with Graphite Negative Electrodes

Pressure evolution studies were performed on Type A-i (NMC/AG) and A-ii (NMC/NG) cells with 0.25PES211 and 1.0PES211 electrolytes. The motivation for this work was to elucidate the superior performance of cells with artificial graphite negative electrodes (Type A-i) compared to cells with natural graphite negative electrodes (Type A-ii).⁵⁰ It is hypothesized that natural graphite is exfoliated during lithiation due to the high degree of

crystallinity of the graphite structure. Exfoliation would increase the surface area of the negative electrode, promoting more lithium-consuming parasitic reactions forming SEI, thereby negatively affecting the capacity retention of NG cells. Additionally, previous studies have shown that 1.0PES211 electrolyte forms a more robust SEI than 0.25PES211 electrolyte in Type A-i and A-ii cells.^{50,51} Therefore, any SEI disruption causing SEI growth and repair would be worse in cells using 0.25PES211 due to a weaker SEI. More SEI growth as well as graphite exfoliation are hypothesized to cause a macro-scale volume expansion in pouch cells, which can be probed with *in-situ* pressure measurements. As such, *in-situ* pressure measurements were performed to attempt to identify these effects.

Since there are two variables being studied here—AG vs. NG negative electrodes and 0.25 vs. 1.0PES211 electrolyte, the data will be presented in two ways. First, a comparison between cells with different electrodes, i.e. AG Type A-i vs. NG Type A-ii cells with 1.0 and then 0.25PES211 electrolyte. Then, a comparison between electrolytes: 1.0 vs. 0.25PES211 for AG Type A-i cells and then NG Type A-ii cells. For conciseness, Type A-i cells will be referred to as simply “AG cells” and Type A-ii cells will be referred to as “NG cells” for the remainder of this section.

5.1.1 Electrode Comparison: AG vs. NG

AG vs. NG with 1.0PES211

The bottom panel of Figure 5.1a shows an example of pressure evolution data, here for AG and NG cells with 1.0PES211 electrolyte. The top panel of this figure shows the corresponding voltage vs. time profile for the NG cell; the AG cell voltage vs. time is omitted for clarity. It is clear that the pressure increases during charge and decreases during

discharge due to the volume expansion and contraction of the electrode materials, as demonstrated in Chapter 4. As such, the voltage profiles will be left out of future figures. The cells shown in Figure 5.1a were cycled at C/6 for about 900 hours and subsequently cycled at C/3 until the end of testing. The pressure growth over time is clearly more severe for the NG cell. However, such a clear trend cannot always be seen using raw pressure vs. time plots as presented in Figure 5.1a, especially when trying to compare more than two cells. Overlaying these data can make it hard to distinguish where one curve begins and another ends, therefore, it is important to extract meaningful metrics out of the raw pressure vs. time curves for analysis. Such metrics to consider are presented in Figure 5.1b. The pressure at the top of charge (TOC) and bottom of charge (BOC) can be tracked, shown circled in Figure 5.1b. The pressure swing (pressure at TOC – pressure at BOC) can be calculated. The area under the pressure curve for one cycle, divided by the duration of the cycle, i.e. the average pressure, can also be calculated. The electrochemical data for these cells, namely the capacity retention, is also important to track to make correlations between the performance of the cells and the pressure data. All of these quantities can be plotted vs. cycle number or time. This is an important distinction for comparing cells that have been cycled at different currents, i.e. in Figure 5.1a wherein cells were cycled at C/6 for 900 hours and then at C/3. For this work, all of the pressure vs. time raw data is processed to calculate the different metrics described here using a MATLAB script.

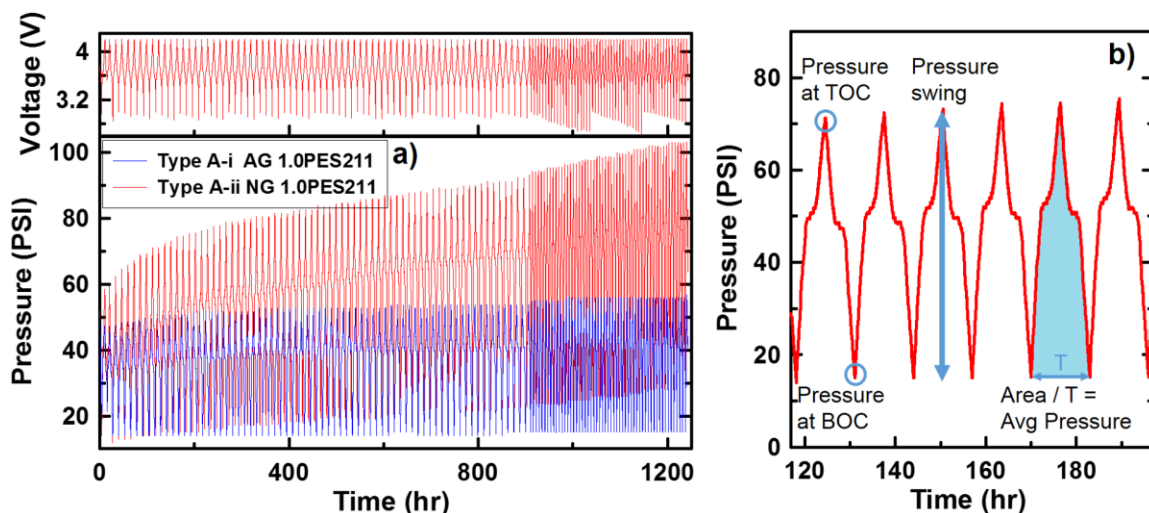


Figure 5.1: a) The pressure vs. time profiles of 1.0PES211 AG (blue) and NG cells (red). The corresponding voltage vs. time graph of the NG cell is shown in the top panel. The cells were cycled between 3.0 V and 4.2 V at 40°C. b) Proposed metrics for measuring pressure evolution: the pressure at the top of charge (TOC), the pressure at the bottom of charge (BOC), the pressure swing, and the average pressure.

Figure 5.2 shows the normalized capacity of AG and NG cells with 1.0PES211 electrolyte vs. cycle no. (a) and time (b). AG cells are shown with triangles in different shades of blue representing different trials, and NG cells are shown with circles in shades of red representing different trials. Cells NG v3 and AG v3 were cycled at C/6 for around 70 cycles (~900 hours) and were then switched to C/3 cycling, causing a capacity drop. Cell NG v4 was cycled at C/3 from the beginning of cycling, therefore, for clarity, its initial normalized capacity was shifted down from 1.0 to match the capacities of the other cells which were switched to C/3 cycling. All other cells were cycled at C/6. Figure 5.2 shows that NG cells have a worse capacity retention than AG cells. Parallel lines in dark orange are drawn for a comparison of the rate of capacity loss. In Figure 5.2a, the dark orange lines match the rate loss of the NG C/6 cycles, but not the C/3 cycles. In Figure 5.2b, the lines match the rate loss of the NG C/6 cycles, but not the C/3 cycles. In Figure 5.2b, the lines match the rate of capacity loss in NG cells for both C-rates. This indicates that the

mechanism for capacity loss for these cells is time dependent, not cycle dependent. Therefore, the metrics for pressure growth will be plotted vs. time.

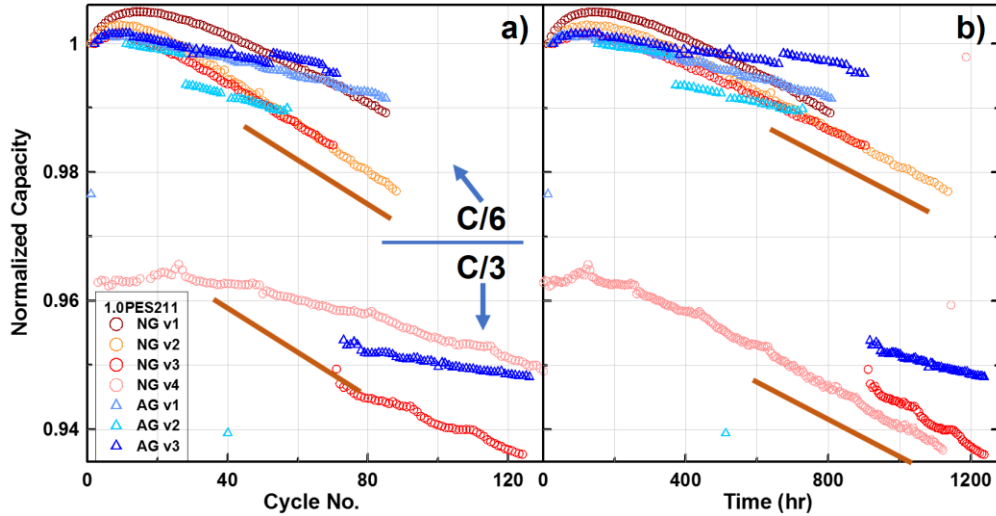


Figure 5.2: The normalized capacity of 1.0PES211 AG (blue triangles) and NG (red circles) cells plotted vs. cycle no. (a) and time (b). All cells were cycled between 3.0 V and 4.2 V at 40°C.

Figure 5.3 shows the calculated metrics for quantifying the pressure growth of AG and NG cells with 1.0PES211 electrolyte. The four rows of plots show the four metrics: pressure at BOC (a,b), pressure at TOC (c,d), pressure swing (e,f) and average pressure (g,h). The first column shows these calculated metrics, and the second column shows the change (delta) in these metrics. All subsequent figures of pressure metrics will be plotted in this way. Figure 5.3 shows that NG cells (red circles) experience a more severe growth than AG cells (blue triangles), as was demonstrated with the raw data presented in Figure 5.1a. Figure 5.2 previously showed that NG cells experienced worse capacity retention than AG cells. This apparent correlation between larger pressure growth and poorer capacity performance suggests that pressure growth can be used to rank the performance of cells.

The larger pressure growth NG cells experience is consistent with the hypothesis of graphite exfoliation causing more SEI production, thereby increasing the rate of capacity loss.

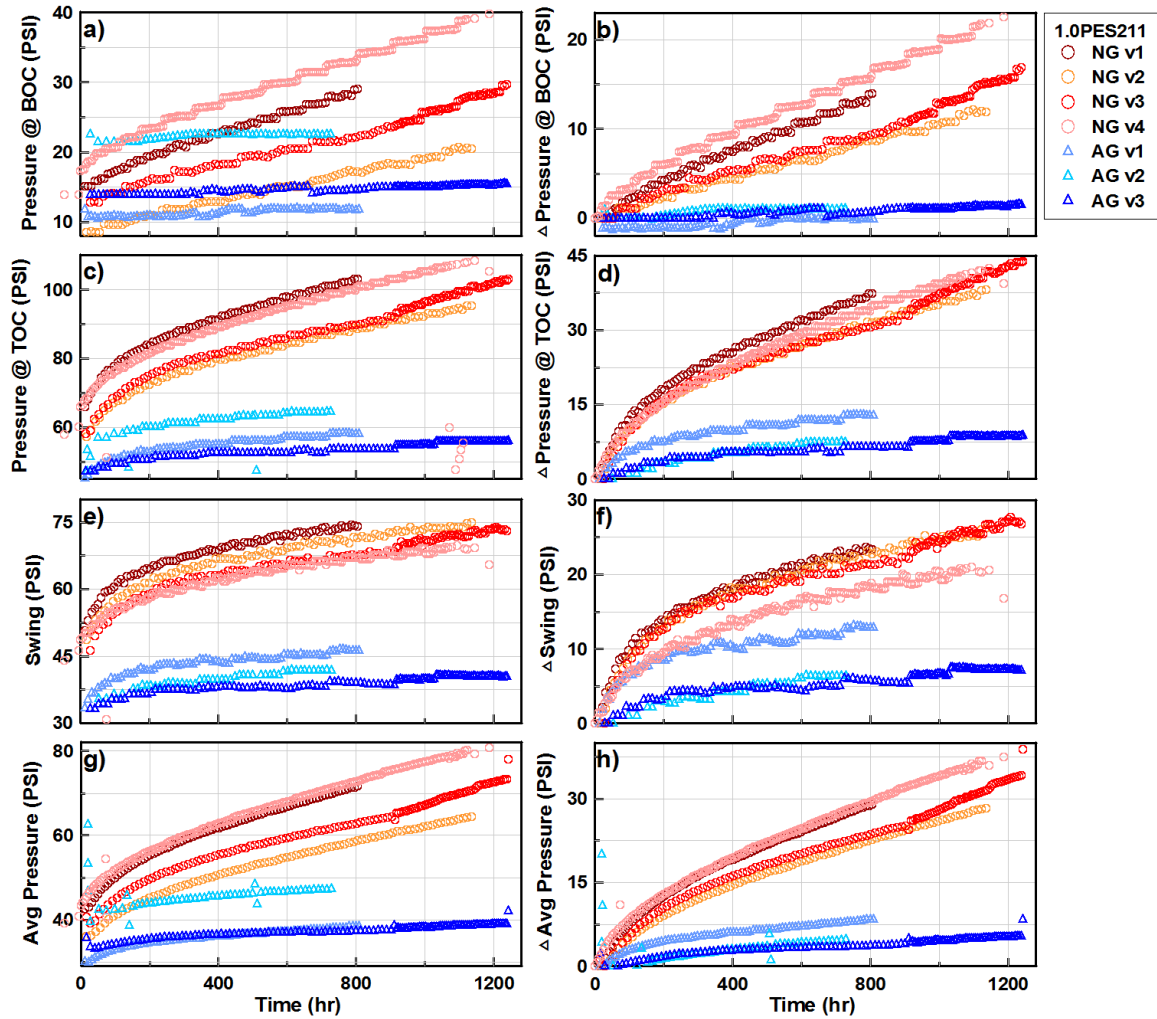


Figure 5.3: Metrics of pressure evolution for 1.0PES211 AG (blue triangles) and NG cells (red circles). Each row shows the metric (left) and the change in the metric (right): a,b) the pressure at the bottom of charge; c,d) the pressure at the top of charge; e,f) the pressure swing; g,h) the average pressure. The capacity vs. time data for these cells is given in Figure 5.2.

AG vs. NG with 0.25PES211

Figure 5.4 shows the normalized capacity of AG (blue triangles) and NG cells (red circles) with 0.25PES211 electrolyte vs. cycle no. (a) and time (b). All cells were cycled at C/6, except for NG v5 which was cycled at C/3. Again, the AG cells show superior performance compared to the NG cells. The agreement between trials of NG capacity vs. time data plotted in Figure 5.4b is not as good as was previously seen with the 1.0PES211 cells in Figure 5.2. The targeted currents for NG v1-v4 was a C/6 rate, however, a slightly larger current was used for NG v1 and v2 compared to NG v3 and v4. NG v5 was cycled at an even larger current to achieve a rate of C/3. The disagreement between capacity vs. time data between 0.25PES211 NG cells cycled at different currents suggests there is also a cycle dependence to capacity loss for these cells.

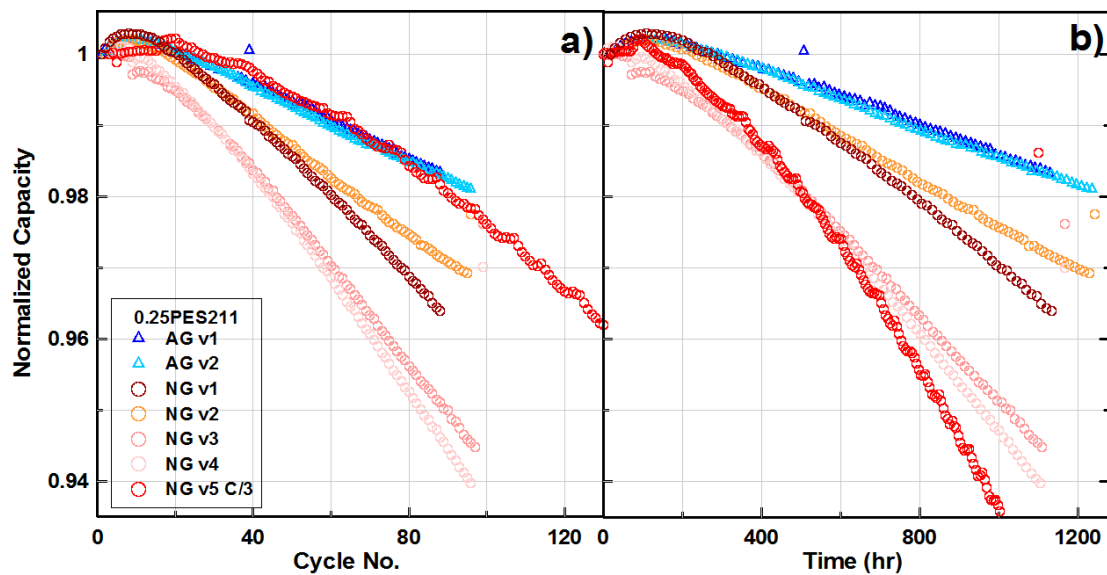


Figure 5.4: The normalized capacity of 0.25PES211 AG (blue triangles) and NG cells (red circles) plotted vs. cycle no. (a) and time (b). All cells were cycled at C/6, unless labeled otherwise, between 3.0 V and 4.2 V at 40°C.

Figure 5.5 shows the metrics for pressure evolution of AG (blue triangles) and NG cells (red circles) with 0.25PES211 electrolyte. By and large, this figure tells the same story as

the pressure evolution experienced in 1.0PES211 cells: NG cells experience a larger pressure growth, which is consistent with the hypothesis for their inferior performance. However, this data shows more variance between the NG trials, and, as a result, some trials such as NG v1 show a pressure growth rate similar to AG cells. A possible source of this variation between pressure growth data will be discussed later in this section.

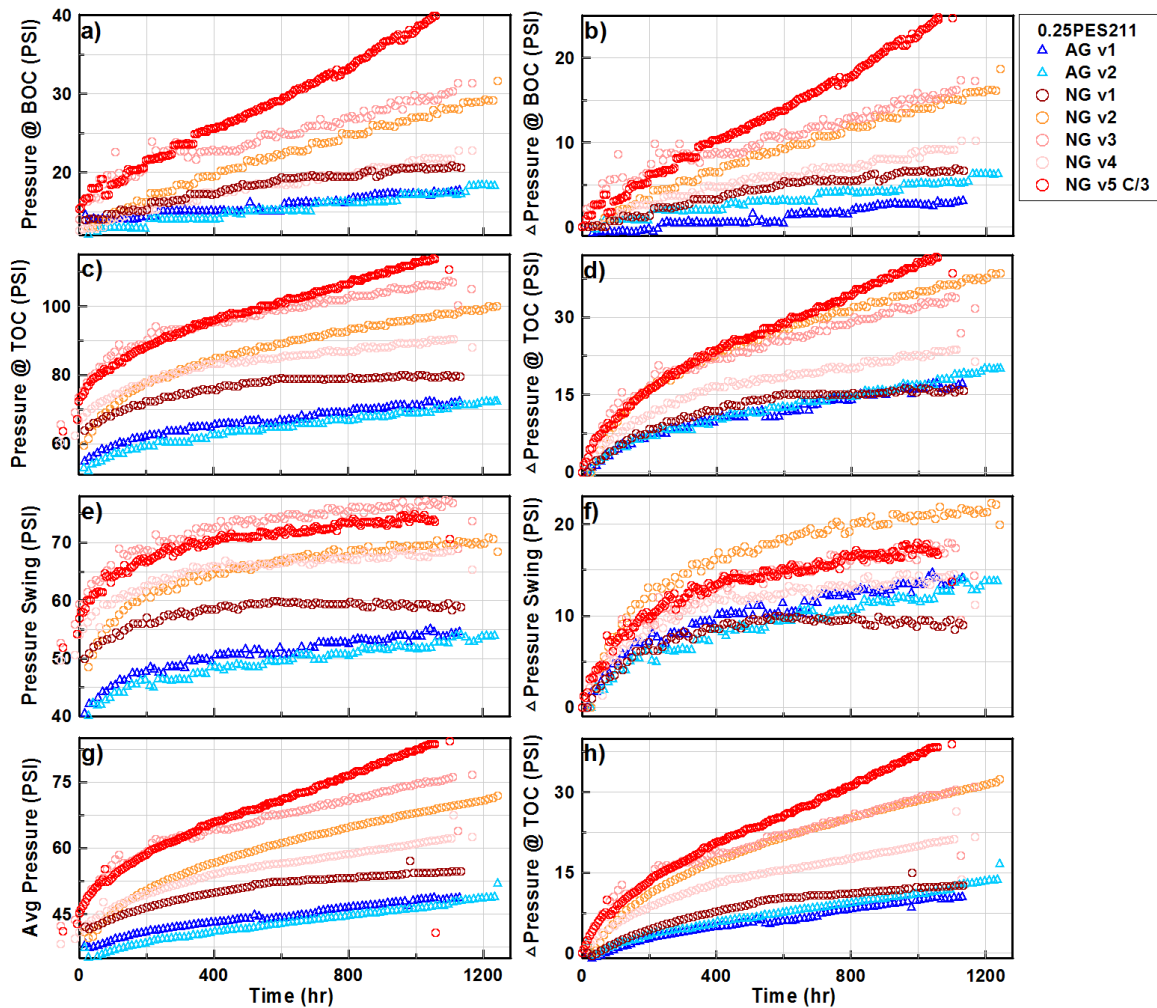


Figure 5.5: Metrics of pressure evolution for 0.25PES211 AG (blue triangles) and NG cells (red circles). Each row shows the metric (left) and the change in the metric (right): a,b) the pressure at the bottom of charge; c,d) the pressure at the top of charge; e,f) the pressure swing; g,h) the average pressure. The capacity vs. time data for these cells is given in Figure 5.4.

The data presented in this sub section showed that *in-situ* pressure measurements accurately ranked the capacity retention of cells with AG vs. NG electrode chemistries using 1.0PES211 electrolyte. This data is consistent with the hypothesis that the pressure growth and capacity loss these cells exhibit is caused by SEI growth.

5.1.2 Electrolyte Comparison: 0.25PES211 vs. 1.0PES211

0.25PES211 vs. 1.0PES211 AG

Figure 5.6 compares the normalized capacity vs. cycle no. (a) and time (b) of AG cells with 0.25PES211 (red circles) and 1.0PES211 electrolyte (blue triangles). The rate of capacity loss is greater for cells with 0.25PES211. This is consistent with the hypothesis that 0.25PES211 electrolyte forms a weaker SEI which is more prone to damage and thus growth and repair, consuming more lithium inventory. The corresponding pressure evolution metrics are presented in Figure 5.7.

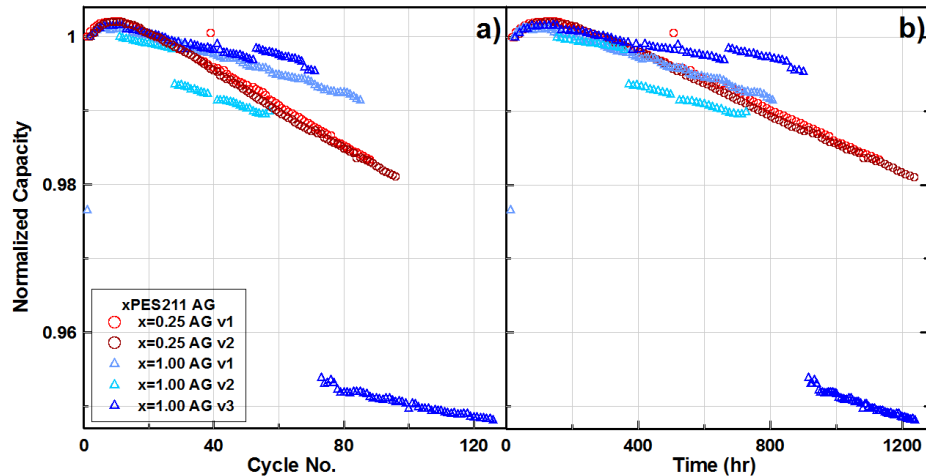


Figure 5.6: The normalized capacity of AG 0.25PES211 (blue triangles) and 1.0PES211 cells (red circles) plotted vs. cycle no. (a) and time (b). All cells were between 3.0 V and 4.2 V at 40°C. The C-rate of cell x=1.00 AG v3 was changed mid-experiment resulting in a capacity drop around cycle 70.

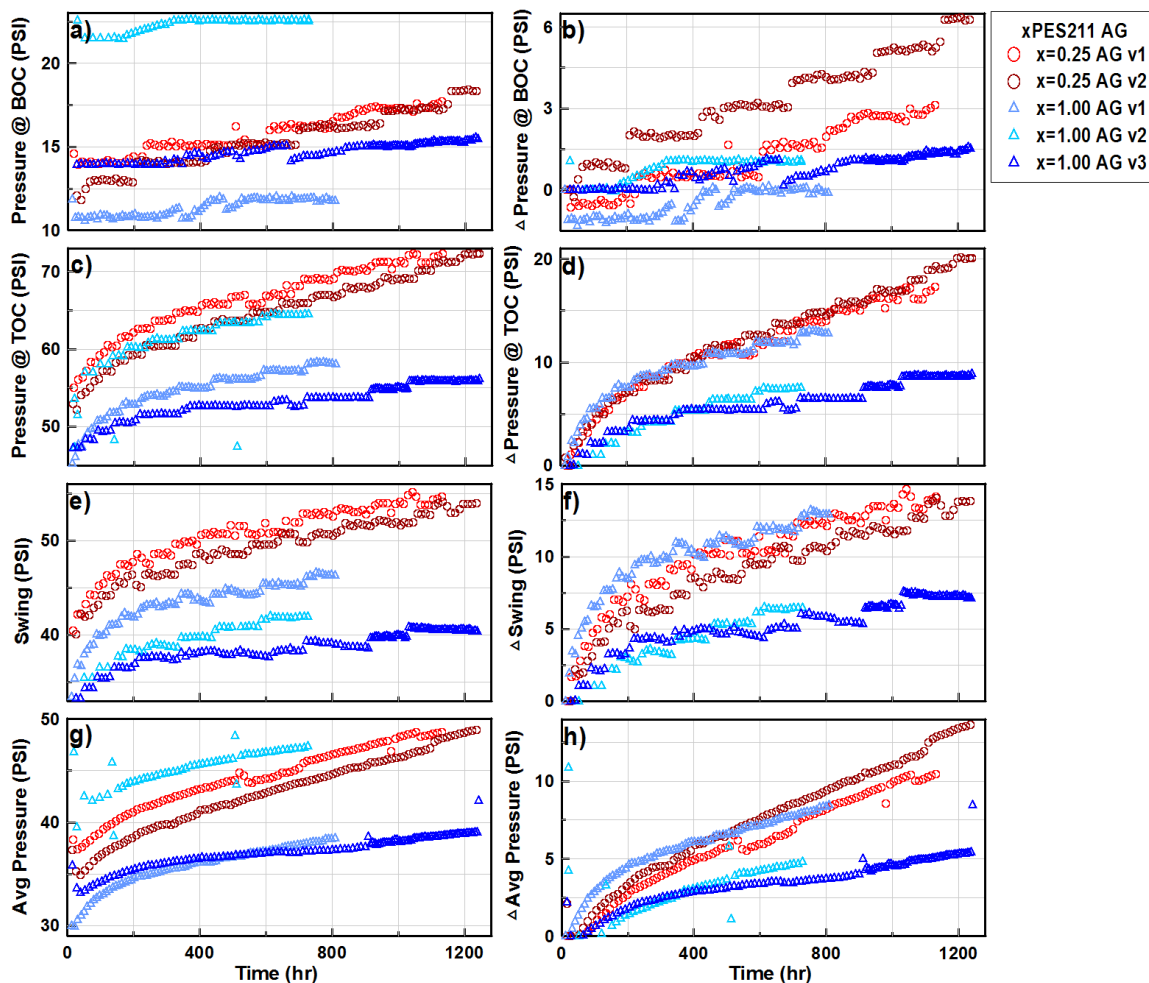


Figure 5.7: Metrics of pressure evolution for AG 1.0PES211 (blue triangles) and 0.25PES211 cells (red circles). Each row shows the metric (left) and the change in the metric (right): a,b) the pressure at the bottom of charge; c,d) the pressure at the top of charge; e,f) the pressure swing; g,h) the average pressure. The capacity vs. time data for these cells is given in Figure 5.6.

Most of this data shows that 0.25PES211 AG cells experience a larger pressure growth than 1.0PES211 cells, corresponding to their worse capacity retention. Cell x=1.00 AG v1 showed a similar initial pressure growth to the 0.25PES211 cells, but by the end of testing the rate of growth is comparable to the 1.0PES211 cells.

0.25 vs. 1.0PES211 NG

Figure 5.8 shows the normalized capacity of NG cells with 0.25 (red circles) and 1.0PES211 electrolyte (blue triangles), plotted vs. cycle no. (a) and time (b). As shown previously, the rate of capacity loss for 1.0PES211 NG cells is strictly time dependent, resulting in good agreement between capacity data when plotted vs. time. The 0.25PES211 NG cells, however, also have a cycle dependence, resulting in differing capacity loss rates when plotted vs. time. Most of the 0.25 NG cells show worse capacity retention than 1.0PES211 NG cells. The corresponding pressure evolution data is presented in Figure 5.9.

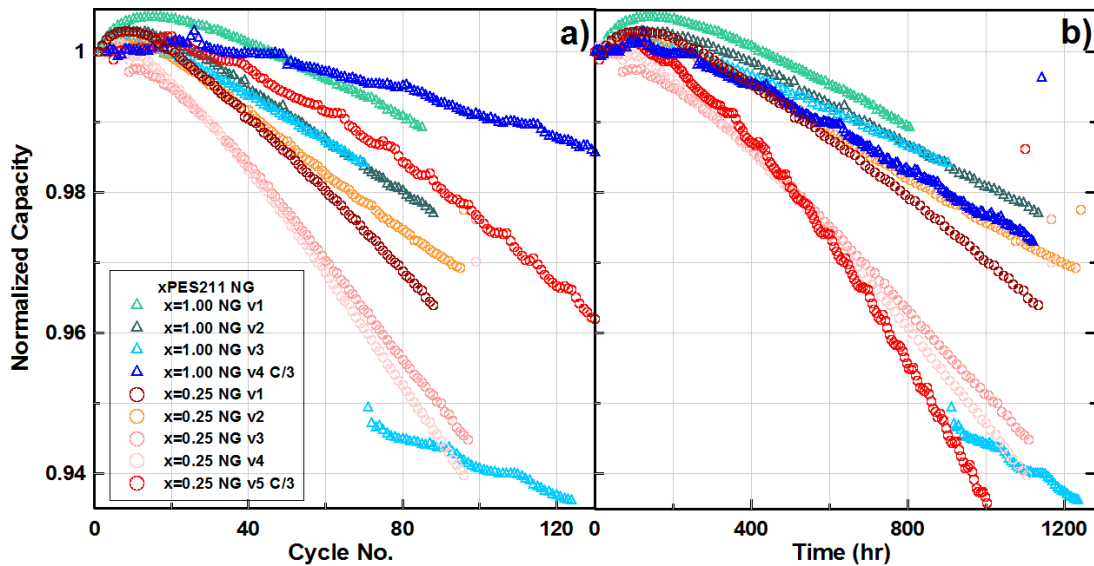


Figure 5.8: The normalized capacity of NG 1.0PES211 (blue triangles) and 0.25PES211 cells (red circles) plotted vs. cycle no. (a) and time (b). All cells were cycled between 3.0 V and 4.2 V at 40°C.

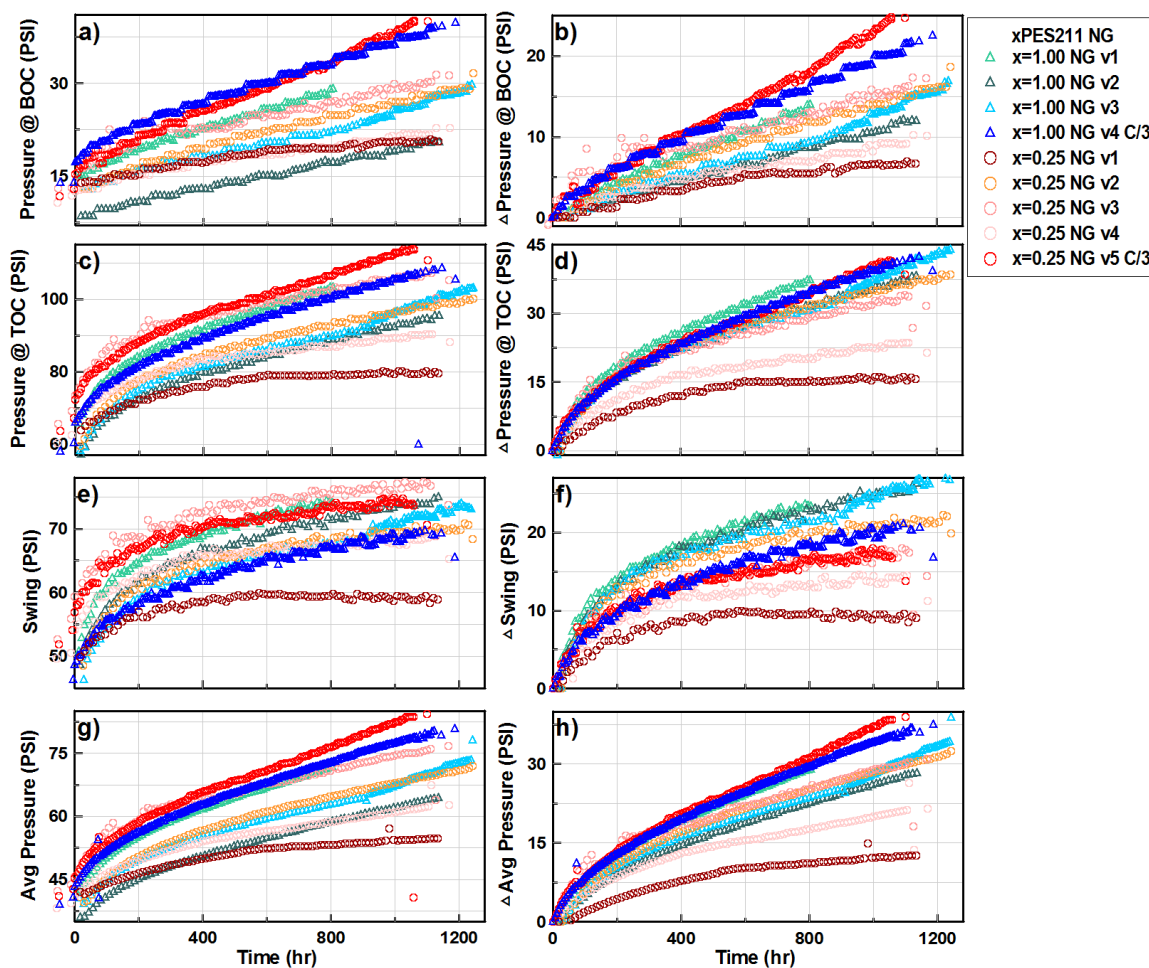


Figure 5.9: Metrics of pressure evolution for NG 1.0PES211 (blue triangles) and 0.25PES211 cells (red circles). Each row shows the metric (left) and the change in the metric (right): a,b) the pressure at the bottom of charge; c,d) the pressure at the top of charge; e,f) the pressure swing; g,h) the average pressure. The capacity vs. time data for these cells is given in Figure 5.8.

The pressure evolution data for 0.25 vs. 1.0PES211 NG cells presented in Figure 5.9 does not illustrate a clear picture. The 0.25PES211 NG cells, which generally exhibit poorer performance, do not clearly show a larger pressure growth than 1.0PES211 NG cells, as would be expected if there was more SEI growth. The large variation between 0.25 NG trials makes the data difficult to interpret. Figure 5.9 shows that 0.25 NG cells experience

the same pressure growth as 1.0 NG cells in some trials, and a lower pressure growth in other trials.

The data presented in this sub section showed that *in-situ* pressure measurements accurately ranked cell performance between different electrolyte chemistries for AG cells but not for NG cells. A large variation in pressure growth was observed between 0.25PES211 NG cells. One possible explanation for this is the method of initializing the pressure tests. As discussed in the experimental methods section, cells are secured into superboats by hand-tightening four screws to force the adjustable superboat wall against the pouch cell. However, hand-tightening may not result in a uniform pressure across one pouch cell, nor is it conducive for cell-to-cell pressure control. This may result in cell-to-cell variation in pressure growth. Future work is necessary to definitively determine if *in-situ* pressure measurements are capable of predicting the performance between cells with different electrolyte blends.

To clearly show all the capacity vs. pressure growth correlations discussed in Sections 5.1.1 and 5.1.2, Figure 5.10 shows a summary of all the data presented in these sections. AG data are shown in shades of blue and NG data are shown in shades of red; $x=1.00$ electrolyte data are shown in circles and $x=0.25$ data are shown in triangles. Figure 5.10a shows the percentage capacity lost vs. the change in average pressure for each cell at the end testing. To make informed judgements about cell performance, especially during short-term cycling, often the rate of capacity loss by the end of testing is more important than the absolute loss. Therefore, Figure 5.10b shows the rate of capacity loss per hour at the end of testing vs. the rate of change in average pressure per hour at the end of testing. These

rates were determined by performing a linear regression on the final 100 hours of the capacity vs. time and change in average pressure vs. time curves.

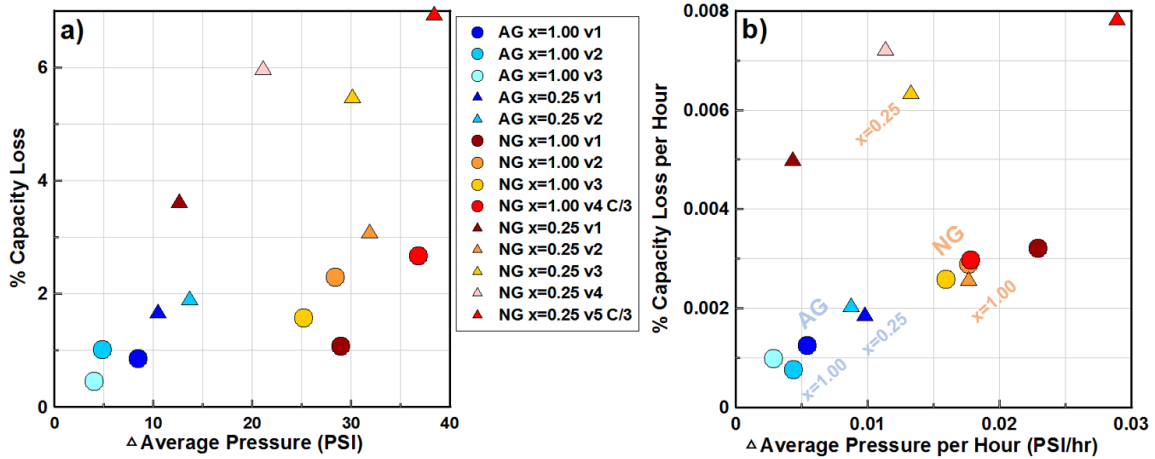


Figure 5.10: Summary of capacity loss vs. pressure growth data for AG and NG cells. a) Percent capacity loss vs. change in average pressure at the end of testing. b) Rate of capacity loss vs. rate of change in average pressure measured during the last 100 hours of testing. AG data are shown in shades of blue, NG data are shown in shades of red; 1.0PES211 electrolyte data are shown with circles, 0.25PES211 electrolyte data are shown with triangles. Cells were cycled at C/6 unless labeled otherwise, and were cycled between 3.0 V and 4.2 V at 40°C.

Figure 5.10a shows a trend between capacity loss and average pressure growth for most data points in addition to some outliers. Figure 5.10b shows this trend more clearly with the rates of capacity loss and pressure growth. AG cells show the best capacity retention and the least pressure growth, with 0.25PES211 AG cells performing slightly worse with larger pressure growth. This is consistent with the hypothesis that 0.25PES211 electrolyte forms a weaker SEI more prone to damage and growth. 1.0PES211 NG cells perform worse than AG cells and exhibit a larger pressure growth, consistent with the hypothesis that natural graphite electrodes exfoliate resulting in more SEI growth. 0.25PES211 NG cells exhibit poorer performance, but do not show the requisite additional growth in

pressure, and are thus outliers in the capacity loss vs. pressure growth trend. In summary, *in-situ* pressure measurements accurately ranked all the chemistries presented in this section, and the hypothesis that SEI growth was the cause of poor capacity retention was consistent in all cases, except for the 0.25PES211 NG chemistry. To investigate this disconnect between capacity loss, pressure growth, and the SEI growth hypothesis, the following section presents differential voltage analysis to quantify the SEI growth of these cells.

5.1.3 Differential Voltage Analysis

To investigate the claim that higher rates of pressure growth are caused by increased SEI production, differential voltage analysis was performed on natural graphite cells that exhibited large pressure growth to determine the mechanisms for capacity loss. This analysis was performed on 0.25PES211 cells labeled NG v2, v3, v4, and v5 C/3, as well as 1.0PES211 cells labeled NG v3 and NG v4 C/3. Cells that are not marked as C/3 were cycled at a C/6 rate. Therefore, a comparison between the loss mechanisms for NG cells with 0.25 and 1.0PES211 electrolyte, as well as between cycling rates, can be made. For these experiments, dV/dQ analysis was performed on slow C/20 rate cycles that were run at the beginning and at the end of testing for each cell. Fits were made as described in Section 3.2.3, and the parameters for positive and negative mass loss as well as relative slippage were determined, as shown in the figures below.

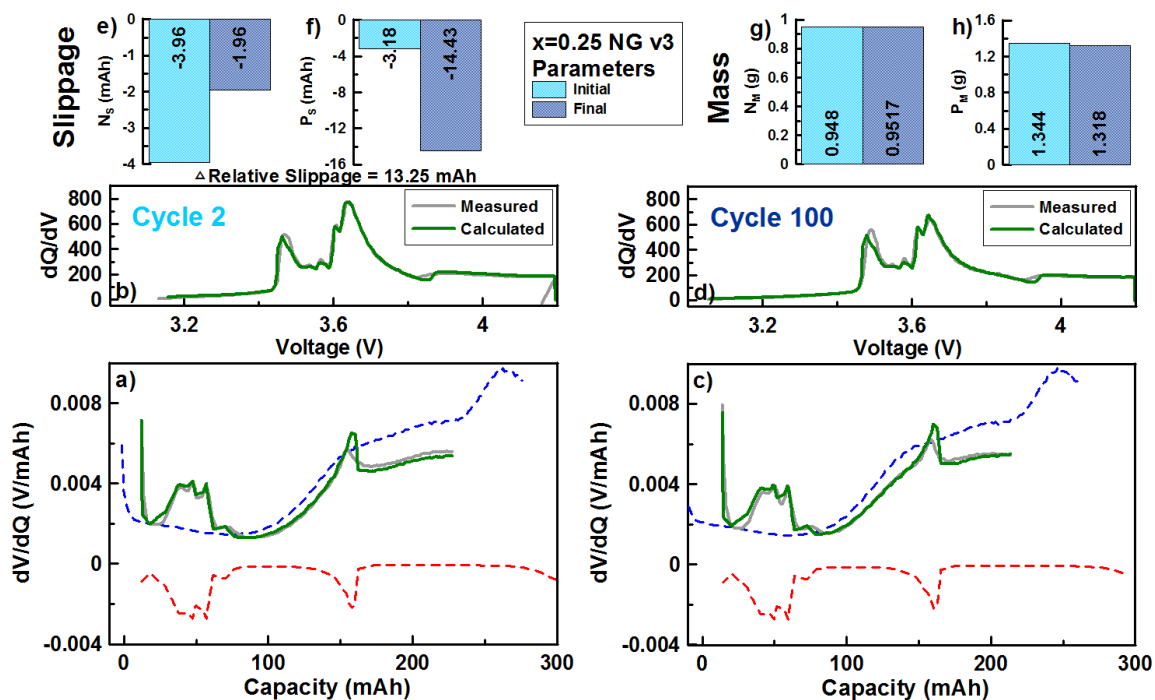


Figure 5.11: dV/dQ analysis of 0.25PES211 NG v3. The dV/dQ and corresponding dQ/dV fits are shown at the beginning of cycling (a,b) and at the end of cycling (c,d). Panels e-g show the fit parameters for the beginning (light blue) and end of cycling (dark blue). This cell was cycled at C/6 between 3.0 V and 4.2 V at 40°C.

Figure 5.11 shows the dV/dQ analysis for cell x=0.25 NG v3. The dV/dQ fit and resulting dQ/dV at the beginning of testing are shown in panels a and b; the fits at the end of testing are shown in panels c and d. The measured dV/dQ vs. Q and dQ/dV vs. V curves are shown in gray, and the calculated fits are shown in green. For the dV/dQ plots, the positive and negative differential voltage curves are shown in dotted blue and red, respectively. Panels e-h show the fit parameters in bar graphs, with the beginning of testing parameters shown in light blue and the end of testing parameters shown in dark blue. Figures 5.11e and f show the positive and negative electrode slippages. These slippages indicate where the negative and positive half cell differential voltage curves begin relative to the full cell curve. The change in relative slippage between the beginning and end of testing,

$$\Delta\text{Relative Slippage} = (N_s - P_s)_{\text{final}} - (N_s - P_s)_{\text{initial}} \quad (5.1)$$

quantifies the amount of inventory loss due to shift loss, i.e. SEI growth and repair, as described in Section 2.4. This is calculated from the slippages presented in Figures 5.11e and f, and is displayed below those panels to be 13.25 mAh. The fitting parameters show little to no significant mass loss. This is not unexpected for electrode materials known to exhibit excellent cycling stability, such as graphite and NMC. The small amount of positive mass loss suggested by the fits would have no impact on the cell capacity. One can see this by looking at the positive electrode differential capacity curve shown in red in Figures 5.11a and c; if this was slightly made smaller, it would have no effect on the full cell curve. Therefore, it is proposed that the primary mechanism of capacity loss for this cell is shift loss—consistent with the hypothesis of SEI growth causing the large pressure growth observed in 0.25PES211 NG cells.

Figure 5.12 shows differential voltage analysis for a 0.25PES211 cell cycled at C/3—double the rate of the cell presented in the previous figure. It was previously shown that 0.25PES211 NG cells exhibit a cycle dependence to capacity loss, therefore, it is unsurprising that this cell cycled at C/3 shows significantly more change in relative slippage compared to the C/6 cell (25.26 vs. 13.25 mAh), suggesting more SEI growth. Again, no significant mass loss is observed.

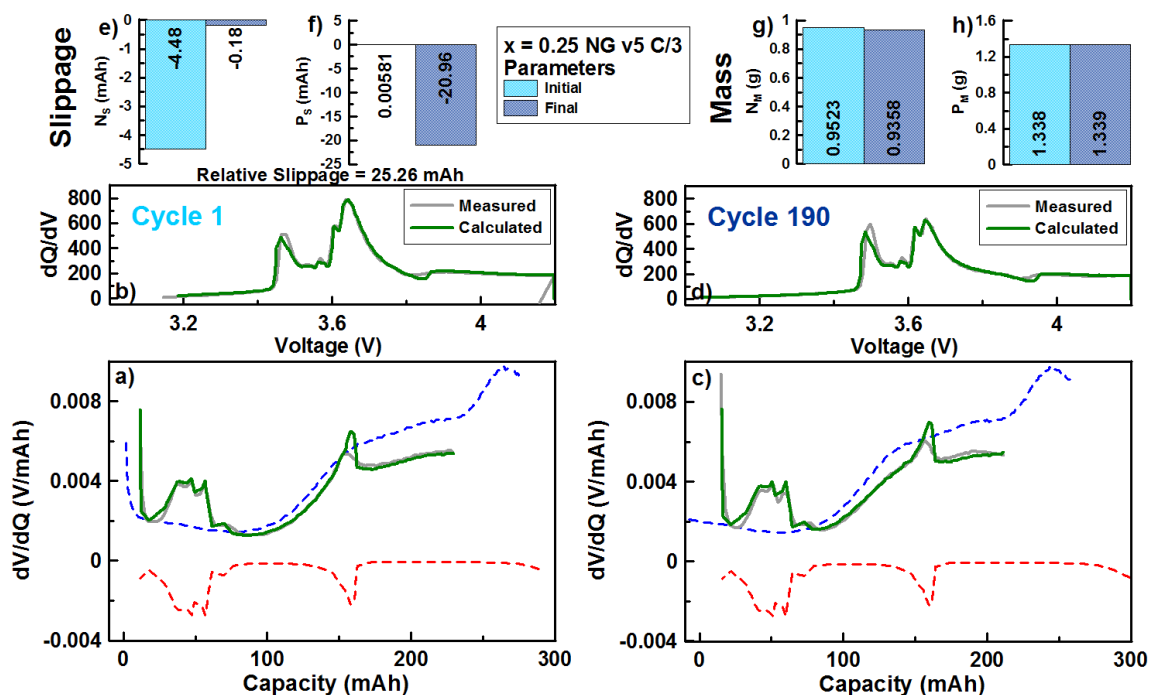


Figure 5.12: dV/dQ analysis of 0.25PES211 NG v5 C/3. The dV/dQ and corresponding dQ/dV fits are shown at the beginning of cycling (a,b) and at the end of cycling (c,d). Panels e-g show the fit parameters for the beginning (light green) and end of cycling (dark green). This cell was cycled at C/3 between 3.0 V and 4.2 V at 40°C.

For conciseness, the remaining detailed plots of the dV/dQ analysis have been put in Appendix A.1.3. Figure 5.13 summarizes the relevant parameter information derived from fitting for the cells presented in Figures 5.11 and 5.12, as well as the remaining fits shown in Appendix A.1.3. The 0.25PES211 NG cells cycled at C/6 and C/3 are shown in green and light green bars respectively, and the 1.0PES211 NG cells cycled at C/6 and C/3 are shown in blue and light blue respectively. The time the cells were cycled for and the number of cycles completed are shown in Figures 5.13d and e, respectively. The percentage of active electrode mass remaining after cycling, i.e. $Final\ Mass / Initial\ Mass * 100\%$, is given for the negative and positive electrodes in panels a) and b). No significant (i.e. enough to affect the full cell capacity) mass loss was experienced for either electrode

in any of these tests. Therefore, the primary mechanism for capacity loss in these cells is SEI growth, represented by the significant change in relative slippage shown in Figure 5.13c.

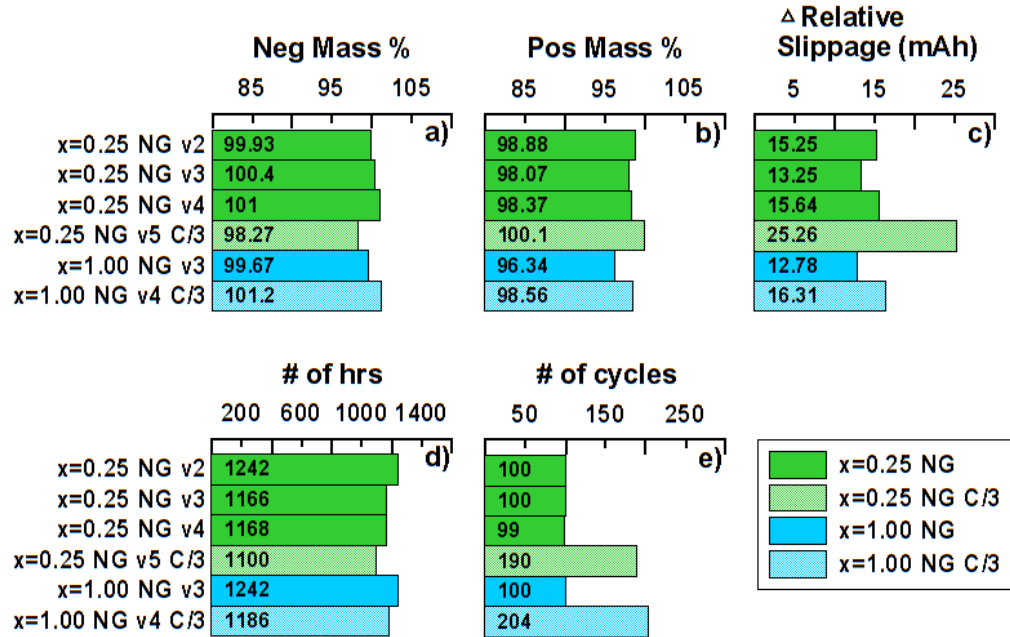


Figure 5.13: Summary of dV/dQ fit parameters for NG 0.25PES211 (shown in green) and 1.0PES211 cells (shown in blue). C/3 cycling rates are shown in lighter colours than cells than ran at C/6.

The results of the dV/dQ analysis presented in Figure 5.13 show that cells with 0.25PES211 electrolyte experience more SEI growth than cells with 1.0PES211 electrolyte. This is especially apparent when comparing the cells that ran at a C/3 rate; the larger current amplified the effects of the cycle dependent SEI growth of the 0.25PES211 electrolyte cell. These results are consistent with the hypothesis that 0.25PES211 electrolyte forms a weaker SEI more prone to continual formation and growth. This is reflected in the capacity vs. time data for NG cells which show 0.25PES211 cells exhibit a worse capacity retention

than 1.0 cells. Although these results suggest that 0.25 NG cells do experience more SEI growth than 1.0 NG cells, the pressure measurements did not show a larger pressure growth in 0.25 NG cells. *In-situ* pressure measurements were unable to detect the larger SEI growth in the 0.25PES211 NG chemistry, and therefore were unable to accurately rank the performance of these cells.

5.2 Analysis of Cells with Silicon Negative Electrodes

5.2.1 Electrode Comparison

In-situ pressure evolution studies were performed on cells with silicon containing negative electrodes previously introduced in this thesis: Type B (LCO/Si alloy-graphite), Type C (NCA/SiO-graphite), Type D-i and Type D-ii (NCA/Si-C). Note that Type D-i and D-ii cells are the exact same chemistry, but Type D-ii cells have a larger capacity due to having thicker electrodes. Figure 5.14 shows the capacity of these cells plotted vs. cycle no. (a) and time (b). The results for Type B cells are shown in yellow crosses, Type C results are shown in green triangles, Type D-i results are shown in blue diamonds, and Type D-ii results are shown in red squares. Data for Type C, D-i and D-ii cells are shown in different shades for multiple trials. All cells were run at a targeted C/6 rate, except those labelled C/3.

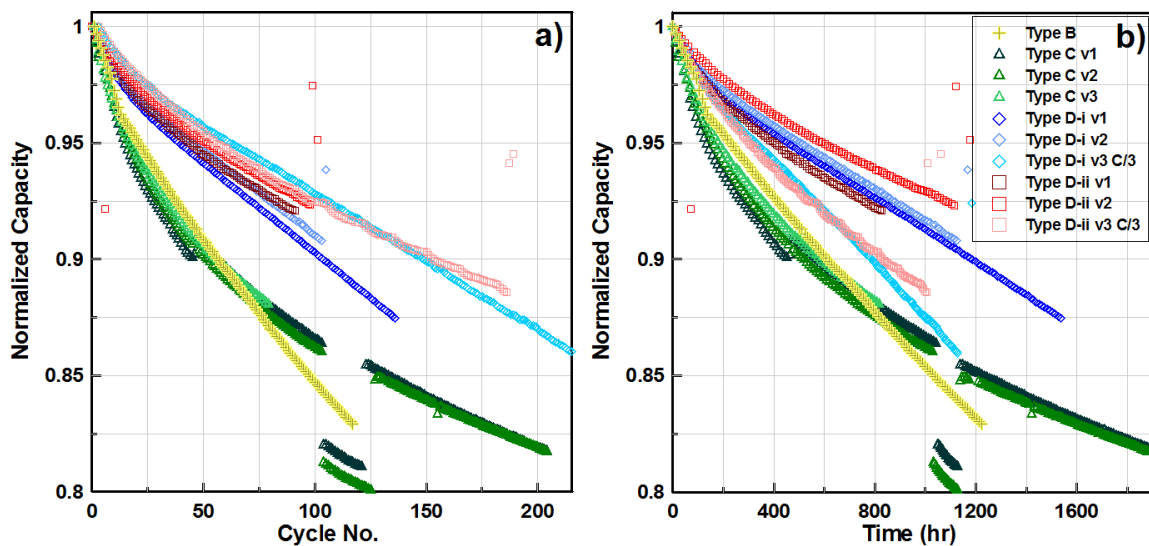


Figure 5.14: The normalized capacity of Type B (yellow crosses), Type C (green triangles), Type D-i (blue diamonds) and Type D-ii cells (red squares) plotted vs. cycle no. (a) and time (b). Cells were cycled at C/6 unless labeled otherwise, and cycled between 3.0 V and 4.2 V at 40°C.

Figure 5.14a shows that the capacity data for Type D cells run at C/3 agree with their C/6 counterparts when plotted vs. cycle no., suggesting primarily cycle dependent capacity loss mechanisms for Type D cells. Type B cells clearly experience the worst capacity retention, both in terms of absolute loss and the rate of loss at the end of testing. Type C cells show similar poor performance in the beginning of cycling, resulting in a large amount of absolute loss. However, the rate of capacity loss these cells exhibit dramatically reduces such that by the end of testing, the rate of loss of Type C cells is the lowest among silicon containing cells presented in Figure 5.14. Type D-i and D-ii cells exhibit similar performance during the beginning of cycling, however, around cycle 75 the loss rate of D-ii cells begins to turn such that these cells continue cycling with a lower capacity loss rate than D-i cells. Therefore, according to the rate of capacity loss at the end of cycling, the

ranking of cell performance from best to worst is Type C > Type D-ii > Type D-i > Type B.

Figure 5.15 shows long-term cycling data to clearly show that the capacity loss rate at the end of cycling is the important metric to judge cell performance, and thus justify that Type C cells are the best silicon containing cells despite their early absolute capacity loss. One might look at the previous Figure 5.14 and think that Type D-ii cells show superior performance compared to Type C cells, therefore, the long-term cycling data for these cells are compared in Figure 5.15. All cells were cycled at C/3 except for Type C v2, which was cycled at C/6. Cell Type C v2 C/6 and Type D-ii v3 C/3 are the short-term pressure tests previously shown in Figure 5.14; they completed about 200 cycles. Type C LT1 and LT2 and Type D-ii LT1 and LT2 are long-term cycling tests which were performed by Xiaowei Ma and William Stone (Dalhousie University). Figure 5.15 clearly shows that Type C cells are superior to Type D-ii cells long-term.

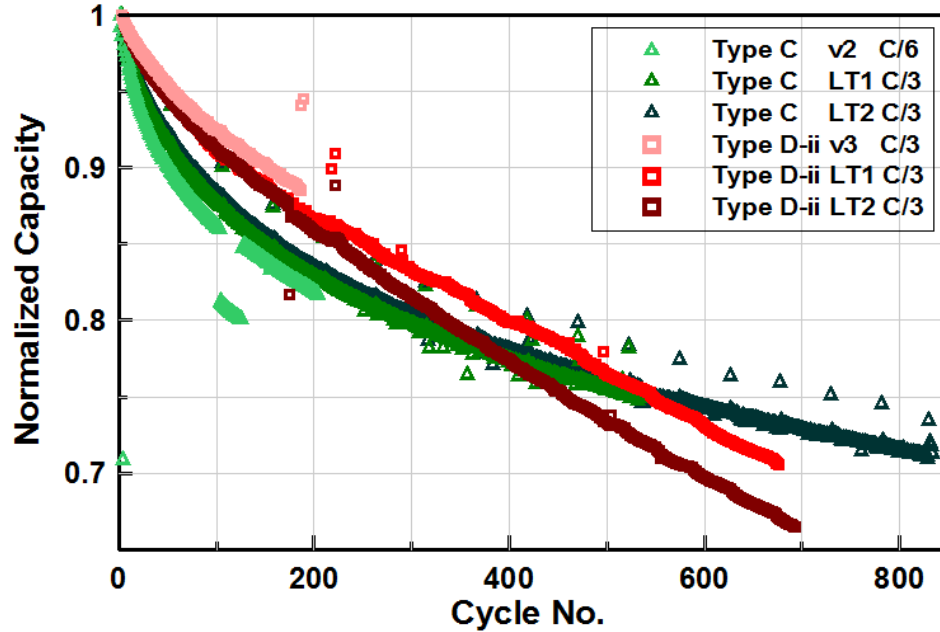


Figure 5.15: Long-term cycling data comparing the performance of Type C and Type D-ii cells. All cells were cycled at C/3 except for Type C v2 which was cycled at C/6. Cells were cycled between 3.0 V and 4.2 V at 40°C. The long-term cycling data was collected by Xiaowei Ma and William Stone (Dalhousie University).

Figure 5.16 shows the pressure vs. time profiles for each silicon-containing cell. Each panel a-d shows results for a different cell type. Figure 5.16 shows that differing initial pressures between cells of the same type affects pressure growth but not capacity retention. For example, all 3 Type C trials were initiated at significantly different pressures. The higher pressure tests exhibited a larger pressure swing than those initiated at lower pressures. Regardless, all three tests exhibited very similar capacity retention, as seen in Figure 5.14. From the pressure vs. time behavior of each cell type presented in Figure 5.14, it is clear that some cells exhibited a larger pressure growth than others. Type C cells show a very flat pressure evolution after about 100 hours of cycling. Type D-ii cells show the next largest pressure growth, with the rate of growth of the cell cycled at C/3 being the

largest. The largest pressure growths are experienced by Type D-i and B cells. This ranking of pressure growth is consistent with the capacity retention rankings, supporting the claim that pressure measurements can be used to predict cell performance. This is also shown with the metrics for pressure growth which are presented in Figure 5.17.

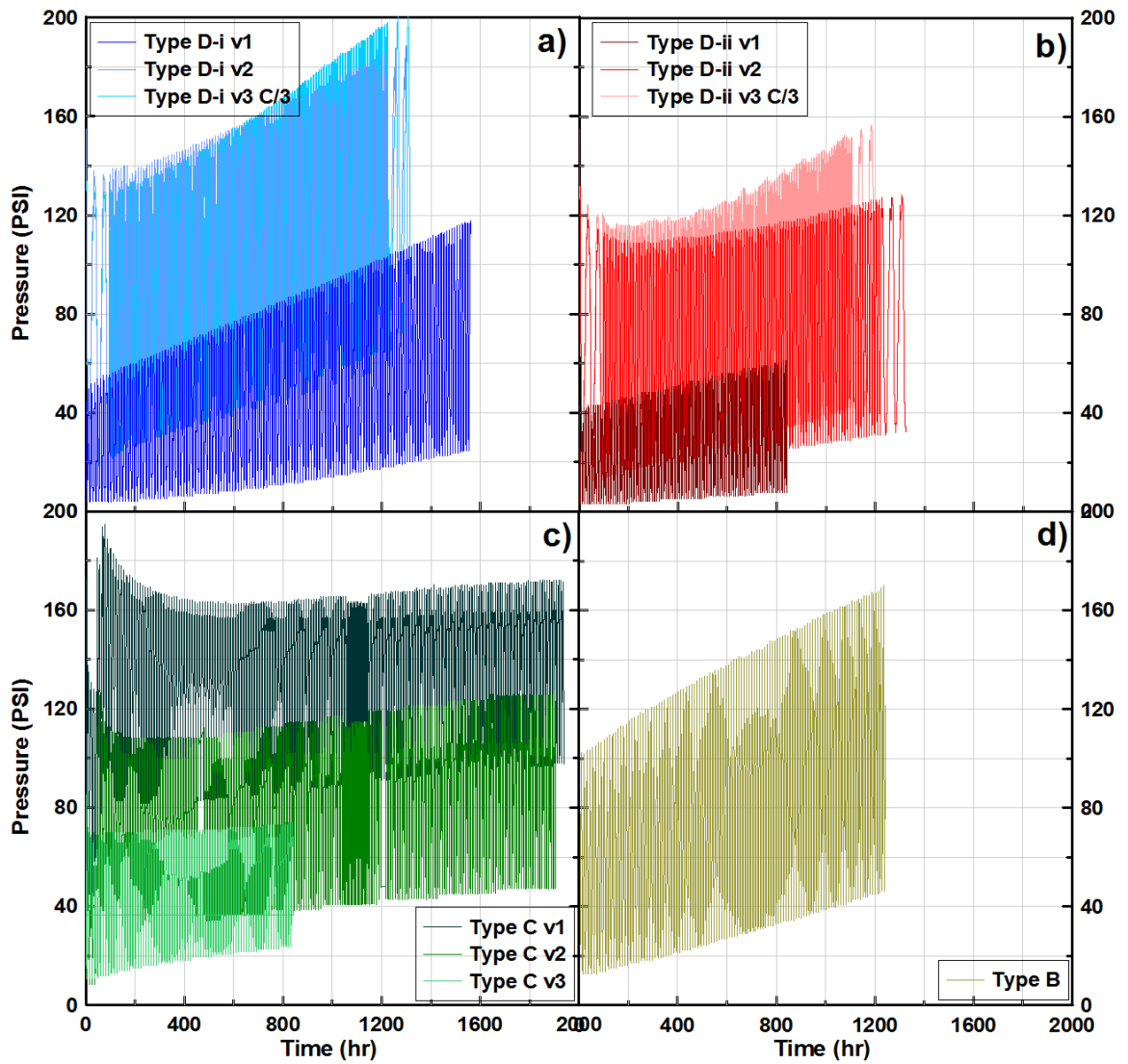


Figure 5.16: The pressure vs. time measurements for a) Type D-i, b) Type D-ii, c) Type C and d) Type B cells. Colour shades distinguish different trials for each cell type. Cells were cycled at C/6 unless labeled otherwise, and cycled between 3.0 V and 4.2 V at 40°C.

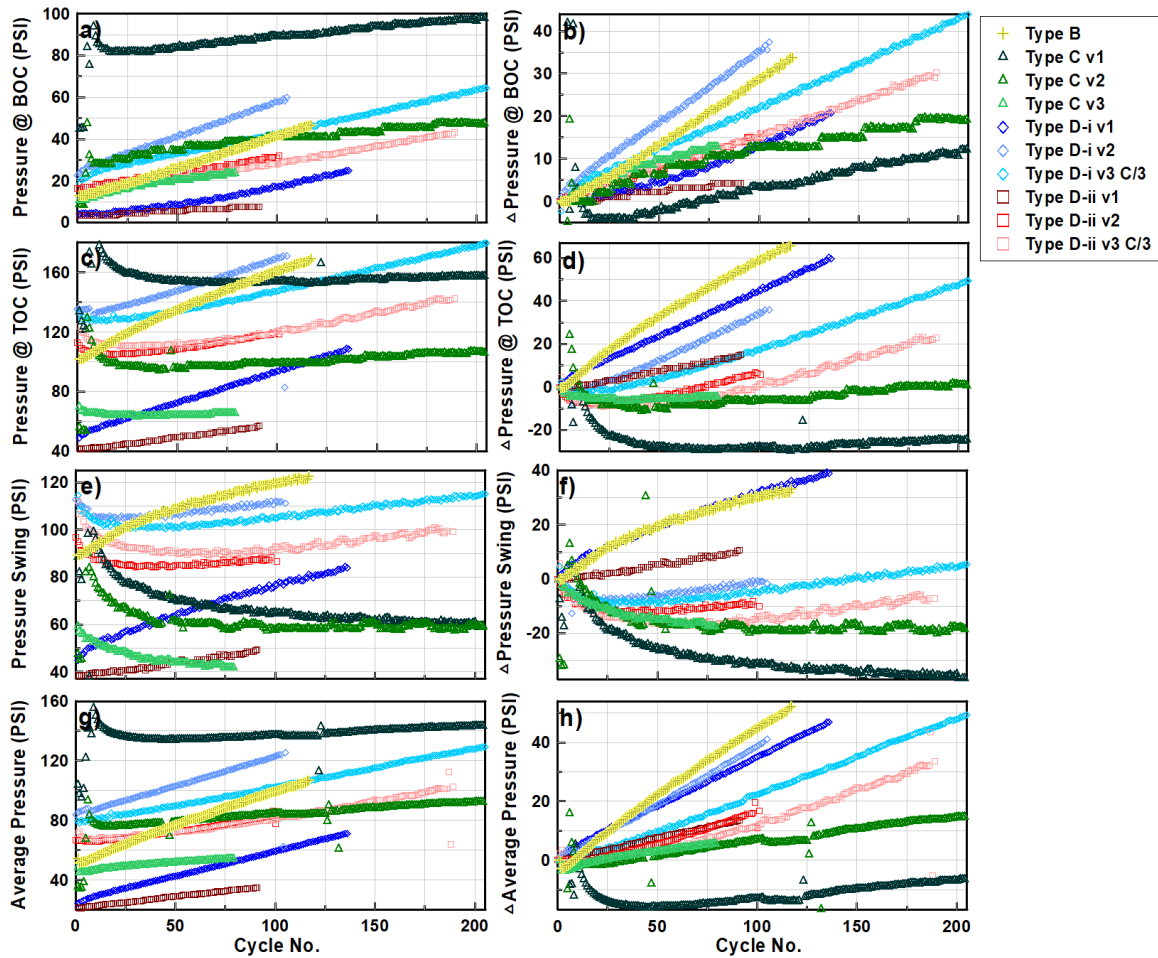


Figure 5.17: Metrics of pressure evolution for Type B (yellow crosses), Type C (green triangles), Type D-i (blue diamonds) and Type D-ii cells (red squares). Each row shows the metric (left) and the change in the metric (right): a,b) the pressure at the bottom of charge; c,d) the pressure at the top of charge; e,f) the pressure swing; g,h) the average pressure. The capacity vs. time data for these cells is given in Figure 5.14.

The pressure growth metrics presented in Figure 5.17 are consistent with the analysis made in the discussion above. Type C cells show the flattest pressure growth. Type D-i cells experience a larger pressure growth rate than D-ii cells, and the C/3 cells show a larger pressure growth than C/6 cells suggesting a cycle dependent mechanism for pressure growth, consistent with the cycle dependence to capacity loss. Type B cells, which experienced the worst capacity retention, exhibit among the largest pressure growth. To

clearly demonstrate this correlation between capacity loss and pressure growth, Figure 5.18 shows a summary of the data presented in this section.

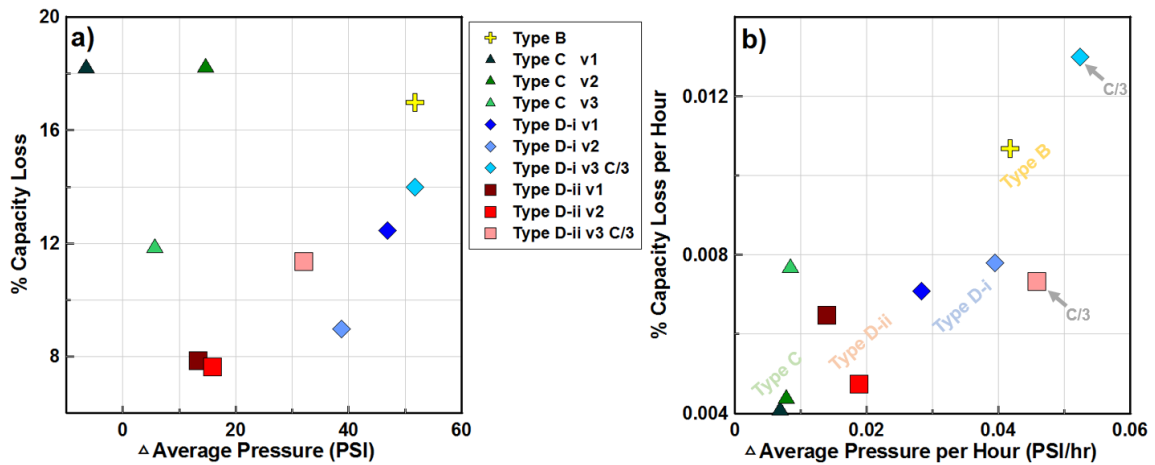


Figure 5.18: Summary of capacity loss vs. pressure growth data for silicon containing cells. a) Percent capacity loss vs. change in average pressure at the end of testing. b) Rate of capacity loss vs. rate of change in average pressure at the end of testing.

Figure 5.18a shows the percent capacity loss vs. the change in average pressure of silicon containing cells. This shows a trend of the best ranked cells showing the least capacity loss and pressure growth, and the worst cells showing the most capacity loss and pressure growth, except for the Type C cells which are outliers. As previously discussed, the absolute capacity loss is less informative about cell performance than the rate of capacity loss at the end of testing, therefore, Figure 5.18b shows that the rate of capacity loss vs. the rate of change in average pressure demonstrates a clearer trend. The disagreement in the capacity loss rate between cell Type C v3 and its brother cells was a result of this cell only running for about half as long, therefore, the rate in capacity loss had yet to fully exhibit the dramatic decrease these cells exhibit as shown in Figures 5.14 and 5.15. The disagreement between cell Type D-i v3 C/3 and Type D-ii v3 C/3 with their respective

brother cells is caused by these cells running at double the C-rate. This resulted in larger capacity loss rates and pressure growth rates, shifting these trials up and to the right relative to their brother cells. Figure 5.18 shows that larger pressure growth corresponded to worse capacity retention in the silicon containing cells investigated in this work, supporting the claim that pressure measurements can be used to rank the performance of cells with different electrode chemistries. The hypothesis that more SEI growth is cause of poorer capacity retention and larger pressure growth is investigated with differential voltage analysis in the following section.

5.2.2 Differential Voltage Analysis

Differential voltage analysis was performed on Type D-i and D-ii cells to elucidate the mechanisms for capacity loss and attempt to correlate them with the measured pressure growth. Figure 5.19 shows the dV/dQ analysis for cell Type D-i v2. Panels a and b show the dV/dQ fit and resulting dQ/dV curves at the beginning of testing, and panels c and d show these curves at the end of testing. The measured curves are shown in gray and the calculated fits are overlaid in green. The fits presented here are not as good as presented in the previous section for the AG/NG cells—especially at low capacity and low voltage for the dV/dQ and dQ/dV fits, respectively. Obviously, this is not ideal, but from the experience of the author, it is tough to make decent fits of cells with silicon-containing negative electrodes. Panels e-h show the fit parameters for the fit at the beginning of testing (light blue) and the fit at the end of testing (dark blue). The positive and negative slippages shown in panels e and f are used to calculate the change in relative slippage, displayed below these panels. The change in relative slippage normalized by the initial cell capacity * 100% is also shown. No negative mass loss, and about 8% positive mass loss is observed.

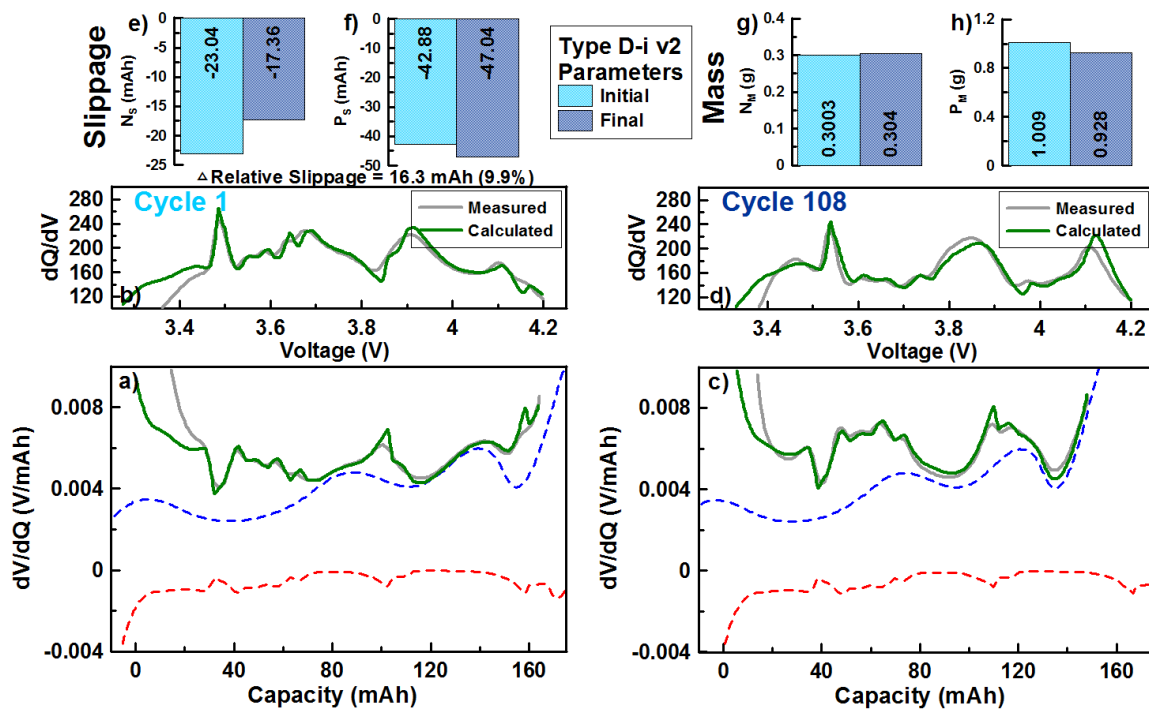


Figure 5.19: dV/dQ analysis of cell Type D-i v2. The dV/dQ and corresponding dQ/dV fits are shown at the beginning of cycling (a,b) and at the end of cycling (c,d). Panels e-g show the fit parameters for the beginning (light green) and end of cycling (dark green). This cell was cycled at C/6 between 3.0 V and 4.2 V at 40°C.

Figure 5.20 shows the dV/dQ analysis for cell D-i v3 C/3—run at a double the rate of the previous cell, therefore accumulating approximately double the number of cycles. Accordingly, the cell experiences a larger change in relative slippage. A similar amount of positive mass loss is observed.

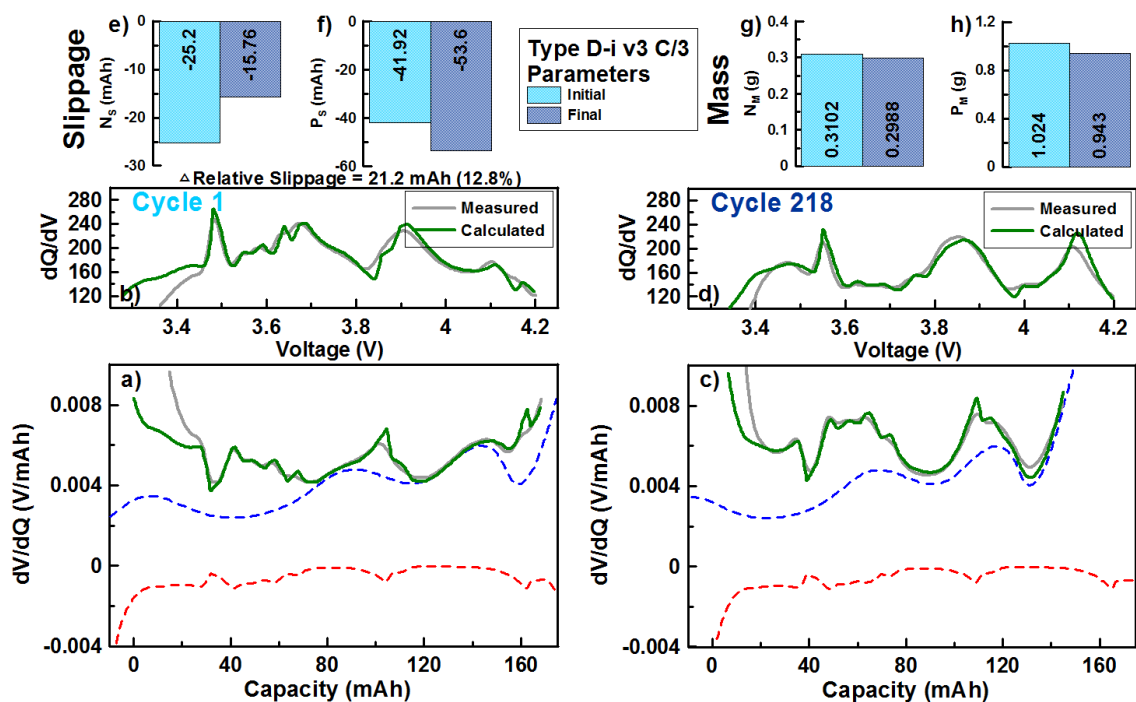


Figure 5.20: dV/dQ analysis of cell Type D-i v3 C/3. The dV/dQ and corresponding dQ/dV fits are shown at the beginning of cycling (a,b) and at the end of cycling (c,d). Panels e-g show the fit parameters for the beginning (light green) and end of cycling (dark green). This cell was cycled at C/3 between 3.0 V and 4.2 V at 40°C.

Figure 5.21 summarizes the relevant parameter information derived from all of the dV/dQ fitting performed on Type D cells. For conciseness, the remaining fits which were not presented in detail in this section are presented in Appendix A.1.3. Figure 5.21d and e show the amount of time and the number of cycles the cells were cycled for. Panels a and b show the normalized negative and positive active mass, i.e. *Final Active Mass / Initial Active Mass* * 100%. Panel c shows the change in relative slippage. Since Type D-i and D-ii cells have significantly different capacities, the slippage is normalized by the initial cell capacity * 100%. Panel c shows that the Type D-ii C/3 cell experienced more change in relative slippage than the Type D-ii C/6 cells, consistent with the cycle dependent capacity loss of these cells and the hypothesis of more SEI growth. However, Type D-ii

cells exhibit more slippage than Type D-i cells. This is inconsistent with the hypothesis that more SEI growth occurs in Type D-i cells, causing worse capacity retention and larger pressure growth. Additionally, Type D-ii cells exhibit more negative active mass loss than Type D-i cells. Therefore, the superior performance of Type D-ii cells can only be rationalized by the greater loss in positive active mass which Type D-i cells exhibit

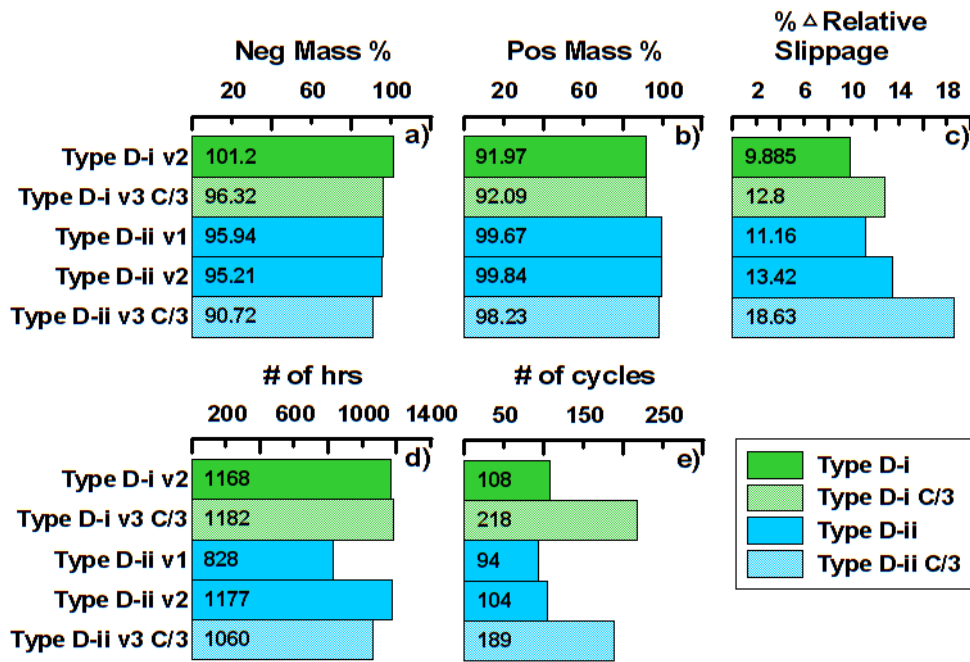


Figure 5.21: Summary of dV/dQ fit parameters for Type D-i (shown in green) and D-ii cells (shown in blue). C/3 cycling rates are shown in lighter colours than cells than ran at C/6.

The dV/dQ analysis presented in this section does not convincingly demonstrate that SEI growth is the cause of the pressure growth in Type D cells. The C/3 cells show more slippage than C/6 cells, which is consistent with the hypothesis that more SEI growth is the cause of the larger pressure growth of cells with cycle dependent capacity retention. However, Type D-i cells do not show more relative slippage than Type D-ii cells, therefore

there is no evidence that the larger pressure growth of the former is caused by more SEI growth. One possibility is that larger positive mass loss in Type D-i cells is the cause of the larger pressure growth. More work is required to further elucidate the mechanisms for pressure growth in Type D-i and D-ii cells.

Chapter 6: Conclusions & Future Work

6.1 Conclusions

High energy density electrodes are desired to reduce the size and cost of Li-ion cells while maintaining the same energy output. However, some high energy density electrode materials, such as silicon and silicon composites, experience a large volume expansion during lithiation. As was shown in this work, electrode volume expansion causes Li-ion pouch cells to expand. It is important to know how much the electrodes of a practical Li-ion cell will change in volume when charged so commercial and industrial implementation of such cells leave enough room to accommodate this expansion. To that end, this thesis work presented *in-situ* methods for measuring the volume evolution of Li-ion pouch cells. Direct volume measurements via Archimedes' principle, as well as other in-direct techniques that measure a response due to volume change, namely *in-situ* thickness and *in-situ* pressure measurements, were utilized. In Chapter 4, these techniques were used to measure the volume expansion of six different types of Li-ion pouch cells with different electrode chemistries; two cell types with single-component graphite negative electrodes: Type A-i (NMC/artificial graphite) and Type A-ii (NMC/natural graphite); and four cell types with silicon-composite negative electrodes: Type B (LCO/Si alloy-graphite), Type C (NCA/SiO-graphite) and Type D-i and D-ii (NCA/Si-C) cells. The *in-situ* volume, thickness and pressure measurements showed that these pouch cells experienced a reversible volume change caused by the net electrode expansion and contraction during charge and discharge, consistent between measurement techniques.

In Section 4.2, the volume expansion of cells with single-component graphite negative electrodes was studied. It was determined that the volume expansion profile of these cells is mostly affected by the expansion of the graphite negative electrode; the volume change of the NMC positive electrode is minimal in comparison. Therefore, the negative electrode dominates the net full cell expansion, resulting in a symmetric volume expansion and contraction profile, with a plateau during charge and discharge caused by graphite staging during lithium intercalation.

Section 4.3 presented an analysis of the expansion profile the silicon-containing Type C NCA/SiO-graphite chemistry, which was then used to elucidate the expansions of the other silicon-containing cells measured in this work. Unlike the volume expansion of the single-component graphite cells, silicon-containing cells exhibit asymmetric expansion profiles caused by the charge/discharge hysteresis of silicon-containing electrode materials. Type C cells exhibit three distinct features which are explained in this work: i) a plateau during charge caused by graphite stage $2L \rightarrow 2$ transformation; ii) an asymmetric plateau near the top of charge caused by the competing expansion and contraction of the negative and positive electrode which effectively cancel each other out; and iii) a rapid volume contraction caused by silicon de-lithiation. These features are also seen in the expansion profiles of the other silicon-containing cells. Type D-i and D-ii NCA/Si-C cells exhibit each of these features. Type B LCO/Si alloy-graphite cells experience a similar expansion profile, however the plateau at the top of charge is not observed. This is caused by the different positive electrode chemistries. Type B cells use a LCO positive electrode which does not contribute an opposing contraction/expansion as NCA does in Type C cells.

Therefore, the expansion behavior of Type B cells is similar to the expansion of just the negative electrode of Type C cells, as demonstrated in Section 4.3.

In Chapter 5, the *in-situ* pressure measurement technique developed in this work was used to measure the long-term pressure (and therefore, volume) evolution of Li-ion pouch cells. It was determined that over tens of cycles, an irreversible pressure growth was observed. This work showed that cells which experienced large pressure growth consistently performed worse than those with lesser pressure growth. It was hypothesized that this is caused by greater SEI growth; more SEI would cause greater volume expansion, as well as worse capacity retention. Therefore, it was proposed that *in-situ* pressure measurements may be a useful technique for ranking the performance of Li-ion cell chemistries. This would be valuable because of the long lifetime requirements of Li-ion cells which necessitate the ability to predict which cell chemistries will achieve longer lifetime than others over short-term testing. Chapter 5 presented the preliminary evidence for the usefulness of *in-situ* pressure measurements in this endeavor.

Section 5.1 examined the capacity retention and the irreversible pressure growth of single-component graphite negative electrode cells with two different electrolyte formulations. Capacity vs. time data showed that Type A-i (AG) cells experienced superior capacity retention compared to Type A-ii (NG) cells, and cells that use 1.0PES211 electrolyte performed better than those with 0.25PES211 electrolyte. In a comparison between electrode chemistries, it was shown that AG cells experience a smaller pressure growth than NG cells, consistent with the hypothesis of less SEI growth resulting in the superior performance of AG cells. In a comparison between electrolyte chemistries, for AG cells, cells with 1.0PES211 electrolyte showed less pressure growth than cells with 0.25PES211

electrolyte, consistent with the superior performance 1.0PES211 electrolyte in AG cells. For NG cells, although 1.0PES211 electrolyte cells also showed better capacity retention than 0.25PES211 cells, there was no significant difference in pressure growth between cells with these electrolyte formulations. In some trials, 0.25PES211 NG cells experienced a larger pressure growth than 1.0PES211 NG cells, contrary to the capacity performance. This is a case where *in-situ* pressure measurements did not accurately rank cell performance, and the hypothesis that increased SEI growth was the cause of worse capacity retention and larger pressure growth was inconsistent. Further work is required.

Section 5.2 presented the pressure evolution of cells with silicon-composite negative electrodes. It was shown that *in-situ* pressure measurements were able to accurately rank the performance of these cells; the cells with the lowest rates pressure growth experienced the best performance. Although it was thought that this would be a result of less SEI growth, differential voltage analysis showed no evidence for different amounts of SEI growth between Type D-i and D-ii cells which experience different rates of pressure growth and capacity loss.

6.2 Future Work

This work has demonstrated promising results indicating that *in-situ* pressure measurements may be used to rank the performance of Li-ion cells. In all cases presented in this work which compared the performance and pressure growth of cells with different electrode chemistries, *in-situ* pressure measurements accurately ranked cell performance. When comparing the performance and pressure growth of cells with the same electrodes and different electrolytes, pressure measurements accurately ranked performance in one

electrode chemistry (AG cells with 0.25 vs 1.0 PES211 electrolyte), but not another (NG cells with 0.25 vs. 1.0 PES211 electrolyte). Therefore, more studies are required to investigate the usefulness of pressure measurements for ranking the lifetime of cells with different electrolyte formulations.

More work to demonstrate the repeatability of pressure measurements is required. To these ends, future studies should employ an altered methodology to foster repeatability and ensure apt comparisons for pressure measurements between different cell chemistries. As laid out in the experimental section, the procedure for installing cells in the pressure measurement apparatus involved securing the cells charged to 3.8 V into superboats. The initial pressure was achieved by hand-tightening four screws to force the adjustable superboat wall against the pouch cell. However, hand-tightening the screws may not yield a uniform pressure distribution across a cell, or between multiple cells in different superboats. This may cause inconsistent pressure evolution. Additionally, initializing the cells at 3.8 V—the “middle of charge”, is not useful for making cell-to-cell comparisons. As different cell chemistries have different magnitudes of volume expansion and contraction, the pressures at the top and bottom of charge will be different between cell types. It was shown in Section 5.2 that the magnitude of the pressure at the bottom of charge affects pressure evolution, therefore it is critical to control this value, which is not accomplished by starting the cells at the middle of charge. Therefore, future studies should initialize all cells at the bottom of charge (i.e. 3.0 V for the experiments performed in this work). Additionally, screws should not be hand-tightened, but tightened with a torque-controlled driver to ensure pressure uniformity.

This work hypothesized that the correlation between larger pressure growth and poorer capacity retention is caused by increased SEI growth. This was investigated by utilizing dV/dQ analysis to quantify the mechanisms for capacity loss for Type A-ii NG cells with 0.25 and 1.0 PES211 electrolyte, and Type D-i and Type D-ii cells silicon-containing cells. This analysis was not performed for all of the pressure growth experiments because the necessary data was not available, namely, slow (i.e. C/20) cycles at the beginning and end of testing to perform the analysis on. All future *in-situ* pressure experiments should incorporate these cycles into the testing protocol so dV/dQ analysis can be more thoroughly used to correlate cell degradation mechanisms to pressure growth.

This work did not consider the effect of active electrode mass loss on pressure evolution. For a complete understanding of these measurements, this must be considered in future work. The effect of active mass loss on the volume expansion and contraction of a cell, and thus the pressure swing, depends on if electrode particles are fully expanded, fully contracted, or somewhere in-between when they are lost. It is possible that loss of fully expanded particles will result in the pressure at the bottom of charge to increase, and the loss of fully contracted particles will cause the pressure at the top of charge to decrease. Such effects would be easier to track if the pressure was initialized at the bottom of charge and if dV/dQ analysis was performed on all experiments, as previously proposed.

In addition to consuming lithium inventory causing capacity loss, SEI growth contributes to cell degradation by increasing cell impedance, thereby lowering the average voltage and thus the energy output of a cell. Electrochemical impedance spectroscopy (EIS) is non-destructive, fast measurement technique for measuring the impedance of a Li-ion cell, and, therefore, is a useful tool for analyzing the degradation due to impedance growth of Li-ion

cells.^{25,52} This technique measures the total impedance of a Li-ion cell, which is a combination of several different processes: ohmic resistance of the electrolyte, current collectors, and other resistive cell components; faradaic impedance caused by charge transfer through electrode interfaces and through the SEI; and Warburg impedance caused by solid-state diffusion of Li into the electrode active material.^{53–55} The impedance caused by charge transfer through the SEI is of interest to this thesis work because it can elucidate the thickness of the SEI. In theory, EIS spectra can be fit with equivalent circuit models with parameters for each impedance element, allowing the SEI charge transfer impedance to be obtained directly.^{54,56} However, in practice, fitting the relatively simple EIS spectra with parameters for each impedance element can result in unreliable fits.⁵⁷ Regardless, it is clear that growth of the SEI charge transfer impedance causes the total cell impedance to grow. Therefore, measuring impedance evolution with EIS can elucidate SEI growth, in conjunction with *in-situ* pressure measurements. Additionally, symmetric cells (cells with positive vs. positive or negative vs. negative electrodes) can be made from the initial and cycled pouch cells from *in-situ* pressure measurements to distinguish positive and negative electrode SEI growth.⁵⁸ Another method to measure impedance growth that would be useful in conjunction with pressure measurements is monitoring ΔV , the change in average voltage between charge and discharge, over time. ΔV growth is another indication of impedance growth, and therefore would be useful in conjunction with *in-situ* pressure data to correlate to SEI growth.

In-situ pressure measurements may also be useful to study SEI formation. Robust, stable initial SEI layers are critical to the performance of Li-ion cells.^{25,52} Electrolyte additives are known to play an important role improving SEI formation and thus cell performance.³¹

However, the effect of additives on SEI and its morphology which result in superior performance is not well understood. Quantitative differential capacity (dQ/dV) analysis has been used to study the underlying chemistry of SEI formation from additives and additive blends.⁵⁹⁻⁶² Monitoring dQ/dV vs. V allows one to determine at which voltage electrolyte reduction occurs as well as the magnitude of the reduction and thus draw inference about the chemical effects of additives on SEI formation. Perhaps, in an analogous manner, differential pressure, i.e. dP/dV vs. V measurements may provide useful insight about the physical properties of the SEI during formation and the mechanical effects of additives. Such physical information may lead toward a better understanding of what makes a good SEI.

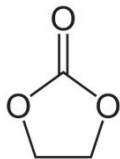
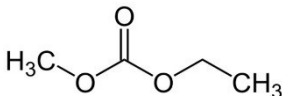
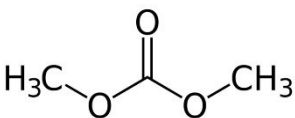
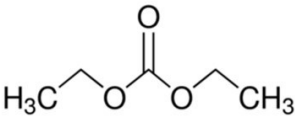
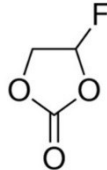
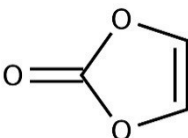
It is the hope of the author that these proposed future works should elucidate the usefulness of the *in-situ* pressure measurement technique presented in this work. If successful, this technique could become another tool in the toolbox of a Li-ion battery researcher. This would be a valued contribution to Li-ion field that the author would be proud of.

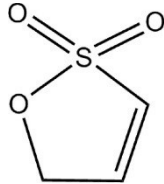
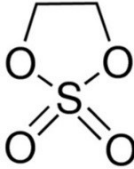
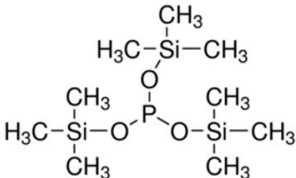
Appendix

A.1 Additional Data & Information

A.1.1 Solvent and Additive Chemical Structures

Table A.1: Solvents and additives used in the electrolyte in this work.

Abbreviation	Name	Chemical Structure	Supplier & Purity
EC	ethylene carbonate		BASF 99.99%
EMC	ethylmethyl carbonate		BASF 99.99%
DMC	dimethyl carbonate		BASF 99.99%
DEC	diethyl carbonate		BASF 99.99%
FEC	fluoroethylene carbonate		BASF 99.94%
VC	vinylene carbonate		BASF 99.97%

PES	prop-1-ene-1,3-sultone		Lianchuang Medicinal Chemistry Co., Ltd 98.2%
DTD	1,3,2-Dioxathiolane-2,2-dioxide		Sigma-Aldrich 98%
TTSPi	tris(trimethylsilyl)phosphite		Sigma-Aldrich >95%

A.1.2 Pressure Apparatus Compliancy

To determine the change in thickness a pouch cell exhibits when it causes a change in pressure in the *in-situ* pressure measurement apparatus, the compliancy of the pouch cell system was measured. This system consists of the pouch cell, the force distributing plate, and the load cell pressure sensor. This was measured for Type C and Type D cells, and also measured without any pouch cells, i.e. the compliancy of just the load cell. The compliancy was measured using the apparatus depicted in Figure A.1a. The system to be measured was placed under a pivoting thick steel bar, inside of a hydraulic press, with a 1 μm resolution dial gauge in contact with the steel bar. When the hydraulic press was activated, it exerted a force on the steel bar, putting pressure on the measured system, inducing a load cell measurement. As the bar was pushed down, the dial gauge displayed the change in position. The pressure vs. change in position x_{raw} was recorded. The bar acts as a lever, therefore the change in position of the bar at the dial gauge is larger than the

change in position over the pouch cell, since the dial gauge makes contact with the bar further from the pivot point than the pouch cell. Therefore, a correction is made to the measured position x_{raw} :

$$x = x_{raw} \frac{\text{distance from pivot to pouch cell}}{\text{distance from pivot to dial gauge}} \quad (\text{A.1})$$

where x is the change in position of the bar over the pouch cell. These measurements were performed at room temperature, and the pouch cells used for these measurements were dry (no electrolyte) cells that had never been charged. Figure A.1b shows the data from these measurements.

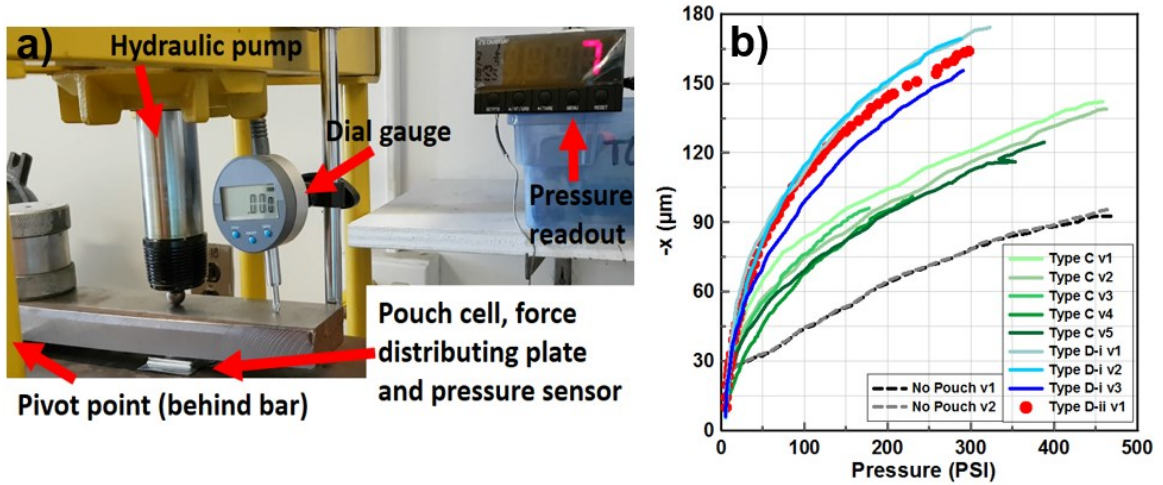


Figure A.1: a) Apparatus used to measure compliancy. b) Compliancy data for different pouch cell systems.

Figure A.1b shows that the load cell by itself is the least compliant, as expected. Additionally, Type D cells exhibit more compliance than Type C cells. This is also expected as it is speculated that the electrodes of Type C cells are more heavily calendared

than Type D cells. Since Type C electrodes have already been heavily compressed during the calendaring process, this renders the electrodes less compliant. Therefore, Type C cells as a whole are less compliant than Type D cells. The range of pressure pouch cells experienced in this work is about 20 to <200 PSI, therefore, the change in thickness experienced during these tests was in the range of 15 to 100 μm .

A.1.3 dV/dQ Analysis Fits

The differential voltage analysis fits which were presented in summary in Sections 5.1.3 and 5.2.2 are presented here. In some cases, the dV/dQ analysis at the beginning and end of cycling was not done on the exact same cell, i.e., the C/20 cycles necessary for reliable fits were only performed at the end of testing—not in the beginning in these cases. Therefore, the parameter comparison is made with a fit from the beginning of testing of another brother cell. This is not ideal. Cases where this was done are explicitly mentioned.

Additional Fits for Section 5.1.3

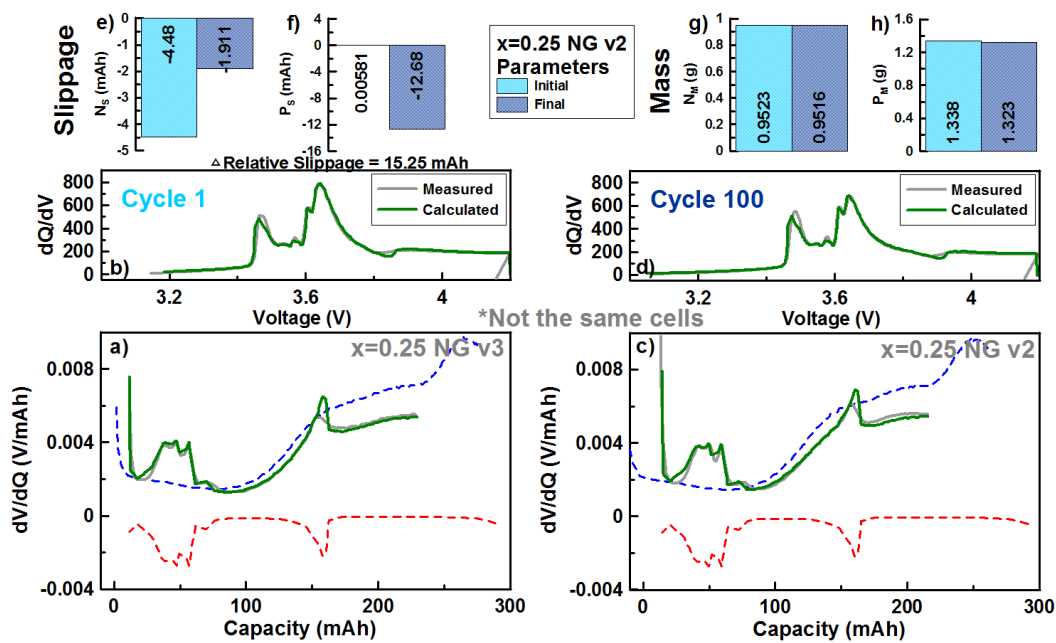


Figure A.2: Differential voltage analysis for cell $x=0.25$ NG v2. This cell was cycled at C/6 between 3.0 V and 4.2 V at 40°C.

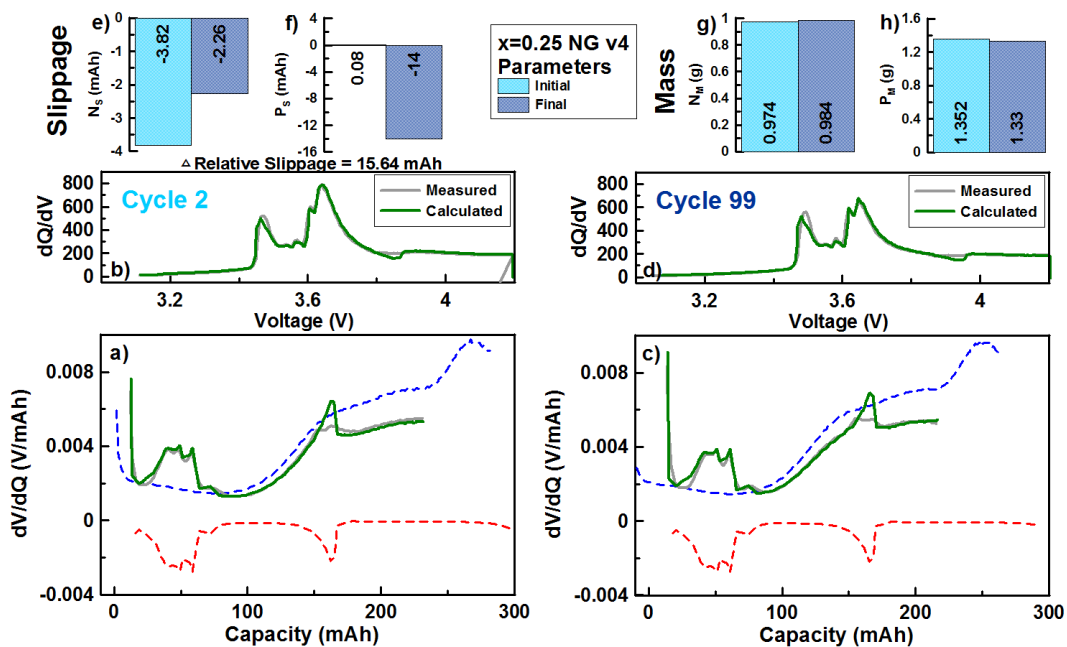


Figure A.3: Differential voltage analysis for cell $x=0.25$ NG v4. This cell was cycled at C/6 between 3.0 V and 4.2 V at 40°C.

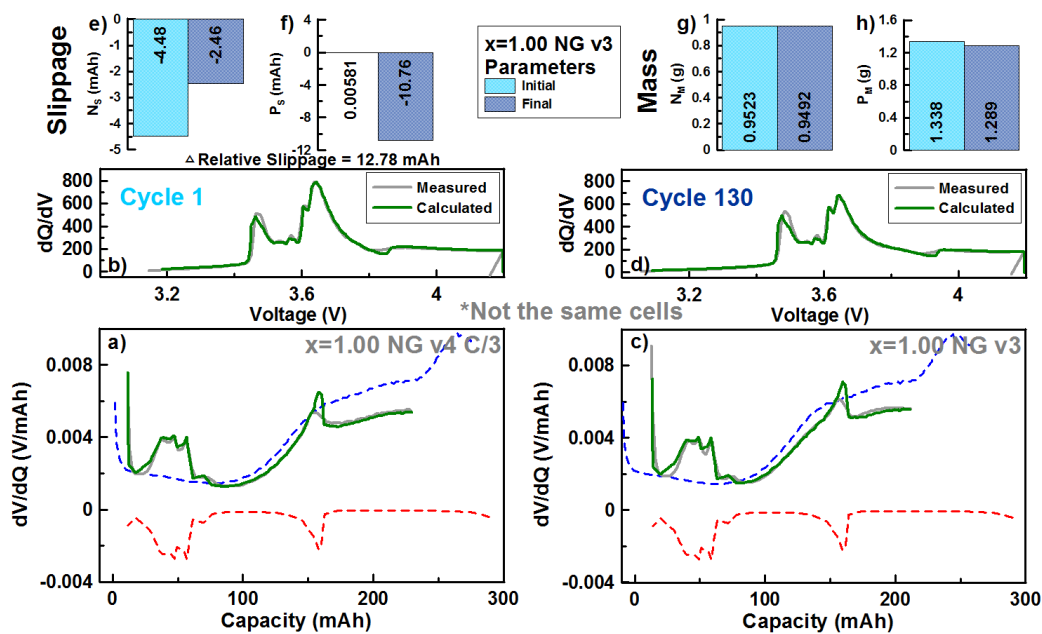


Figure A.4: Differential voltage analysis for cell x=1.00 NG v3. This cell was cycled at C/6 between 3.0 V and 4.2 V at 40°C.

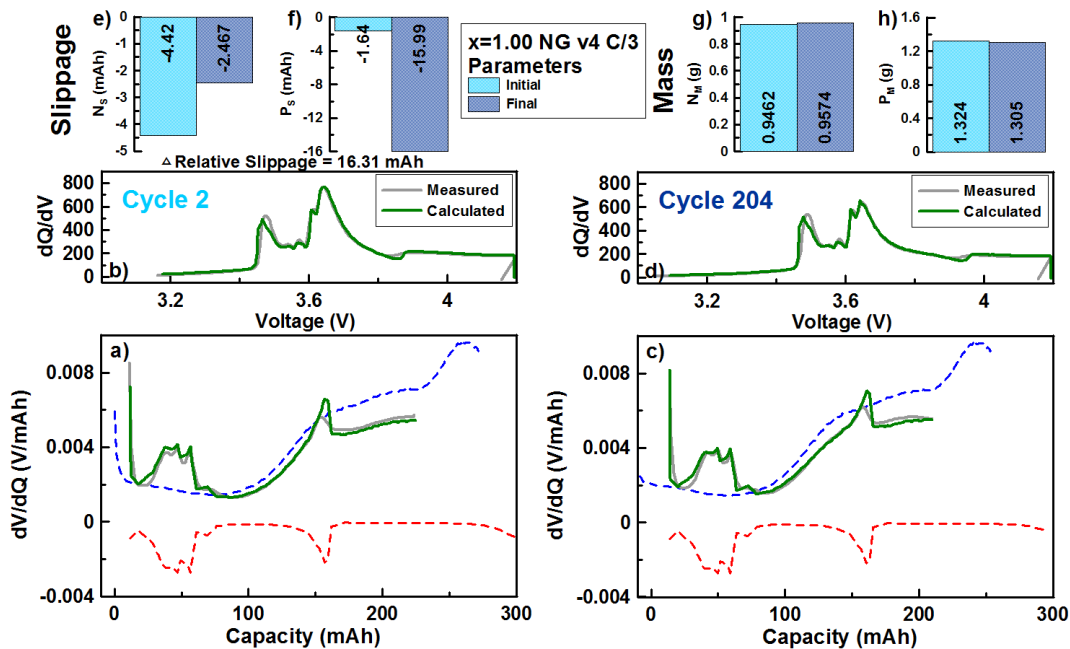


Figure A.5: Differential voltage analysis for cell x=1.00 NG v4 C/3. This cell was cycled at C/3 between 3.0 V and 4.2 V at 40°C.

Additional Fits for Section 5.2.2

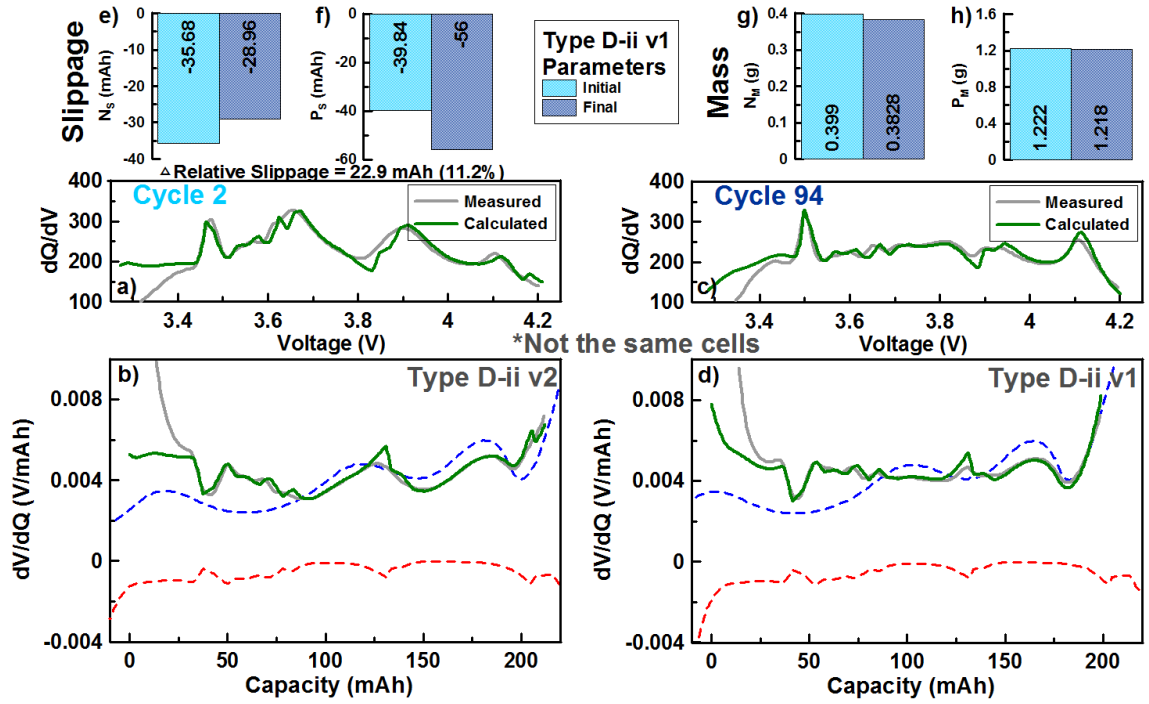


Figure A.6: Differential voltage analysis for cell Type D-i v1. This cell was cycled at C/6 between 3.0 V and 4.2 V at 40°C.

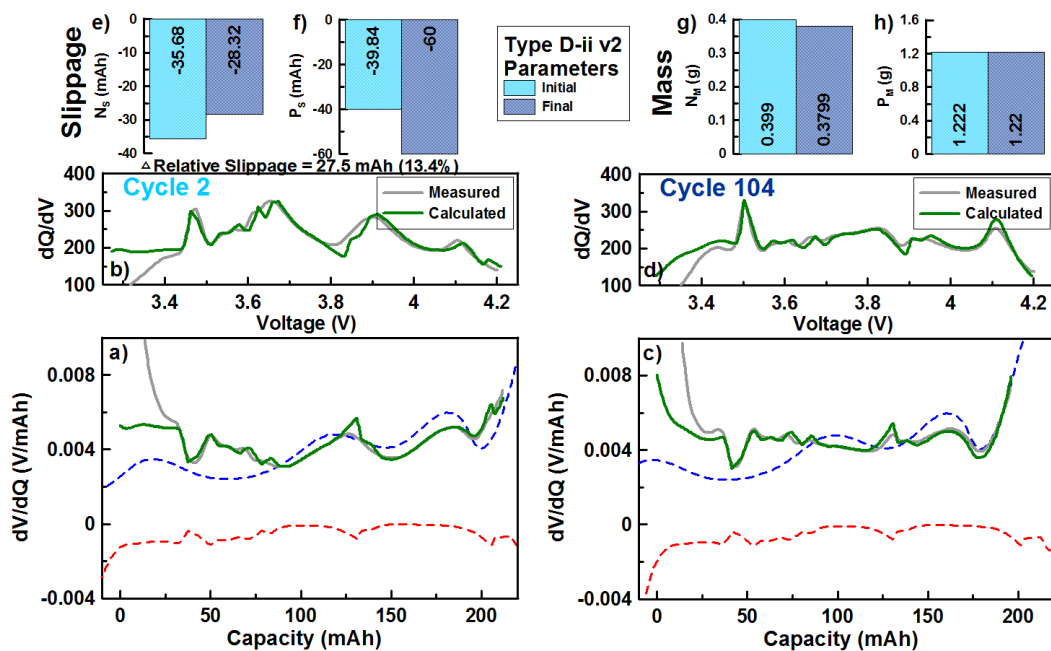


Figure A.7: Differential voltage analysis for cell Type D-ii v2. This cell was cycled at C/6 between 3.0 V and 4.2 V at 40°C.

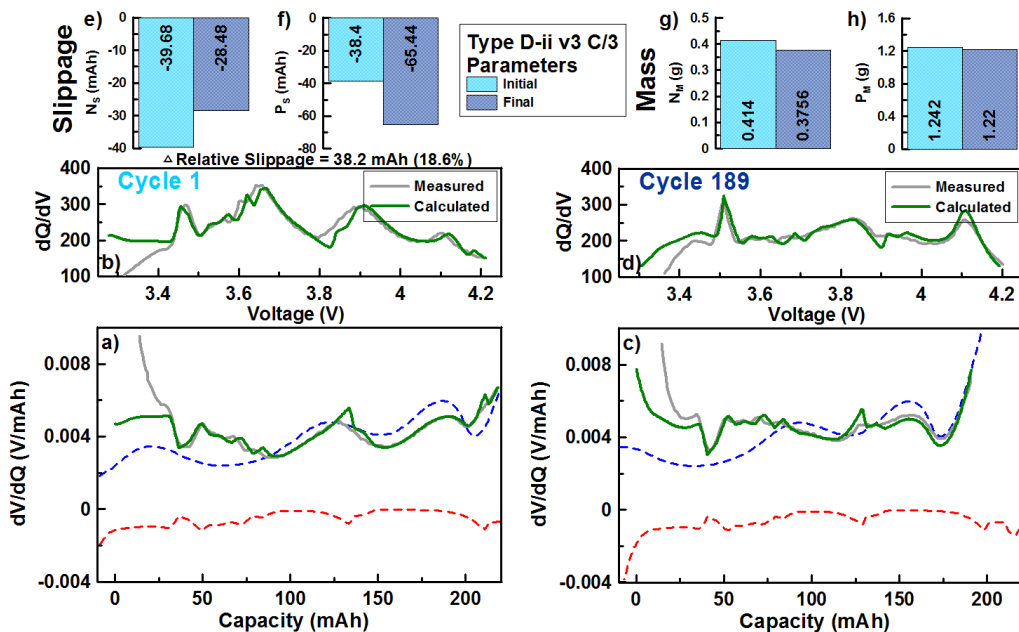


Figure A.8: Differential voltage analysis for cell Type D-ii v3 C/3. This cell was cycled at C/3 between 3.0 V and 4.2 V at 40°C.

A.2 Permissions

9/22/2017

RightsLink Printable License

Electrochemical Society, Inc LICENSE TERMS AND CONDITIONS

Sep 22, 2017

This is a License Agreement between Dalhousie University -- Alex Louli ("You") and Electrochemical Society, Inc ("Electrochemical Society, Inc") provided by Copyright Clearance Center ("CCC"). The license consists of your order details, the terms and conditions provided by Electrochemical Society, Inc, and the payment terms and conditions.

All payments must be made in full to CCC. For payment instructions, please see information listed at the bottom of this form.

License Number	4194280752126
License date	Sep 21, 2017
Licensed content publisher	Electrochemical Society, Inc
Licensed content title	Journal of the Electrochemical Society
Licensed content date	Jan 1, 1948
Type of Use	Thesis/Dissertation
Requestor type	Academic institution
Format	Print, Electronic
Portion	chapter/article
Title or numeric reference of the portion(s)	Volume, Pressure and Thickness Evolution of Li-Ion Pouch Cells with Silicon-Composite Negative Electrodes
Title of the article or chapter the portion is from	Volume, Pressure and Thickness Evolution of Li-Ion Pouch Cells with Silicon-Composite Negative Electrodes
Editor of portion(s)	N/A
Author of portion(s)	A. J. Louli, Jing Li, S. Trussler, Christopher R. Fell, and J. R. Dahn
Volume of serial or monograph.	164
Issue, if republishing an article from a serial	12
Page range of the portion	
Publication date of portion	2017
Rights for	Main product
Duration of use	Life of current and all future editions
Creation of copies for the disabled	no
With minor editing privileges	yes
For distribution to	Worldwide
In the following language(s)	Original language of publication
With incidental promotional use	no
The lifetime unit quantity of new product	Up to 499
Made available in the	?

<https://s100.copyright.com/CustomerAdmin/PLF.jsp?ref=dc957f4c-97f9-450e-9a04-c912aa313ae2>

1/5

following markets

Specified additional information	To be published in my thesis.
The requesting person/organization is:	Alexander J Louli
Order reference number	
Author/Editor	Alexander J Louli
The standard identifier of New Work	?
Title of New Work	Probing the Reversible and Irreversible Volume Expansion Observed in Li-ion Pouch Cells
Publisher of New Work	Dalhousie University
Expected publication date	Oct 2017
Estimated size (pages)	130
Total (may include CCC user fee)	0.00 USD
Terms and Conditions	

TERMS AND CONDITIONS

The following terms are individual to this publisher:

None

Other Terms and Conditions:

Permission is granted to include the above-referenced paper in your thesis, provided that you obtain permission of the other individual authors. In the thesis, please acknowledge the authors and the citation given above, and include the words: "Reproduced by permission of ECS — The Electrochemical Society."

STANDARD TERMS AND CONDITIONS

1. **Description of Service; Defined Terms.** This Republication License enables the User to obtain licenses for republication of one or more copyrighted works as described in detail on the relevant Order Confirmation (the "Work(s)"). Copyright Clearance Center, Inc. ("CCC") grants licenses through the Service on behalf of the rightsholder identified on the Order Confirmation (the "Rightsholder"). "Republication", as used herein, generally means the inclusion of a Work, in whole or in part, in a new work or works, also as described on the Order Confirmation. "User", as used herein, means the person or entity making such republication.

2. The terms set forth in the relevant Order Confirmation, and any terms set by the Rightsholder with respect to a particular Work, govern the terms of use of Works in connection with the Service. By using the Service, the person transacting for a republication license on behalf of the User represents and warrants that he/she/it (a) has been duly authorized by the User to accept, and hereby does accept, all such terms and conditions on behalf of User, and (b) shall inform User of all such terms and conditions. In the event such person is a "freelancer" or other third party independent of User and CCC, such party shall be deemed jointly a "User" for purposes of these terms and conditions. In any event, User shall be deemed to have accepted and agreed to all such terms and conditions if User republishes the Work in any fashion.

3. Scope of License; Limitations and Obligations.

3.1 All Works and all rights therein, including copyright rights, remain the sole and exclusive property of the Rightsholder. The license created by the exchange of an Order Confirmation (and/or any invoice) and payment by User of the full amount set forth on that document includes only those rights expressly set forth in the Order Confirmation and in these terms and conditions, and conveys no other rights in the Work(s) to User. All rights not expressly granted are hereby reserved.

References

- [1] G.E. Blomgren, The Development and Future of Lithium Ion Batteries, *J. Electrochem. Soc.* **164** (2017) A5019–A5025. doi:10.1149/2.0251701jes.
- [2] J.R. Dahn, G.M. Ehrlich, Lithium-Ion Batteries, in: Linden's Handbook of Batteries Fourth Ed., 2011. doi:10.1007/978-0-387-34445-4.
- [3] M.S. Whittingham, What Are the Ultimate Limits To Intercalation Reactions?, *Proceedings of the International Batterery Association*, 2013.
- [4] T. Marks, S. Trussler, A.J. Smith, D. Xiong, J.R. Dahn, A Guide to Li-Ion Coin-Cell Electrode Making for Academic Researchers, *J. Electrochem. Soc.* **158** (2011) A51–A57. doi:10.1149/1.3515072.
- [5] C. Pillot, The Rechargeable Battery Market and Main Trends 2014-2025, *Proceedings of the 32nd International Battery Seminar & Exhibit*, 2015.
- [6] J.R. Dahn, Phase Diagram of Li_xC_6 , *Phys. Rev. B.* **44** (1991) 9170–9177. doi:10.1103/PhysRevB.44.9170.
- [7] M.N. Obrovac, V.L. Chevrier, Alloy Negative Electrodes for Li-Ion Batteries, *Chem. Rev.* **114** (2014) 11444–11502. doi:10.1021/cr500207g.
- [8] T. Zheng, J.N. Reimers, J.R. Dahn, Effect of Turbostratic Disorder in Graphitic Carbon Hosts on the Intercalation of Lithium, *Phys. Rev. B.* **51** (1995) 734–741. doi:10.1103/PhysRevB.51.734.
- [9] M. Wissler, Graphite and Carbon Powders for Electrochemical Applications, *J. Power Sources.* **156** (2006) 142–150. doi:10.1016/j.jpowsour.2006.02.064.
- [10] S.H. Ng, C. Vix-Guterl, P. Bernardo, N. Tran, J. Ufheil, H. Buqa, J. Dentzer, R. Gadiou, M.E. Spahr, D. Goers, P. Novák, Correlations Between Surface Properties of Graphite and the First Cycle Specific Charge Loss in Lithium-Ion Batteries, *Carbon* **47** (2009) 705–712. doi:10.1016/j.carbon.2008.11.008.
- [11] H. Buqa, A. Würsig, D. Goers, L.J. Hardwick, M. Holzapfel, P. Novák, F. Krumeich, M.E. Spahr, Behaviour of Highly Crystalline Graphites in Lithium-Ion Cells with Propylene Carbonate Containing Electrolytes, *J.*

Power Sources. **146** (2005) 134–141.
doi:10.1016/j.jpowsour.2005.03.106.

- [12] M.N. Obrovac, L. Christensen, Structural Changes in Silicon Anodes During Lithium Insertion/Extraction, *Electrochem. Solid-State Lett.* **7** (2004) A93–A96. doi:10.1149/1.1652421.
- [13] L.Y. Beaulieu, T.D. Hatchard, A. Bonakdarpour, M.D. Fleischauer, J.R. Dahn, Reaction of Li with Alloy Thin Films Studied by In Situ AFM, *J. Electrochem. Soc.* **150** (2003) A1457–A1464. doi:10.1149/1.1613668.
- [14] L.Y. Beaulieu, K.W. Eberman, R.L. Turner, L.J. Krause, J.R. Dahn, Colossal Reversible Volume Changes in Lithium Alloys, *Electrochem. Solid-State Lett.* **4** (2001) A137–A140. doi:10.1149/1.1388178.
- [15] J. Li, J.R. Dahn, An In Situ X-Ray Diffraction Study of the Reaction of Li with Crystalline Si, *J. Electrochem. Soc.* **154** (2007) A156–A161. doi:10.1149/1.2409862.
- [16] M.N. Obrovac, L. Christensen, D.B. Le, J.R. Dahn, Alloy Design for Lithium-Ion Battery Anodes, *J. Electrochem. Soc.* **154** (2007) A849–A855. doi:10.1149/1.2752985.
- [17] J.O. Besenhard, J. Yang, M. Winter, Will Advanced Lithium-Alloy Anodes Have a Chance in Lithium-Ion Batteries?, *J. Power Sources*. **68** (1997) 87–90. doi:10.1016/S0378-7753(96)02547-5.
- [18] M. Holzapfel, H. Buqa, L.J. Hardwick, M. Hahn, A. Würsig, W. Scheifele, P. Novák, R. Kötz, C. Veit, F.M. Petrat, Nano Silicon for Lithium-Ion Batteries, *Electrochim. Acta.* **52** (2006) 973–978. doi:10.1016/j.electacta.2006.06.034.
- [19] M.L. Terranova, S. Orlanducci, E. Tamburri, V. Guglielmotti, M. Rossi, Si/C Hybrid Nanostructures for Li-Ion Anodes: An Overview, *J. Power Sources*. **246** (2014) 167–177. doi:10.1016/j.jpowsour.2013.07.065.
- [20] R. Petibon, V.L. Chevrier, C.P. Aiken, D.S. Hall, S.R. Hyatt, R. Shunmugasundaram, J.R. Dahn, Studies of the Capacity Fade Mechanisms of LiCoO₂/Si-Alloy:Graphite Cells, *J. Electrochem. Soc.* **163** (2016) A1146–A1156. doi:10.1149/2.0191607jes.
- [21] M. Yamada, A. Ueda, K. Matsumoto, T. Ohzuku, Silicon-Based Negative Electrode for High-Capacity Lithium-Ion Batteries: “SiO”-Carbon Composite, *J. Electrochem. Soc.* **158** (2011) A417–A421. doi:10.1149/1.3551539.

- [22] V.L. Chevrier, L. Liu, D.B. Le, J. Lund, B. Molla, K. Reimer, L.J. Krause, L.D. Jensen, E. Figgemeier, K.W. Eberman, Evaluating Si-Based Materials for Li-Ion Batteries in Commercially Relevant Negative Electrodes, *J. Electrochem. Soc.* **161** (2014) A783–A791. doi:10.1149/2.066405jes.
- [23] T. Kim, S. Park, S.M. Oh, Solid-State NMR and Electrochemical Dilatometry Study on Li⁺ Uptake/Extraction Mechanism in SiO Electrode, *J. Electrochem. Soc.* **154** (2007) A1112–A1117. doi:10.1149/1.2790282.
- [24] M.A. Al-Maghrabi, J. Suzuki, R.J. Sanderson, V.L. Chevrier, R.A. Dunlap, J.R. Dahn, Combinatorial Studies of Si_{1-x}O_x as a Potential Negative Electrode Material for Li-Ion Battery Applications, *J. Electrochem. Soc.* **160** (2013) A1587–A1593. doi:10.1149/2.115309jes.
- [25] S.J. An, J. Li, C. Daniel, D. Mohanty, S. Nagpure, D.L. Wood, The State of Understanding of the Lithium-Ion-Battery Graphite Solid Electrolyte Interphase (SEI) and its Relationship to Formation Cycling, *Carbon* **105** (2016) 52–76. doi:10.1016/j.carbon.2016.04.008.
- [26] K. Xu, Nonaqueous Liquid Electrolytes for Lithium-Based Rechargeable Batteries, *Chem. Rev.* **104** (2004) 4303–4417. doi:10.1021/cr030203g.
- [27] R. Fong, U. von Saken, J.R. Dahn, Studies of Lithium Intercalation into Carbons Using Nonaqueous Electrochemical Cells, *J. Electrochem. Soc.* **137** (1990) 2009–2013. <http://jes.ecsdl.org/content/137/7/2009.abstract>.
- [28] D. Aurbach, K. Gamolsky, B. Markovsky, Y. Gofer, M. Schmidt, U. Heider, On the Use of Vinylene Carbonate (VC) as an Additive to Electrolyte Solutions for Li-Ion Batteries, *Electrochim. Acta.* **47** (2002) 1423–1439. doi:10.1016/S0013-4686(01)00858-1.
- [29] B. Li, M. Xu, T. Li, W. Li, S. Hu, Prop-1-ene-1,3-Sultone as SEI Formation Additive in Propylene Carbonate-Based Electrolyte for Lithium Ion Batteries, *Electrochem. Commun.* **17** (2012) 92–95. doi:10.1016/j.elecom.2012.02.016.
- [30] L. Ma, J. Xia, J.R. Dahn, Improving the High Voltage Cycling of Li[Ni_{0.42}Mn_{0.42}Co_{0.16}]O₂ (NMC442)/Graphite Pouch Cells Using Electrolyte Additives, *J. Electrochem. Soc.* **161** (2014) A2250–A2254. doi:10.1149/2.1041414jes.
- [31] D.Y. Wang, J. Xia, L. Ma, K.J. Nelson, J.E. Harlow, D. Xiong, L.E. Downie, R. Petibon, J.C. Burns, A. Xiao, W.M. Lamanna, J.R. Dahn, A

- Systematic Study of Electrolyte Additives in Li[Ni_{1/3}Mn_{1/3}Co_{1/3}]O₂ (NMC)/Graphite Pouch Cells, *J. Electrochem. Soc.* **161** (2014) A1818–A1827. doi: 10.1149/2.0511412jes.
- [32] A.J. Smith, J.C. Burns, D. Xiong, J.R. Dahn, Interpreting High Precision Coulometry Results on Li-ion Cells, *J. Electrochem. Soc.* **158** (2011) A1136–A1142. doi:10.1149/1.3625232.
- [33] C.R. Birkl, M.R. Roberts, E. McTurk, P.G. Bruce, D.A. Howey, Degradation Diagnostics for Lithium Ion Cells, *J. Power Sources.* **341** (2017) 373–386. doi:10.1016/j.jpowsour.2016.12.011.
- [34] A.J. Smith, J.C. Burns, X. Zhao, D. Xiong, J.R. Dahn, A High Precision Coulometry Study of the SEI Growth in Li/Graphite Cells, *J. Electrochem. Soc.* **158** (2011) A447–A452. doi:10.1149/1.3557892.
- [35] I. Bloom, A.N. Jansen, D.P. Abraham, J. Knuth, S.A. Jones, V.S. Battaglia, G.L. Henriksen, Differential Voltage Analyses of High-Power, Lithium-Ion Cells 1. Technique and Application, *J. Power Sources.* **139** (2005) 295–303. doi:10.1016/j.jpowsour.2004.07.021.
- [36] H.M. Dahn, A.J. Smith, J.C. Burns, D.A. Stevens, J.R. Dahn, User-Friendly Differential Voltage Analysis Freeware for the Analysis of Degradation Mechanisms in Li-Ion Batteries, *J. Electrochem. Soc.* **159** (2012) A1405–A1409. doi:10.1149/2.013209jes.
- [37] R. Fathi, J.C. Burns, D.A. Stevens, H. Ye, C. Hu, G. Jain, E. Scott, C. Schmidt, J.R. Dahn, Ultra High-Precision Studies of Degradation Mechanisms in Aged LiCoO₂/Graphite Li-Ion Cells, *J. Electrochem. Soc.* **161** (2014) A1572–A1579. doi:10.1149/2.0321410jes.
- [38] L.Y. Beaulieu, V.K. Cumyn, K.W. Eberman, L.J. Krause, J.R. Dahn, A System for Performing Simultaneous In Situ Atomic Force Microscopy/Optical Microscopy Measurements on Electrode Materials for Lithium-Ion Batteries, *Rev. Sci. Instrum.* **72** (2001) 3313–3319. doi:10.1063/1.1388214.
- [39] M. Winter, G.H. Wrodnigg, J.O. Besenhard, W. Biberacher, P. Novák, Dilatometric Investigations of Graphite Electrodes in Nonaqueous Lithium Battery Electrolytes, *J. Electrochem. Soc.* **147** (2000) 2427. doi:10.1149/1.1393548.
- [40] G. Jeong, S.M. Lee, N.S. Choi, Y.-U. Kim, C.K. Lee, Stabilizing Dimensional Changes in Si-Based Composite Electrodes by Controlling the Electrode Porosity: An In Situ Electrochemical Dilatometric Study,

Electrochim. Acta. **56** (2011) 5095–5101.
doi:10.1016/j.electacta.2011.03.071.

- [41] J.L. Gomez-Cámer, C. Bünzli, M.M. Hantel, T. Poux, P. Novák, On the Correlation Between Electrode Expansion and Cycling Stability of Graphite / Si Electrodes for Li-Ion Batteries, *Carbon* **105** (2016) 42–51. doi:10.1016/j.carbon.2016.04.022.
- [42] C.P. Aiken, J. Xia, D.Y. Wang, D.A. Stevens, S. Trussler, J.R. Dahn, An Apparatus for the Study of In Situ Gas Evolution in Li-Ion Pouch Cells, *J. Electrochem. Soc.* **161** (2014) A1548–A1554. doi:10.1149/2.0151410jes.
- [43] J. Li, R. Shunmugasundaram, R. Doig, J.R. Dahn, In Situ X-ray Diffraction Study of Layered Li-Ni-Mn-Co Oxides: Effect of Particle Size and Structural Stability of Core-Shell Materials, *Chem. Mater.* **28** (2016) 162–171. doi:10.1021/acs.chemmater.5b03500.
- [44] J.N. Reimers, J.R. Dahn, Electrochemical and In Situ X-Ray Diffraction Studies of Lithium Intercalation in Li_xCoO_2 , *J. Electrochem. Soc.* **139** (1992) 2091–2097.
- [45] R. Weber, C.R. Fell, J.R. Dahn, S. Hy, Operando X-ray Diffraction study of Polycrystalline and Single-Crystal $\text{Li}_x\text{Ni}_{0.5}\text{Mn}_{0.3}\text{Co}_{0.2}\text{O}_2$, *J. Electrochem. Soc.* **Submitted** (2017).
- [46] J. Li, A.R. Cameron, H. Li, S. Glazier, D. Xiong, M. Chatzidakis, J. Allen, G.A. Botton, J.R. Dahn, Comparison of Single Crystal and Polycrystalline for High Voltage Li-Ion Cells, *J. Electrochem. Soc.* **164** (2017) A1534–A1544. doi:10.1149/2.0991707jes.
- [47] T.M. Bond, J.C. Burns, D.A. Stevens, H.M. Dahn, J.R. Dahn, Improving Precision and Accuracy in Coulombic Efficiency Measurements of Li-Ion Batteries, *J. Electrochem. Soc.* **160** (2013) A521–A527. doi:10.1149/2.014304jes.
- [48] L.J. Krause, L.D. Jensen, J.R. Dahn, Measurement of Parasitic Reactions in Li Ion Cells by Electrochemical Calorimetry, *J. Electrochem. Soc.* **159** (2012) A937–A943. doi:10.1149/2.021207jes.
- [49] J.C. Burns, A. Kassam, N.N. Sinha, L.E. Downie, L. Solnickova, B.M. Way, J.R. Dahn, Predicting and Extending the Lifetime of Li-Ion Batteries, *J. Electrochem. Soc.* **160** (2013) A1451–A1456. doi:10.1149/2.060309jes.

- [50] J. Li, H. Li, A. Cameron, S. Glazier, Q. Liu, J.R. Dahn, Impact of Electrolyte Additive Content on the Lifetime of $\text{LiNi}_{0.5}\text{Mn}_{0.3}\text{Co}_{0.2}\text{O}_2$ /Artificial and Natural Graphite Cells, *J. Electrochem. Soc.* **164** (2017) A2756–A2766. doi:10.1149/2.1731712jes.
- [51] S.L. Glazier, A.J. Louli, J. Li, J.P. Allen, J.R. Dahn, An Analysis of Artificial and Natural Graphite in Lithium Ion Pouch Cells using Ultra-High Precision Coulometry, Isothermal Microcalorimetry, Gas Evolution, Long Term Cycling and Pressure Measurements, *J. Electrochem. Soc.* **Submitted** (2017).
- [52] E. Peled, S. Menkin, Review—SEI: Past, Present and Future, *J. Electrochem. Soc.* **164** (2017) A1703–A1719. doi:10.1149/2.1441707jes.
- [53] J. Vetter, P. Novák, M.R. Wagner, C. Veit, K.C. Möller, J.O. Besenhard, M. Winter, M. Wohlfahrt-Mehrens, C. Vogler, A. Hammouche, Ageing Mechanisms in Lithium-Ion Batteries, *J. Power Sources.* **147** (2005) 269–281. doi:10.1016/j.jpowsour.2005.01.006.
- [54] M.D. Levi, G. Salitra, B. Markovsky, H. Teller, D. Aurbach, U. Heider, L. Heider, Solid-State Electrochemical Kinetics of Li-Ion Intercalation into $\text{Li}_{1-x}\text{CoO}_2$: Simultaneous Application of Electroanalytical Techniques SSCV, PITT, and EIS, *J. Electrochem. Soc.* **146** (1999) 1279–1289. doi:10.1149/1.1391759.
- [55] D. Andre, M. Meiler, K. Steiner, C. Wimmer, T. Soczka-Guth, D.U. Sauer, Characterization of High-Power Lithium-Ion Batteries by Electrochemical Impedance Spectroscopy. I. Experimental Investigation, *J. Power Sources.* **196** (2011) 5334–5341. doi:10.1016/j.jpowsour.2010.12.102.
- [56] D.W. Abarbanel, K.J. Nelson, J.R. Dahn, Exploring Impedance Growth in High Voltage NMC/Graphite Li-Ion Cells Using a Transmission Line Model, *J. Electrochem. Soc.* **163** (2016) A522–A529. doi:10.1149/2.0901603jes.
- [57] M.D. Levi, D. Aurbach, Simultaneous Measurements and Modeling of the Electrochemical Impedance and the Cyclic Voltammetric Characteristics of Graphite Electrodes Doped with Lithium, *J. Phys. Chem. B.* **101** (1997) 4630–4640. doi:10.1021/jp9701909.
- [58] R. Petibon, N.N. Sinha, J.C. Burns, C.P. Aiken, H. Ye, C.M. Vanelzen, G. Jain, S. Trussler, J.R. Dahn, Comparative Study of Electrolyte

- Additives Using Electrochemical Impedance Spectroscopy on Symmetric Cells, *J. Power Sources*. **251** (2014) 187–194. doi:10.1016/j.jpowsour.2013.11.054.
- [59] J.C. Burns, R. Petibon, K.J. Nelson, N.N. Sinha, A. Kassam, B.M. Way, J.R. Dahn, Studies of the Effect of Varying Vinylene Carbonate (VC) Content in Lithium Ion Cells on Cycling Performance and Cell Impedance, *J. Electrochem. Soc.* **160** (2013) A1668–A1674. doi:10.1149/2.031310jes.
- [60] D.S. Hall, M. Nie, L.D. Ellis, S.L. Glazier, S. Hyatt, R. Petibon, A. Xiao, W.M. Lamanna, K. Smith, I.G. Hill, J.R. Dahn, Surface-Electrolyte Interphase Formation in Lithium-Ion Cells Containing Pyridine Adduct Additives, *J. Electrochem. Soc.* **163** (2016) A773–A780. doi:10.1149/2.1091605jes.
- [61] J. Xia, J.R. Dahn, Improving Sulfolane-Based Electrolyte for High Voltage Li-Ion Cells with Electrolyte Additives, *J. Power Sources*. **324** (2016) 704–711. doi:10.1016/j.jpowsour.2016.06.008.
- [62] R. Petibon, E.C. Henry, J.C. Burns, N.N. Sinha, J.R. Dahn, Comparative Study of Vinyl Ethylene Carbonate (VEC) and Vinylene Carbonate (VC) in LiCoO₂/Graphite Pouch Cells Using High Precision Coulometry and Electrochemical Impedance Spectroscopy Measurements on Symmetric Cells, *J. Electrochem. Soc.* **161** (2013) A66–A74. doi:10.1149/2.030401jes.